

STUDIES ON CORROSION, MECHANICAL AND WETTING PROPERTIES OF THE THERMAL SPRAYED COATINGS ON LOW CARBON STEEL

Thesis

Submitted in partial fulfillment of the requirements for the degree of
DOCTOR OF PHILOSOPHY

By

AMUDHA A

(Reg.No. 155021PH15F02)



**DEPARTMENT OF PHYSICS
NATIONAL INSTITUTE OF TECHNOLOGY KARNATAKA
SURATHKAL, MANGALORE - 575025**

STUDIES ON CORROSION, MECHANICAL AND WETTING PROPERTIES OF THE THERMAL SPRAYED COATINGS ON LOW CARBON STEEL

Thesis

Submitted in partial fulfillment of the requirements for the degree of

DOCTOR OF PHILOSOPHY

By

AMUDHA A

(Reg.No. 155021PH15F02)

Under the guidance of

Prof. H.D SHASHIKALA AND Dr. H.S NAGARAJA



**DEPARTMENT OF PHYSICS
NATIONAL INSTITUTE OF TECHNOLOGY KARNATAKA
SURATHKAL, MANGALORE - 575025**

AUGUST, 2020

DECLARATION

By the Ph.D. Scholar

I hereby declare that the Research Thesis entitled “**Studies on corrosion, mechanical and wetting properties of the thermal sprayed coatings on low carbon steel**” which is being submitted to the **National Institute of Technology Karnataka, Surathkal** in partial fulfillment of the requirements for the award of the Degree of **Doctor of Philosophy in Physics** is a bonafide report of the research work carried out by me. The material contained in this Research Thesis has not been submitted to any University or Institution for the award of any degree.



Amudha A

(Register No.: 155021PH15F02)


Department of Physics

Place: NITK, Surathkal

Date:

CERTIFICATE

This is to certify that the Research Thesis entitled “**Studies on corrosion, mechanical and wetting properties of the thermal sprayed coatings on low carbon steel**” submitted by **Amudha A (Register Number: 1155021PH15F02)** as the record of the research work carried out by her, is accepted as the *Research Thesis* submission in partial fulfillment of the requirements for the award of the degree of *Doctor of Philosophy*.

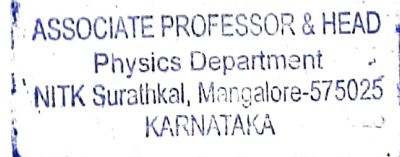

Prof.(Mrs). H.D Shashikala


Dr. H.S Nagaraja

Research Supervisors,
Department of Physics,
N.I.T.K. Surathkal – 575025


18/10/2021
Chairman – DRPC

(Signature with Date and Seal)



ACKNOWLEDGEMENT

I record my sincere gratitude to my Research Guides, Prof.(Mrs) H.D. Shashikala, and Dr. H.S Nagaraja for their guidance, motivation, and support throughout my research work. I am grateful to NITK Surathkal and its Physics department for awarding the full-time Institute Research Scholarship and contingency grant from the Ministry of Human Resource and Development (MHRD), India. I thank the Chairman and the members of the Research Progress Assessment Committee (Dr. Kartick Tarafder, Department of Physics, and Dr. K.S Ravi Shankar, Department of MME) for their suggestions. I extend my thanks to the entire teaching faculty and non-teaching staff, and research scholars of the Physics department, NITK, for their co-operation.

I sincerely thank Dr. Anup Kumar Keshri and his student O.S Asiq Rahman, IIT Patna, for the plasma sprayed coatings used in this work. I thank Mr.Joshi, M/s Spraymet-Bangalore for the thermal sprayed coating facility. I express thanks to Dr. Harish Barshilia- NAL, Bangalore for the XPS facility. I am grateful to Prof. Arvind Agarwal, Florida International University-Miami, USA, for his motivation and encouragement for taking up thermal sprayed coatings as a research interest. I express my gratitude to Mr. V.T Bhanukiran, Deputy Managing Director, Doosan Pvt. Ltd-Haryana for teaching and sharing his expertise in ANSYS simulation. I sincerely thank Mr.Joel for the weld overlay facility. I also thank the editors and reviewers of my publications for their valuable assessment.

My thanks go to many of the present and former research scholars of Materials Processing Laboratory and Materials Research Laboratory for their co-operation. I acknowledge many research scholars especially Miss. Bindu K, Mr. Mahendra K, Mr. Brijesh K, Mr. Achyutha K, Mr. Bharath, and Miss. Sulakshana Shenoy, for their help in completing this work. I remain grateful for all the help, moral support, and motivation received from my friends Mrs. Koushalya M, Mrs. Harshita, Mrs. Geetha M.D, Mrs, Suji K, Mr. Shiva Kumar, Fr. Jesuraj, Mr. Irfan, Mrs. Swapna Mansani, Mrs. Ashwathi pillai, Mrs. Bhanumathi, Mrs. Lalitha Tripura Sundari, Mrs. Arti Sahaya Rones, Mrs. Madhavi O, Miss. Uma Sakthivel, Miss. Advitha M, Mrs. Showri Ranjana, Mr. Nanda Kishore, and many people. I express sincere gratitude to Mr.Adi Golugure and Mrs.Kavitha Golugure as well as Mr. Hari

Chintapalli and Mrs. Radhika Chintapalli's families for their kind help during my visit to Boston (USA) for a conference, without them, the journey would have been quite difficult.

I am thankful to Prof. Alope Paul and Dr. Ravi Raju, Department of Materials Engineering, IISc-Bangalore, and Prof. Sastri Ramchandru, PESIT, who particularly sparked my interest in research. I express my heartfelt thanks to Mr. Anil Kumar Yekkala, a father figure who is my source of inspiration, for his continuous care and support. I am always grateful to all the volunteers of Friends of Children Trust-Bangalore especially Mr. Murtuza Khetty, Mr. Vivek Pradhan, Mr. Ravi Vattipalli, Mr. Akash Narayana, Mr. Rohit Shetti, Mr. Shrikanth Hampiholi, Mr. Harish M Pillai, Mr. Nagarjuna, Mr. Shrikanth, Mrs. Divya Prabhu and Mr. Sanjay Padubidri for motivating me to do PhD and guiding me until now. I also thank my school and college teachers from Vidya Mandir School, Jyothi School, St.Teresa's girl's high school, Navajeevana-Salesian Sisters, Vijaya College-Basavanagudi, National College-Jayanagar, and NITK-Surathkal.

I remain grateful for all the help, moral support, technical aid, and motivation I received from many people, directly or indirectly in several aspects, at different stages throughout my Ph. D. tenure. Finally, I acknowledge the love, support, and encouragement from my family in this endeavor. Last but not the least, I express my honest thanks to Mr. Chowdareddy Narayanareddy a friend for life, mentor, care taker and a support system who constantly cares, motivates and encourages me to fulfill my dreams.

ABSTRACT

Low-carbon or mild carbon steels are very attractive materials throughout the industrialized world in diverse applications but are susceptible to corrosion. This problem can be mitigated and the service lifetime of the low carbon steel can be increased by the application of protective coatings with good mechanical properties while reducing maintenance costs. In the present work, different corrosion-resistant materials like metal alloy (Inconel-625), ceramic-metal composite 25(NiCr)-75Cr₃C₂ and ceramic-graphene oxide nanoplatelets(GNP) composite (Al₂O₃-GNP and ZrO₂-GNP) were coated using thermal spray techniques like weld overlay, High-Velocity Oxyfuel (HVOF), and Atmospheric Plasma Spray (APS) techniques respectively. The structural, morphological and compositional studies were carried out by XRD, FTIR, Raman Spectroscopy, XPS, FESEM-EDAX, TEM, and BET characterization techniques. The corrosion studies were conducted using the three-electrode electrochemical system. The stability of the coatings was studied using immersion tests upto 14 days. The mechanical and wetting properties of samples were studied using Vicker's microhardness tester and contact angle measurements respectively.

ANSYS FEA simulation showed that alternate skip weld overlay of SS-309Mo as the buffer layer by GTAW and Inconel-625 as final layer by SMAW process for the 6 mm thick low carbon steel substrate preheated to 100°C, to be the best model with 18 MPa surface residual stress among twelve combinations. Using the conditions of the best model, SS-309Mo and Inconel-625 have been coated on low carbon steel. The weld overlay coated Inconel-625 had nearly the same corrosion resistance as that of bulk Inconel-625 with increased microhardness.

25(NiCr)-75Cr₃C₂ cermet coating on low carbon steel using HVOF process showed hydrophobic behaviour with improved microhardness and corrosion resistance. The α -Al₂O₃-(X wt. %GNP) and ZrO₂-(X wt. %GNP) (where X= 0, 0.5, 1.0, 1.5 and 2) composite coatings by APS process were successful in the retention of GNPs in the composite. The surface corrosion resistance increased by six orders of magnitude when coated with 2.0 wt.% GNP reinforced α -Al₂O₃ nanocomposite, in comparison with bare Al₂O₃ coating. The increase in corrosion resistance is due to the hydrophobic nature of in-situ reduced GNP. In addition, the mechanical properties have improved with the addition of GNP. The corrosion rate of ZrO₂-2 wt. % GNP coating is 130 times lesser than that of ZrO₂. Further, the mechanical and wetting properties of the coatings showed a similar trend as that of corrosion behaviour.

Keywords: low carbon steel; thermal spray coating; corrosion; mechanical; wetting properties

*Dedicated to my beloved mother Mrs. Lakshmi,
father Mr. Armugam
and friend for life Mr. N. C. Reddy.*

TABLE OF CONTENTS

S.No		Page No
1	CHAPTER 1 Introduction	1
1.1	Carbon steel	1
1.2	Background to corrosion	2
1.2.1	Types of corrosion	3
1.2.2	Electrochemical corrosion	6
1.2.3	Corrosion resistant materials	8
1.2.4	Corrosion resistant coating techniques	10
1.3	Literature review	23
1.4	Scope and objectives of the work	29
	Scope of the work	29
	Objective of the present work	29
2	CHAPTER 2 Experimental details	31
2.1	Materials	31
2.1.1	Substrate and Coating Materials	31
2.2	Synthesis of composites for coating	32
2.2.1	Synthesis of Graphene Oxide by Hummers method	32
2.2.2	Synthesis of Composite powder by Spray Drying process	33
2.3	Coating methods	35
2.3.1	Weld overlay coating	35
2.3.2	Coating of $75\text{Cr}_3\text{C}_2$ -25(NiCr) cermet by HVOF process	40
2.3.3	Coating of Alumina-xGO and Zirconia-xGO (x- 0.0, 0.5, 1.0, 1.5 and 2.0 wt.%) composites by APS process	41
2.4	Characterization of the samples	42

2.5	Study of corrosion, mechanical and wetting properties of the samples	43
2.5.1	Electrochemical corrosion properties of the coatings	43
2.5.2	Mechanical properties of the coatings	45
2.5.3	Wetting properties of the coatings	46
3	CHAPTER 3 Weld overlay of Inconel-625 on the substrate with ss-309mo as buffer layer: corrosion, mechanical and wetting properties	49
3.1	Introduction	49
3.2	Brief Methodology	51
3.3	Results and Discussion	51
3.3.1	ANSYS FEA analysis for selection of the best model for WO coating based on low residual stress.	51
3.3.2	Weld Overlay Coating of Model 12B	60
3.3.3	Electrochemical corrosion behaviour of the coatings	62
3.3.4	Mechanical properties of the coatings	68
3.4	Summary and conclusion	69
4	CHAPTER 4 HVOF coating of nickel chromium-chromium carbide cermet: corrosion, mechanical and wetting properties	71
4.1	Introduction	71
4.2	Brief Methodology	72
4.3	Results and Discussion	72
4.3.1	Structural Analysis of the coating	72
4.3.2	Morphological Analysis of the coatings	73
4.3.3	Electrochemical corrosion behaviour of the coatings	73
4.3.4	Mechanical properties of the coatings	78
4.3.5	Wetting properties of the coatings	79
4.4	Summary and Conclusion	80
5	CHAPTER 5 Plasma sprayed α -Al ₂ O ₃ -GO composite: Corrosion, mechanical and wetting properties	83

5.1	Introduction	83
5.2	Brief Methodology	84
5.3	Results and Discussion	85
5.3.1	Dispersion of GO nanoplatelets in the spray-dried alumina powder	85
5.3.2	Structural and morphological analysis of the coatings	87
5.3.3	Electrochemical Corrosion properties of the coatings	96
5.3.4	Mechanical properties of the coatings	100
5.3.5	Wetting properties of the coatings	102
5.3.6	Porosity of the coatings	103
5.4	Summary and conclusion	104
6	CHAPTER 6 Plasma sprayed ZrO ₂ -GNP composite coating: Corrosion, mechanical and wetting properties	107
6.1	Introduction	107
6.2	Brief Methodology	108
6.3	Results and discussion	108
6.3.1	Dispersion of GO nanoplatelets(GNP) in the spray-dried Zirconia powder	108
6.3.2	Structural and morphological analysis of the coatings	111
6.3.3	Electrochemical corrosion properties of the coatings	116
6.3.4	Mechanical properties of the coatings	121
6.3.5	Wetting properties of the coatings	122
6.4	Summary and conclusion	124
7	CHAPTER 7 Summary and conclusion of the thesis	127
8	Appendix I-III	
I	References	
II	List of Publications, conferences and workshops attended	
III	Brief Curriculum Vitae	

LIST OF FIGURES

Figure No.	Description	Page No.
Fig. 1.1	Corrosion of Pump Impeller in Sea Water	2
Fig. 1.2	Uniform Corrosion	4
Fig. 1.3	Schematic of Pitting Corrosion	4
Fig. 1.4	Corrosion Fatigue Cracks	6
Fig. 1.5	Schematic electrochemical corrosion mechanism of iron	7
Fig. 1.6	Schematic representation of graphene oxide structure	9
Fig. 1.7	Schematic representation of thermal spray process	12
Fig. 1.8	Schematic representation of types of thermal spray process	13
Fig. 1.9	Weld overlay of the filler material on the substrate	14
Fig. 1.20	Schematic representation of a) GTAW and b) SMAW processes	15
Fig. 1.21	Schematic representation of standard HVOF process system	16
Fig. 1.22	Schematic Representation of Atmospheric Plasma spray process	18
Fig. 1.23	Schematic representation of different wetting models [(a), (b) and (c)] and wetting behaviour [(d), (e), (f) and (g)].	21
Fig. 1.24	Schematic representation of the Vicker's Indenter	23
Fig. 2.1	Schematic representation of stepwise synthesis graphene oxide by Hummer's method	33
Fig. 2.2	Schematic representation of spray drying process	34
Fig. 2.3	(a) ANSYS Model of skip welding of first and second layer (weld coatings on substrate with dimensions) and (b) moving heat source due to welding	38
Fig. 2.4	Schematic representation of weld overlay deposition of SS-309Mo and Inconel-625 on the substrate (CS).	39
Fig. 2.5	Schematic representation of three electrode electrochemical set up.	44
Fig. 2.6	Photograph of Clemex microhardness tester	46
Fig. 2.7	Photograph of the Holmarc's Contact angle meter	47
Fig. 3.1	Single layer residual stress comparison with process and coating variation	55
Fig. 3.2	Multilayer residual stress comparison with a single process and a single material.	56

Fig. 3.3	Multilayer residual stress comparison with process and coating material variation	57
Fig. 3.4	Multilayer residual stress comparisons with BM preheat and without preheat variation and BM thickness variation.	58
Fig. 3.5	Residual Stress for multilayer coating with variation in BM thickness	58
Fig. 3.6	XRD plot of the substrate (CS), SSCS and ISSCS.	60
Fig. 3.7	SEM image of (a) CS, SSCS and ISSCS at the cross-section, (b)top surface of SSCS (c) and (d) the top surface of ISSCS at lower and higher magnifications respectively.	61
Fig. 3.8	(a) Tafel plot of CS, SSCS and ISSCS, bare SS-309Mo and Bare Inconel-625, (b) Nyquist Impedance Plot (with insets of enlarged Nyquist plot CS and equivalent circuit used for fitting), c) Bode plot and d) Bode impedance plot of CS, SSCS and ISSCS.	62
Fig. 3.9	(a) and (b) Tafel plots and (c) and (d) Nyquist plot of the SSCS and ISSCS respectively at different immersion periods namely 1hour, 1day, 7days and 14 days.	67
Fig. 3.10	Vicker's indentation on a) substrate (CS), b) SSCS and c) ISSCS	68
Fig. 4.1	XRD plot of (a) substrate (b) 25(NiCr)-75Cr ₃ C ₂ coating on the substrate	72
Fig. 4.2	SEM image of the 25(NiCr)-75Cr ₃ C ₂ coated samples	74
Fig. 4.3	Tafel plots of the 25(NiCr)-75Cr ₃ C ₂ coating and the substrate.	75
Fig. 4.4	(a) Nyquist Impedance plot of the substrate and the coating (b) Equivalent circuit of the substrate and (c) Equivalent circuit of the coating	76
Fig. 4.5	(a) Impedance spectra (b) Bode plot for both 25(NiCr)-75Cr ₃ C ₂ coating and the substrate.	77
Fig. 4.6	Vicker's micro-indentation on a) Substrate low carbon steel IS2062 grade and b) thermal sprayed 25(NiCr)-75Cr ₃ C ₂ coating	78
Fig. 4.7	Contact angle image of 3.5wt.%NaCl solution on a) substrate and b) the HVOF thermal sprayed 25(NiCr)-75Cr ₃ C ₂ coating captured using the sessile drop method.	79
Fig. 5.1	FESEM images of powder distribution of a) GO nanoplatelets, b) spray dried alumina (SDA) and c) Spray-dried alumina with 0.5 wt. % GO Nanoplatelets (SDA-0.5GO).	85

Fig. 5.2	(a) XRD pattern and (b) Raman spectra of GO Nanoplatelets, SDA and SDA-0.5GO Nanocomposite powders.	86
Fig. 5.3	XRD of SDA, SDA-0.5GO, SDA- 1.0GO, SDA- 1.5GO, and SDA- 2.0GO plasma-sprayed composites	87
Fig. 5.4	Raman spectroscopy of SDA, SDA-0.5GO, SDA- 1.0GO, SDA- 1.5GO, and SDA- 2.0GO plasma-sprayed composites	88
Fig. 5.5	FTIR spectra of as-synthesized SDA and SDA-(0.5, 1.0, 1.5 and 2.0) wt.% GO coatings.	89
Fig. 5.6	XPS survey spectra of (a) SDAGO powder and (b) SDAGO plasma sprayed coatings	90
Fig. 5.7	XPS spectra of a) carbon (C1s), b) aluminum (Al2p), c) oxygen (O1s) of SDA coatings and d) C1s, e) Al2p and f) O1s are of SDA-0.5GO composite coatings.	91
Fig. 5.8	FESEM surface morphology of a) SDA, b) SDA-0.5GO, e) SDA-1GO, f) SDA-1.5GO g) SDA-2GO coatings, and c) and d) EDS mapping on alumina splat region and also on GO flakes region respectively	92
Fig. 5.9	SEM showing surface morphology at the cross-section of a) SDA, b) SDA coating at higher magnification, c) SDAGO Coating and d) SDAGO showing GO nanoplatelets at 2.0 wt.% GO in the coatings	93
Fig. 5.10	The FESEM images showing thickness of the plasma sprayed coatings of SDA-0.5%GO, SDA-1.0%GO, SDA-1.5%GO and SDA-2.0%GO composites.	94
Fig. 5.11	HR-TEM images of a) GO nanoplatelets b) SDA c) SDA- 0.5GO d) SDA- 1.0GO e) SDA- 1.5GO and f) SDA- 2.0GO with d spacing of Al ₂ O ₃ and their corresponding SAED patterns	95
Fig. 5.12	a) Tafel plot b) Nyquist plot (inset shows Nyquist plot of SDA and equivalent circuit) c) Bode plot and d) Bode impedance plot	96
Fig. 5.13	Variation of Current density and corrosion rate as a function of composition	97
Fig. 5.14	(a), (b), (c), (d) and (e) SEM morphology of SDA and SDA(0.5, 1.0, 1.5 and 2.0)GO composites before corrosion and, (f), (g), (h), (i) and (j) after corrosion test respectively.	98

Fig. 5.15	a) Variation of microhardness and b) variation of fracture toughness of the plasma sprayed coatings SDAGO composites as a function of GO wt.% addition	101
Fig. 5.16	Contact angle measurement variation as a function of wt.% GO nanoplatelets addition to Alumina	102
Fig. 5.17	pore diameter (pore size) as a function of GO wt.% in SDA-GO composite	104
Fig. 6.1	(a) and (b) Surface morphology of the SDZ, (c) and (d) SDZ-1wt.%GNP powder at lower and higher magnification respectively	109
Fig. 6.2	TEM micrographs of (a) GNPs, (b) SDZ, (c) SDZ-1wt.%GNP and (d) SDZ-2wt.%GNP powders	110
Fig. 6.3	XRD spectrum of (a) SDZ and SDZ-(0.5, 1.0, 1.5 and 2.0 wt.%)GNP powder	111
Fig. 6.4	XRD spectrum of (a) PSZ and PSZ-(0.5, 1.0, 1.5 and 2.0 wt.%)GNP, (b) Highlighted peak at 12° to show retention of GO in the plasma-sprayed coatings	112
Fig. 6.5	Monoclinic and tetragonal structure ZrO ₂ .	113
Fig. 6.6	Raman spectra of PSZ and PSZ-(0.5, 1.0, 1.5 and 2.0)wt.%GNP plasma sprayed coatings	114
Fig. 6.7	FE-SEM images of (a) PSZ, (b) Higher magnification of PSZ, and (c) EDAX spectra of PSZ, (d) PSZ-1.0GNP, (e) Higher magnification of PSZ-1.0GNP (f) EDAX spectra of PSZ-1.0GNP, (g) PSZ-2.0GNP, (h) Higher magnification of PSZ-2.0GNP and (i) EDAX spectra of PSZ-2.0GNP	115
Fig. 6.8	FESEM cross sectional image of (a) PSZ and (b) PSZ-GNP coatings	115
Fig. 6.9	(a) Tafel plot of SDZ and SDZ-(0.5, 1.0, 1.5, and 2.0)wt.%GNP plasma sprayed coatings, (b) Variation of corrosion rate, and (c) Variation of corrosion current density with the composition.	116
Fig. 6.10	EIS plot of PSZ and PSZ-(0.5, 1.0, 1.5 and 2.0)wt.%GNP plasma sprayed coatings. (a) The Nyquist plot, (b) equivalent circuit (c) Bode Plot, and (d) Impedance plot	118
Fig. 6.11	The Nyquist plot of (a)PSZ, (b)PSZ-0.5GNP, (c) PSZ-1.0GNP (d) PSZ-1.5GNP (e) PSZ-2.0GNP immersed for various durations and (f) PSZ-	120

(0.5, 1.0, 1.5 and 2.0)wt.%GNP plasma sprayed coatings immersed for 14 days

Fig. 6.12 Variation of microhardness of the PSZ and PSZ-(0.5, 1.0, 1.5, and 2.0) wt.% GNP plasma sprayed coatings. 121

Fig. 6.13 Contact angle measurement of (a)PSZ, (b)PSZ-0.5GNP, (c) PSZ-1.0GNP (d) PSZ-1.5GNP (e) PSZ-2.0GNP 123

LIST OF TABLES

Table No	Description	Page No.
Table 1.1	The main parameters of APS process	19
Table 2.1	Composition of the substrate and the coating material	31
Table 2.2	IS-2062 Grade-B Temperature Dependent Properties	36
Table 2.3	SS-309Mo Temperature Dependent Properties	36
Table 2.4	Inconel-625 Temperature Dependent Properties	37
Table 2.5	Welding Parameters for Weld Deposition	40
Table 2.6	The HVOF process parameters used for coating of 75Cr ₃ C ₂ -25(NiCr)	41
Table 2.7	Atmospheric Plasma Spray process parameters employed for Alumina-xGO composite coatings.	41
Table 2.8	Process parameters used for plasma spray deposition of Zirconia-xGO composites coatings.	42
Table 3.1	Twelve different combinations of Coating Materials and Welding Process	53
Table 3.2	Corrosion parameters obtained for substrate and weld coated samples from LPR test	63
Table 3.3	Equivalent circuit fitting parameters	65
Table 3.4	Hardness values for coated and uncoated samples in GPa	68
Table 4.1	Corrosion parameters comprising of Coating and the substrate	75
Table 4.2	Values of elements of Equivalent Circuit	76
Table 4.3	The mechanical properties of the substrate and the 25(NiCr)-75Cr ₃ C ₂ coating.	78
Table 5.1	Characteristic IR functional groups of GO, SDA, and SDAGO	90
Table 5.2	Electrochemical parameters obtained by Tafel extrapolation	97
Table 5.3	Equivalent circuit fitting elements	99
Table 5.4	Mechanical properties of SDA and SDAGO composite coatings	101

Table 6.1	Table 6.1 Electrochemical parameters obtained from Tafel extrapolation of LPR tests.	117
Table 6.2	Electrochemical circuit parameters obtained from EIS fitting	118
Table 6.3	Electrochemical circuit parameters obtained from EIS fitting after 14 days	119
Table 6.4	Mechanical properties of PSZ and PSZ-(0.5, 1.0, 1.5, and 2.0) wt.%GNP plasma sprayed coatings.	122
Table 7.1	Table of summary	131

NOMENCLATURE

PREN	Pitting Resistance Equivalent Number
SCC	Stress Corrosion Cracking
HVOF	High Velocity Oxy Fuel
APS	Atmospheric Plasma Spray
GTAW	Gas Tungsten Arc Welding Overlay
SMAW	Shielded Metal Arc Welding Overlay
GO	Graphene Oxide
GNP	Graphene oxide Nanoplatelets
Gr	Graphene
Cr_3C_2	Chromium carbide
Al_2O_3	Alumina
ZrO_2	Zirconia
Cr	Chromium
Mo	Molybdenum
N	Nitrogen
M	Metal
Ni	Nickel
Na	Sodium
Nb	Niobium
Cl	Chlorine
Fe	Iron
O	Oxygen

H	Hydrogen
Cu	Copper
e^-	Electron
<i>CR</i>	Corrosion Rate
<i>R</i>	Resistance
<i>C</i>	Capacitance
<i>C_{dl}</i>	Double layer capacitance
<i>CPE</i>	Constant Phase Element
<i>R_{ct}</i>	Charge transfer resistance
<i>Z</i>	Impedance
mmpy	Mille meter per year
θ_γ / CA	Contact Angle
γ	Interfacial Tension
<i>s</i>	Solid
<i>l</i>	liquid
<i>v</i>	vapor
<i>GPa</i>	Giga Pascal
<i>MPa</i>	Mega Pascal
<i>Hv</i>	Vicker's Hardness

CHAPTER 1

Introduction

CHAPTER 1

Introduction

Overview

In this chapter, an introduction to carbon steel, corrosion, different types of corrosion, its causes and its effects on various industries are mentioned. Coating materials and methods to overcome the corrosion problems, improvement of wetting and mechanical properties of the coatings to mitigate the corrosion are discussed. Brief literature on the research topic, scope, and objective of the thesis have been discussed. Also, at the end of this chapter, a brief outline of the thesis has been included.

1.1 Carbon steel

Carbon steels are used throughout the technologically advanced world in varied applications such as construction, chemical and metal processing equipment, nuclear/fossil fuel power plants, transportation, oil and gas industries, mining, marine and shipping industry. It offers the advantages of easy availability, lower price, and ease of fabrication. On exposure to water, iron corrosion products would be formed on the steel and may create operational problems of equipment and plants.

Carbon steels normally have about 1% carbon and its alloys contain less than 2% carbon by weight. Low-carbon or mild carbon steels contain less than 0.25% carbon and are used due to their welding and forming abilities, which make them very attractive for construction applications (Dwivedi et al 2017). These carbon steels are susceptible to corrosion. Carbon steels perform very well in dry atmospheres but the rate of corrosion increases dramatically in high humidity or saline-industrial environments leading to corrosion failure of the material (Liu et al 2016). Other factors that can affect the corrosion rate of carbon steels are continuous immersion in an aqueous environment which will increase the corrosion rate. However, immersion in stagnant water will retard the corrosion rate of carbon steels. Pitting and non-uniform corrosion attacks are associated with carbon steels in high-humidity and/or saline-industrial environments (Hayden et al 2019). This problem can be mitigated and the service lifetime of the low

carbon steel can be increased with the application of protective coatings with good mechanical properties while reducing maintenance costs.

1.2 Background to corrosion

Corrosion is nothing but the degradation or destruction of a material due to electrochemical or chemical reactions, with its surrounding medium (Popoola et al 2013). Corrosion occurs mostly in metals (although corrosion can occur in non-metallic components), as all pure metals try to return to its lowest energy state, which they had as sulfides and oxides.



Fig. 1.1 Corrosion of Pump Impeller in Sea Water (www.tomson.com)

Corrosion is one of the major problems faced by the industry, especially when pumps, ship impellers, and other equipment have to work in harsh environments like seawater. For example: When pump components like impellers are made of low-grade material without adequate corrosion resistance, severe corrosion damage occurs when operating in a seawater environment.

The loss to the industry due to corrosion-related problems can be divided into two categories:

1. Direct Loss: Maintenance cost, use of costly material, the extra thickness of components.
2. Indirect loss: Monetary loss due to equipment under repair, accidents due to leakage, environment contamination due to corrosion products.

1.2.1 Types of corrosion: The main types of corrosion occurring in components working in a seawater environment are:

1. Uniform Corrosion and Pitting Corrosion (which are not residual stress-related).
2. Stress Corrosion Cracking and Corrosion Fatigue (which are residual stress-related).

Residual stresses are stresses which remain in the material or coating after all operations like welding overlay, thermal spray, etc. are completed and all external loads like restraint are removed. Residual stresses develop due to many reasons. For example, they can be due to

- non-uniform thermal expansion and shrinkage during welding overlay, thermal spray, thermal cutting.
- sudden quenching of material from an elevated temperature.
- forces experienced by the material during heavy operations like grinding, metal cutting, etc.
- phase transformation of material from the austenitic phase to the martensitic phase due to volume changes in structure.

Residual stresses are classified according to which produce them such as mismatch stresses, thermal stresses, and stresses due to plastic deformation.

1.2.1.1 Uniform Corrosion

Uniform corrosion, as shown in **Fig. 1.2** is a uniform attack of metal resulting in oxide layer formation. This occurs by a chemical reaction of metal with oxygen in the air. The metals in dry atmosphere at room temperature are shielded by a very thin layer of oxide. At very high temperatures, the reaction with oxygen in the air can continue without resistance and will be quickly converted into an oxide.

At room temperature, the oxidation reaction stops when the oxide layer is thin. The oxide layer formed protects the metal from further oxidation. For example, the iron oxide layer formed on low carbon steel is less durable in seawater, than the chromium oxide layer formed on stainless steel. This results in a higher corrosion rate in low carbon steel than in stainless steel.



Fig. 1.2 Uniform Corrosion (www.tomson.com)

1.2.1.2 Pitting Corrosion

Pitting corrosion, as shown in **Fig. 1.3** is a form of local corrosion; in which major part of the metal surface is unaffected and only tiny part of the surfaces are highly affected forming holes. It is a form of electrochemical corrosion, in which anode and cathodic sites are formed due to the local breakage of an oxide film. Pitting corrosion is more unsafe than the uniform corrosion because it is very difficult to predict and detect it (Frankel & Sridhar 2008).

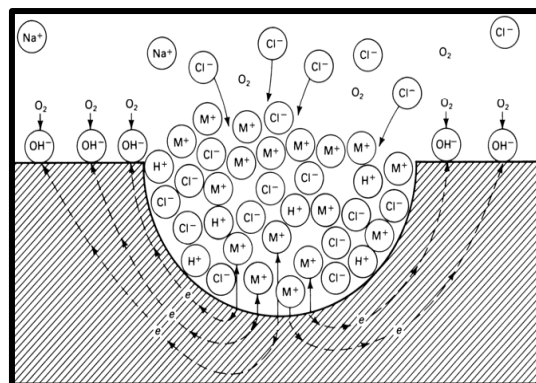


Fig. 1.3 Schematic of Pitting Corrosion (Frankel & Sridhar 2008)

The stages of pitting corrosion are pit initiation and pit growth. An initial corrosion may form a pit on the surface by a passive oxide film. The anodic reaction starts at the initial pit which is exposed to corrosive medium like seawater. The surrounding metal surface acts as the cathode. As the anodic region is very small compared to the large cathodic region, the corrosion rate is very high at the anode and a deep pit formation results in holes in the components.

It is widely known that by increasing the amount of chromium, adding alloying elements like molybdenum and nitrogen in stainless steel increases the resistance to pitting corrosion. The pitting resistance equivalent number (PREN) is used to rank and compare the resistance of different ferrous and non-ferrous steels according to their pitting resistance. The effect of alloying elements on pitting resistance in alloys plays a major role. The most commonly used PREN formula for stainless steel and nickel alloys is as shown in Equation 1 (Corres et al 1999).

$$\text{PREN} = \% \text{Cr} + 3.3 \times \% \text{Mo} + 16 \times \% \text{N}$$

[1.1]

The pitting resistance or PREN number increases with the increase in alloying content, but the cost also increases substantially with an increase in alloying content. For example, Inconel-625 with a PREN number of around 51 is 40 times costlier than Stainless Steel Grade SS-316 which has a PREN of around 25.

1.2.1.3 Stress Corrosion Cracking

Stress Corrosion Cracking (SCC) is due to combined effect of corrosive environments like seawater and the presence of tensile stress in the component. The tensile stress may be from directly applied stress on the material or from residual stress in the material. Cold forming, grinding, heat treatment, machining, and welding can induce tensile residual stresses. The magnitude of residual stresses can be close to the yield strength of the metal (Toribio 1998).

1.2.1.4 Corrosion Fatigue

Corrosion fatigue, as shown in **Fig. 1.4** is the degradation of a material under the combined act of a corrosive environment and cycling stresses. The fatigue stresses cause break of the protective passive film leading to acceleration of corrosion process. The corrosion fatigue fracture is brittle in nature and the cracks are mostly trans-granular, as in SCC, but not branched. The presence of tensile residual stress increases the ability of cyclic stresses to cause corrosion fatigue failure (Selines & Pelloux 1972).



Fig. 1.4 Corrosion Fatigue Cracks (www.hghouston.com)

1.2.2 Electrochemical Corrosion

Corrosion of materials may be due to either by chemical processes or by electrochemical process (Bhandari et al 2015). Of these, the most important is electrochemical corrosion of metals (M), in which the oxidation process $M \rightarrow M^+ + e^-$ is aided by the presence of a suitable electron acceptor, sometimes referred to in corrosion science as a *depolarizer*. In a sense, corrosion can be regarded as the spontaneous return of metals to their ores.

The corrosion process is of oxidation and reduction steps occur at separate locations on the metal. Since, the metals are conductive, the electrons can flow through the metal from the anodic to the cathodic sites (**Fig.1.5**). As in **Fig.1.5**, the presence of water is necessary in order to transport ions to and from the metal, even a thin film of adsorbed moisture can be sufficient. Corrosion often initiates at a location, (1) The metal is under stress (at a bend or weld) or is isolated from the air (where two pieces of metal are joined or under a loosely-adhering paint film). The metal ions dissolve in the moisture film and the electrons migrate to another location. (2) They are taken up by a depolarizer. Oxygen is the most common depolarizer; the resulting hydroxide ions react with the Fe^{2+} to form the mixture of hydrous iron oxides known as rust.

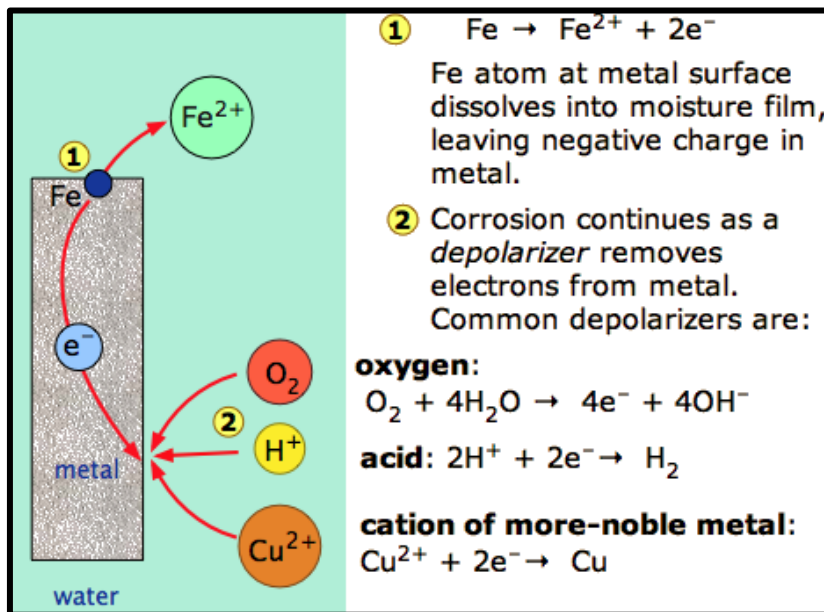


Fig.1.5 Schematic electrochemical corrosion mechanism of iron.
Source-(<https://chem.libretexts.org/>).

A corrosion system can be regarded as a short-circuited electrochemical cell in which the anodic process is something like



and the cathodic steps may involve the reduction of oxygen gas



or the reduction of protons



or the reduction of a metal ion



Where M is the metal.

If one part of a metallic object is protected from the atmosphere so that there is insufficient O_2 to build or maintain the oxide film, this "protected" region will often be the site at which corrosion is most active. The fact that such sites are usually hidden from view accounts for much of the difficulty in detecting and controlling corrosion. In contrast to anodic sites, which tend to be localized to specific regions of the surface, the cathodic part of the process can occur almost anywhere. Because metallic oxides are

usually semiconductors, most oxide coatings do not inhibit the flow of electrons to the surface, so almost any region that is exposed to O₂ or to some other electron acceptor can act as a cathode. The tendency of oxygen-deprived locations to become anodic is the cause of many commonly-observed patterns of corrosion. A very common cause of corrosion is having two dissimilar metals in contact, as might occur near a fastener or at a weld joint. Moisture collects at the junction point, acting as an electrolyte and forming a cell in which the two metals serve as electrodes. Moisture and conductive salts on the outside surfaces provide an external conductive path, effectively short-circuiting the cell and producing very rapid corrosion.

1.2.3 Corrosion Resistant Materials

Corrosion-resistant coatings for metal vary depending on the kind of metal involved and the kind of corrosion prevention needed. The materials which form durable oxide layers in seawater are preferred for components working in seawater environments. Some of the examples of materials that form a durable oxide layer are Stainless Steel Grade SS-316, SS-309Mo, Duplex Stainless Steel, Inconel-625, and Hastelloy-276. All these steels form a stable oxide film that fights Uniform Corrosion. But a different corrosion phenomenon called pitting corrosion decides which material is better for seawater operation (Kim et al 2015).

To prevent galvanic corrosion in iron and steel, coatings made from zinc and aluminum are helpful. Large components, such as bridges and energy windmills, are often treated with zinc and aluminum corrosion-resistant coatings because they provide reliable long-term corrosion prevention (Li 2001). Steel and iron fasteners, threaded fasteners, and bolts are often coated with a thin layer of cadmium, which helps block hydrogen absorption which can lead to stress cracking.

In addition to cadmium, zinc, and aluminum coatings, nickel-chromium and cobalt-chromium are used as corrosive coatings because of their low level of porosity (Song et al 2017). They are extremely moisture resistant and therefore help inhibit the development of rust and the eventual deterioration of the metal. Oxide ceramics and ceramic metal mixes are examples of coatings that are strongly wear-resistant, in addition to being corrosion resistant (Keshri et al 2010). The ceramics such as alumina, zirconia, titania,

etc., are some of the oxide ceramics which are more suitable as corrosion-resistant materials. However, the porosity, which is invariably introduced in the coatings, makes a pathway for electrolytes to penetrate from the top surface to the carbon steel substrate. Therefore, the reduction of porosity in the plasma sprayed coatings play a significant role in improving the corrosion resistance.

The potential application of different nanostructured materials in corrosion protection, prevention and control is a subject of increasing interest. The nano-materials such as single-walled and multi-walled CNTs, graphene and graphene oxide nanoplatelets (GNP), are used in corrosion protection too. GNP reinforcement into the ceramic material coatings may overcome this problem by being impermeable by covering the matrix with graphene oxide sheet, thereby preventing the penetration of electrolyte into the coatings and also to the substrate.

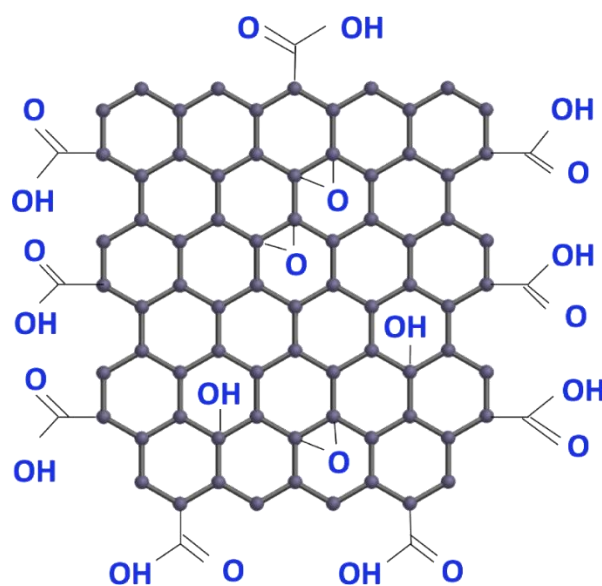


Fig. 1.6 Schematic representation of graphene oxide structure (source: www.acsmaterial.com)

Graphene is the sp^2 hybridized carbon atoms arranged in a hexagonal array in two-dimensional lattices (Geim & Novoselov 2007, Rafiee et al 2012) as shown in **Fig. 1.6**. It has an extraordinary chemical-tunability, electrical, mechanical, optical, physical, and thermal properties (Ye et al 2015). Because of these extraordinary properties, graphene is the building block of numerous applications such as electronic devices, bio devices,

optoelectronics, sensors and nanostructured ceramic composites for anticorrosion and anti-wear applications (Ding et al 2018).

These coating materials can be coated on the carbon steel substrate using various coating techniques based on the type of coating material and application in which the material is used.

1.2.4 Corrosion Resistant Coatings Techniques

Coatings can be used for improving the corrosion resistance of underlying base metals, as an alternative to costly corrosion-resistant materials. A low-cost base metal plate or casting, with the required yield and tensile strength, can be considered for coating with highly corrosion-resistant materials, using different coating methods to enhance its corrosion resistance to seawater. The use of this coated low-cost base metal for the fabrication of new components working in seawater applications like pump casings, pump impellers, valve bodies, and valve blades would result in major cost savings to industry. Further coated components which have undergone seawater corrosion can be replaced with new coatings using in-situ coating processes. This immediate, in-situ and low-cost repair of corroded components, after years of service in seawater environment, is a major requirement of the industry.

The corrosion coatings have been prepared using different techniques such as sol-gel, electrodeposition, Physical Vapor Deposition (PVD), Chemical Vapor Deposition (CVD), plasma electrolytic oxidation (PEO) (López-Ortega, Arana, et al. 2018) and thermal spray techniques including Vacuum Plasma Spray (VPS), Atmospheric Plasma Spray (APS), High-Velocity Oxyfuel (HVOF), detonation gun, etc. Thermal spray techniques are most preferred methods because of many advantages like relatively thicker coatings can be obtained, the substrate is not affected, the thickness can be adjusted, can be deposited on different shaped components, onsite deposition is feasible in large scale and is low cost. The detailed explanation for the various thermal sprayed techniques used for coating of corrosion-resistant materials is explained in the upcoming section.

1.2.4.1 Thermal Spray Coatings

Thermal Spray is a generic term for a group of coating processes used to apply metallic or nonmetallic coatings (Toma et al 2010). These processes are grouped into three major categories: flame spray, electric arc spray, and plasma arc spray. These energy sources are used to heat the coating material (in powder, wire, or rod form) to a molten or semi-molten state. The resultant heated particles are accelerated and propelled toward a prepared surface by either process gases or atomization jets. Upon impact, a bond forms with the surface, with subsequent particles causing thickness buildup and forming a lamellar structure (**Fig. 1.8**) (Kim et al 2005).

Characteristics of Thermal Spray Coatings

The high particle temperatures and speeds achieved in thermal spray process result in significant droplet deformation on impact at a surface, producing thin layers or lamellae, often called “splats,” that conform and adhere to the substrate surface. Solidified droplets build up rapidly, particle by particle, as a continuous stream of droplets impact to form continuous rapidly solidified layers. Individual splats are generally thin (~1 to 20 μm), and each droplet cools at very high rates ($>10^6$ K/s for metals) to form uniform, very fine-grained, polycrystalline coatings or deposits.

Fig. 1.6 shows a schematic of a generic thermal spray powder consolidation process, illustrating the key features and a typical deposit microstructure. Sprayed deposits usually contain some level of porosity, typically between 0 and ~10%, some unmelted or partially melted particles, fully melted and deformed “splats,” metastable phases, and oxidation from entrained air. Thermal spray process jets or plumes are characterized by large gradients of both temperature and velocity. Feedstock is usually in powdered form with a distribution of particle sizes. When these powdered materials are fed into the plume, portions of the powder distribution take preferred paths according to their inertia. As a result, some particles may be completely unmelted and can create porosity or become trapped as “unmelts” in the coating. Use of wire and rod feedstock materials produces particle size distributions because of non-uniform heating and unpredictable drag forces, which shear molten material from the parent wire or rod. The level of these coating

defects varies depending on the particular thermal spray process (**Fig. 1.8**) used, the operating conditions selected, and the material being sprayed (Bobzin et al 2012).

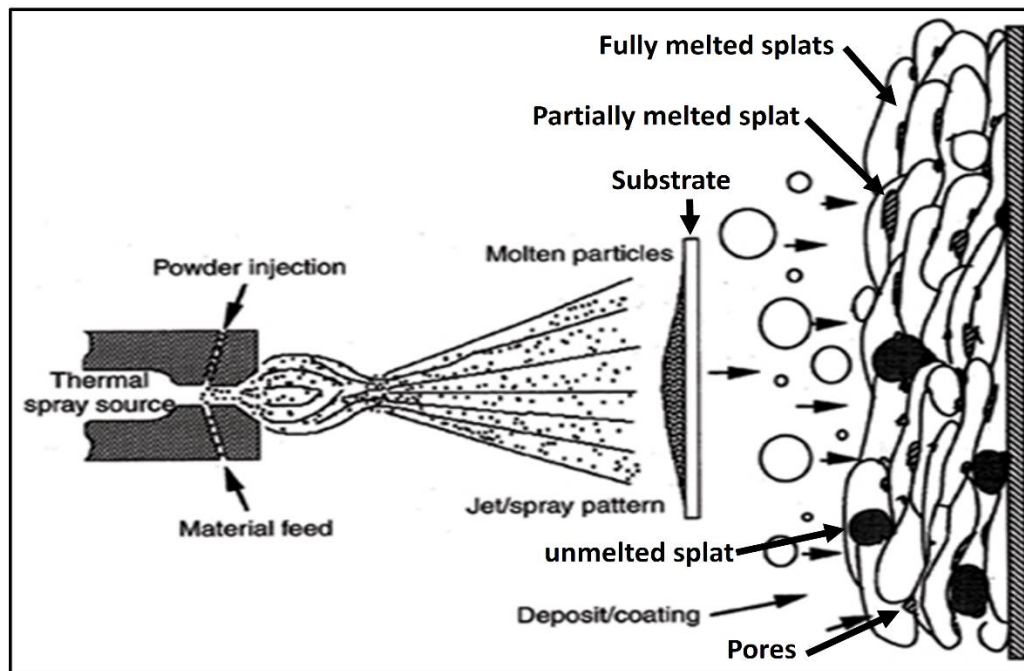


Fig. 1.7 Schematic representation of thermal spray process
(<https://empoweringpumps.com>)

Advantages of thermal spray coating

- Less capital cost
- Requires less floor space
- Wastes from thermal spray are not toxic
- Easy disposal of waste
- Better bonding characteristics
- Wider range of materials can be coated
- Improved wear and corrosion resistance
- Higher hardness
- Thick coating capability
- Larger components can be coated
- Portability

Types of thermal Spray Techniques:

There are several different types of Thermal Spray Coating processes as shown in **Fig. 1.8**. They differ in how they apply thermal and kinetic energy to the source material, the form of the source material (powder or wire) and the relative velocities and temperatures of the flame. Each process has advantages and disadvantages, and some are optimized for certain types of coatings. We are concentrating on the Wire Arc like Weld Overlay, High Velocity Oxy-Fuel (HVOF) and Atmospheric plasma spray (APS) techniques are discussed mainly since these techniques are exclusively used for our work.

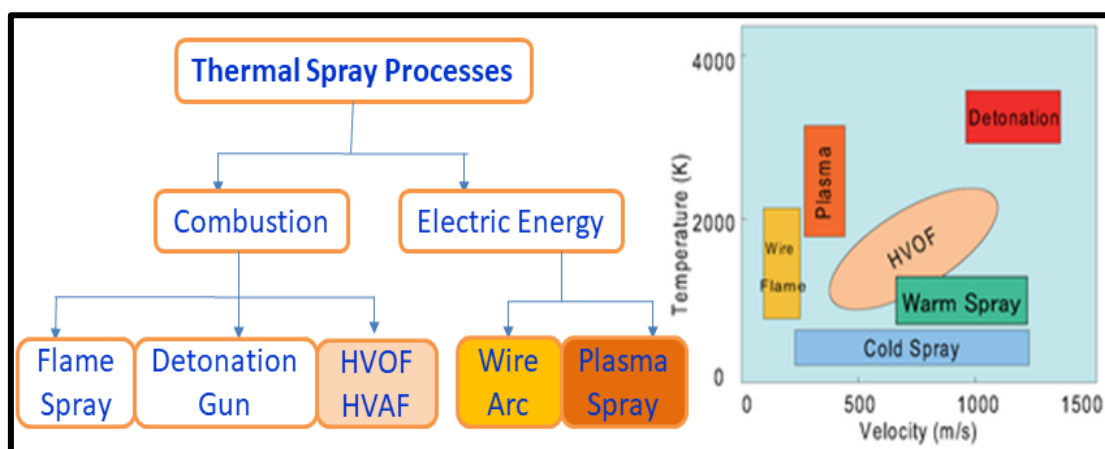


Fig. 1.8 Schematic representation of types of thermal spray process

2.1.1 Weld Overlay Coating

Welding Overlay is the process of depositing welding beads on a base metal as shown in **Fig. 1.9** to improve its surface properties like, mechanical, wear resistance and corrosion resistance. The common weld overlay processes employed to deposit weld beads include: Gas Tungsten Arc Welding Overlay Process (GTAW) and Shielded Metal Arc Welding Process (SMAW).

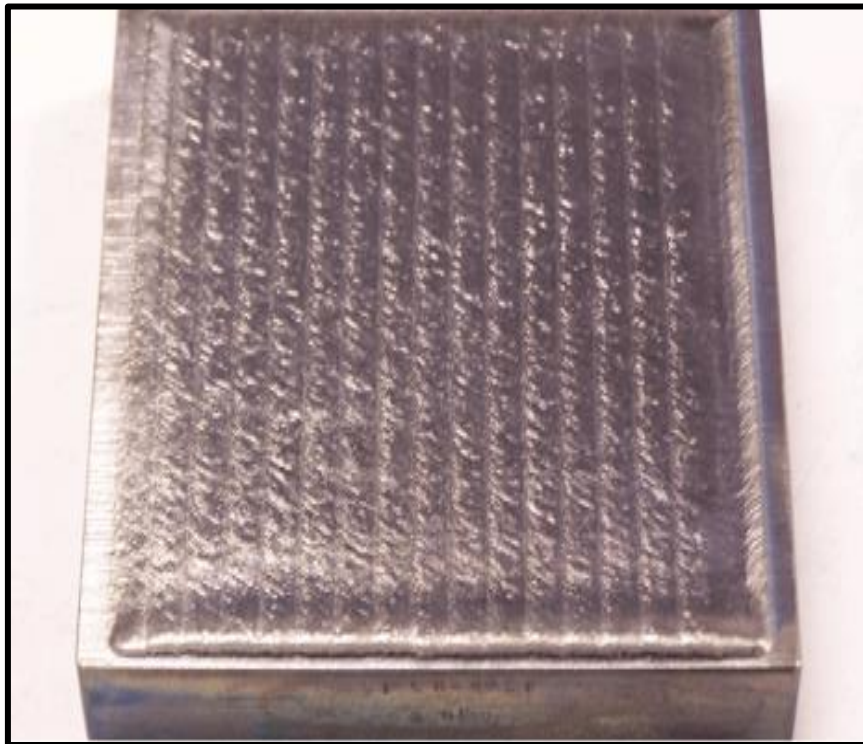


Fig. 1.9 Weld overlay of the filler material on the substrate.

GTAW WO coating:

In the GTAW WO Process (**Fig. 1.20(a)**), a tungsten electrode is used to strike an arc with base metal, while a filler wire deposits the weld metal on the surface of base metal. Argon shielding is used to protect the deposited weld metal from oxidation by atmospheric air.

SMAW WO coating:

In the SMAW WO Process (**Fig. 1.20(b)**), an electrode core wire with flux coating is used to strike an arc with base metal. The electrode wire melts and deposits weld metal on the surface of base metal. As the weld metal is deposited, the flux coating of the electrode disintegrates, providing a shielding gas and a layer of slag, both of which protect the weld oxidation by atmospheric air until it cools. The slag floats to the top of the deposited weld metal and can be easily removed.

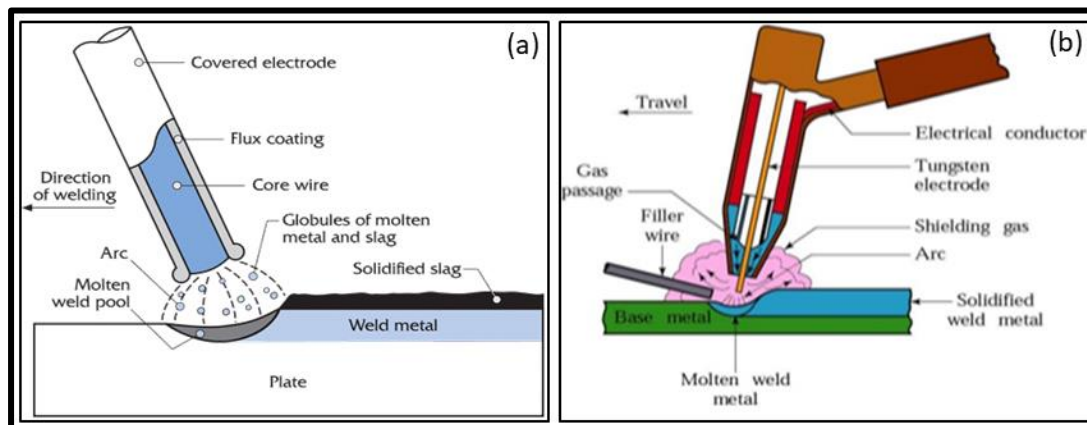


Fig. 1.20 Schematic representation of a) GTAW and b) SMAW processes.

The advantages of deposition by weld overlay process are:

- Low worker skill requirement for deposition of weld on base metal.
- Portable method for deposition of weld on base metal and can be employed in component rectification work at project sites.
- Low Cost Process for deposition of weld on base metal.
- Very good adhesion of weld metal to base metal
- Deposition material is in form of wires and is easily available

2.1.2 High-Velocity Oxy-Fuel (HVOF) spray process

HVOF processes involve both thermal and kinetic energy transfer because of the melting and accelerating forces felt by the deposited particles. The HVOF process **Fig. 1.21** works by confining combustion gases and particles in a high-pressure chamber to create a high-velocity jet. Fuel gas, such as propane, acetylene, and oxygen are fed into a combustion chamber and ignited. The jet travels through the nozzle and an extended confining barrel to generate a supersonic gas jet with high particle velocity. The feedstock powder can be fed into the system axially or radially, entrained into the high velocity jet, and accelerated through the barrel to deposit onto a substrate.

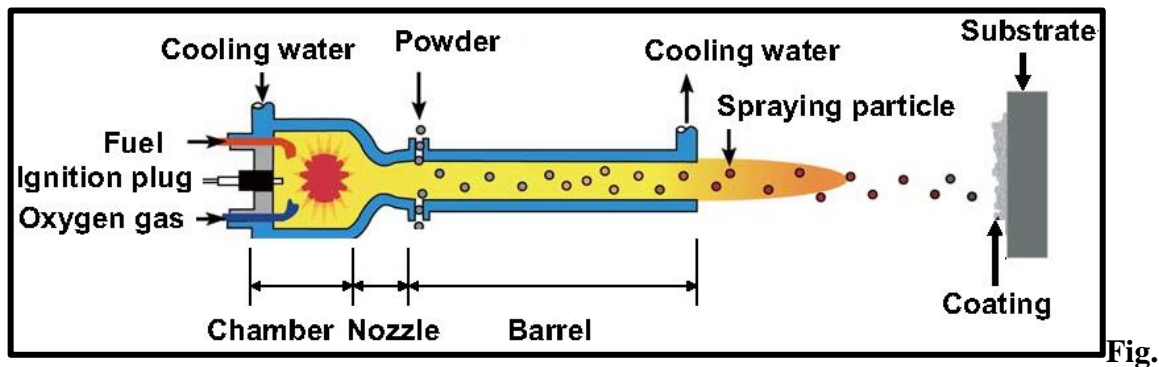


Fig.

1.21 Schematic representation of standard HVOF process system.

Advantages HVOF spray coating

- Higher density (lower porosity) due to greater particle impact velocities
- Higher strength bond to the underlying substrate and improved cohesive strength within the coating
- Lower oxide content due to less in-flight exposure time
- Retention of powder chemistry due to reduced time at temperature
- Smoother as-sprayed surface due to higher impact velocities and smaller powder sizes
- Higher hardness due to less degradation of carbide phases specific to a system
- Improved corrosion protection due to less through thickness porosity

Disadvantages of HVOF spray coating

- Coatings can be extremely complex, with their properties and microstructure depending upon numerous processing variables
- Powder sizes are restricted to a range of about 5 - 60 μm , with a need for narrow size distributions
- Deposition of coatings is difficult or impossible to achieve on to internal surfaces of small cylindrical components, or other restricted access surfaces because HVOF spraying needs line of sight to the surface and a spray distance of 150-300 mm.

2.1.3 Atmospheric Plasma Spray (APS) process

Atmospheric plasma spray belongs to a family of processes called thermal spray. The plasma spray process consists of forming the plasma jet, which interacts with the particles

(Kim et al 2005). The plasma jet provides thermal and kinetic energy to the material to be deposited by directing it to a substrate to produce coating as in **Fig. 1.22**.

The principal components of the plasma spray systems are plasma torch, process control, power supply, gas supply, material feeder (powder or liquid), and dynamic sample holder. The main element of a plasma spray system is the plasma torch, which is responsible for converting electric energy into thermal energy, necessary for material processing. A process control console allows adjustment of the operating parameters, i.e., the control of arc current, arc ignition, plasma gas flow rates, material, and carrier gas flow rates. The additional systems necessary for operation are the plasma gas supply system, the power supply system (including the high-frequency starter unit), the high-pressure cooling water system, and the material (powder or solutions) feed system. The systems also have mechanical equipment (sample holder) to control relative motion between the plasma torch and the substrate. Another important step in the deposition process is material injection, which is mainly influenced by the injection method, feed system type, and the characteristics of the material. The injection method may be radial or axial.

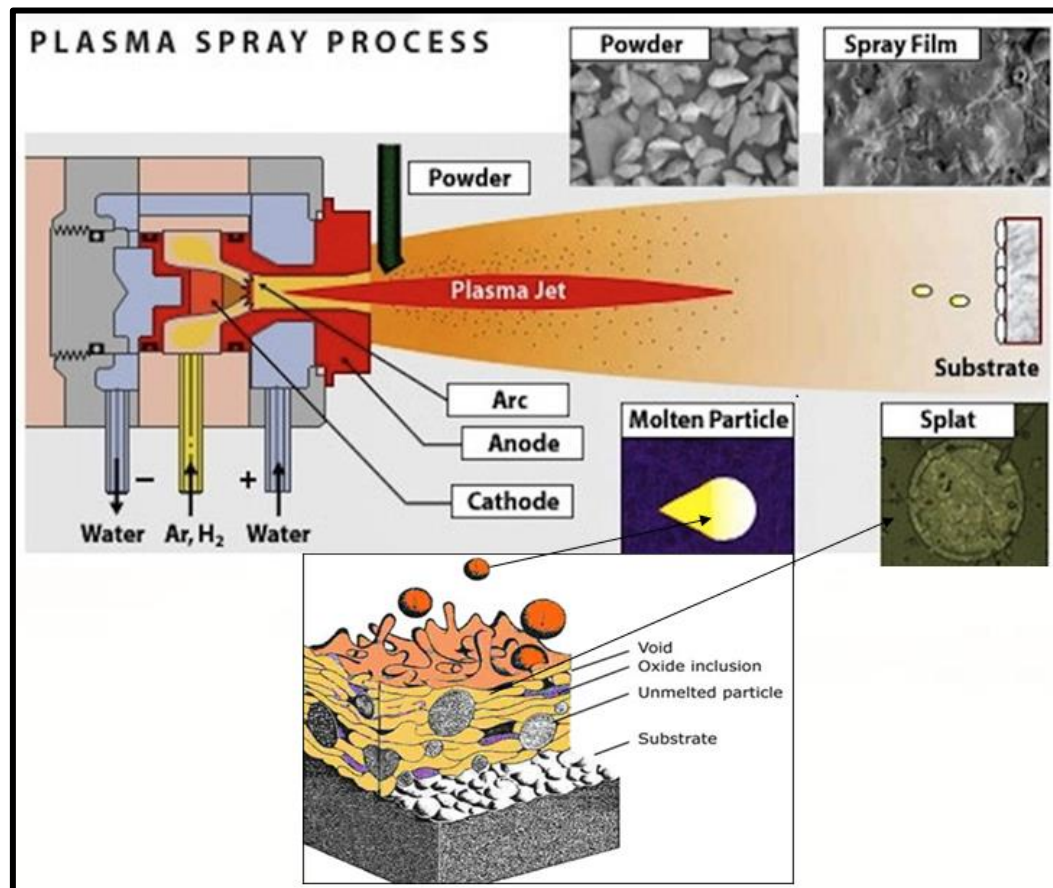


Fig. 1.22. Schematic Representation of Atmospheric Plasma spray process

In the deposition process of plasma spray, the substrate is usually prepared to receive the coating by performing cleaning procedures (removing oils and greases), inducing surface roughness, preheating, and controlling movement. The adhesion of the particles to the substrate and between the lamellae strongly depends on the preparation of the substrate, preheating temperature, and morphology and composition of the material. Preheating, generally performed with the plasma jet itself, is a key point and has to be controlled according to the size and thickness of the part to be coated. Substrate and coating temperatures, either for preheating or during deposition, are linked to the residual voltage distribution, which is a controlled parameter.

The input parameters and the operational characteristics of the plasma spray process are described in **Table 1.1**. The input parameters are controlled during the experiment and, therefore, are independent variables. However, the operational characteristics often depend on the combination of the input parameters, thus, they are dependent variables.

Table 1.1 The main parameters of APS process

Parameters	Torch	Plasma Jet	Particles	Substrate
Input parameters	Current		Size distribution	Substrate material
	Plasma gas composition		Morphology	Pre-heat treatment
	Flow rate		Feed rate	Motion/ Speed
	Nozzle design, erosion		Carrier gas flow rate	Distance
	Cooling flow			
Operating Characteristics	1.Voltage	Stability	Particle trajectory	Coatings properties
	2.Voltage fluctuations	Geometry	Particle temperature	Porosity
	3.Thermal efficiency	Plasma gas composition	Particle Distribution	Mechanical properties
	4.Torch set up	Atmosphere Pressure Humidity		Deposition

Advantages of APS process

- There are a range of different materials that can be used as a quality coating using plasma spraying. Most materials are available in the suitable powder form such as metals, ceramics and alloys, and can be individually selected depending on the substrate.
- Plasma spraying can coat many different substrate materials such as plastics, glass, metals and ceramics.
- Compared to other types of thermal spraying, plasma spraying can use a wide range of powder particle sizes between 5-100µm.
- Plasma spraying provides effective coatings that act as a protective barrier to a substrate, ensuring the material has a high resistance and is insulated and controlled.

Disadvantages of the APS process

- Equipment can be expensive
- The internal components of the plasma gun can experience deterioration due to the high temperatures and they will need replacing fairly regularly to maintain the consistency of the coating.

1.2.5 Wetting properties

Various types of anticorrosive coatings have been developed, including ones that prevent the contact of the material with a corrosive environment, such as aqueous solutions. A relatively new type of coating which repels water and aqueous solutions is the hydrophobic coating which modifies wetting properties of a material. The wetting of solids by liquids is influenced by the surface tension of the components involved. Thomas Young established formula in 1805 which characterizes the surface tension at the three-phase contact of a droplet on a solid (Drelich et al 2019). The contact angle (CA) between a liquid and a solid is widely used as a criterion to evaluate the wettability (**Fig. 1.23 (a)**). Hydrophilic surfaces have a water CA less than 90° (**Fig. 1.23(e)**) while hydrophobic surfaces have a water CA greater than 90° (**Fig. 1.23(f)**). For an ideally smooth homogenous surface, the equilibrium CA (θ_Y) of a liquid droplet (say, of water) is given by the Young's equation

$$\gamma_{lv} \cos \theta_Y = \gamma_{sv} - \gamma_{sl} \quad [1.6]$$

Where θ_Y is Young's contact angle, γ_{lv} , γ_{sv} and γ_{sl} are the liquid-vapor interfacial tension, solid-vapor interfacial tension and solid/liquid interfacial tensions.

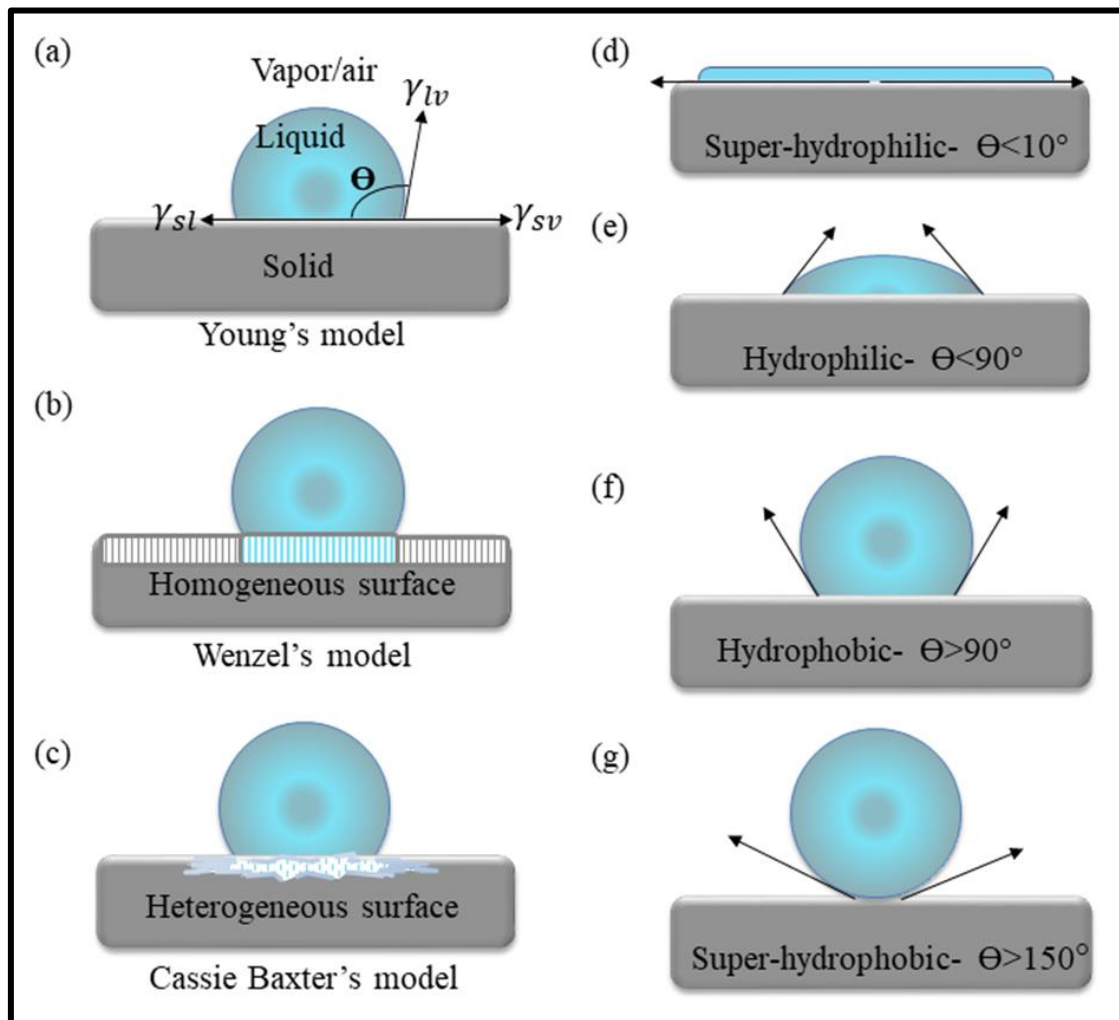


Fig. 1.23 Schematic representation of different wetting models [(a), (b) and (c)] and wetting behaviour [(d), (e), (f) and (g)].

However on real surfaces, which are rough and heterogeneous, the contact angle is different from the equilibrium value. The effect of roughness and chemical heterogeneity on the CA is incorporated into two well-known models of wetting, namely the Wenzel (**Fig. 1.23** (b)) and Cassie–Baxter models (**Fig. 1.23** (c)).

Contact angle hysteresis (CAH), which is the difference between the maximum CA (advancing CA, e.g., in front of a moving droplet) and the minimum CA (receding CA, e.g., at the rear of a moving droplet) is a parameter used to characterize the adhesion between a liquid and a surface. Surfaces that exhibit a water CA greater than 150° and very low CAH ($<10^\circ$) are said to be super-hydrophobic (**Fig. 1.23**(g)). But there are a number of important exceptions, and sometimes called the ‘petal effect’. While the CA

characterizes wetting during normal loading, CAH characterizes wetting during shear loading at the solid-liquid interface. Adhesion under both these types of loadings can be measured separately using the centrifugal adhesion balance. Besides water-repellency, the super-hydrophobic surfaces have many emerging applications such as self-cleaning, drag reduction in water flow, antifouling, ice-phobicity, oleophobicity, water filtering, etc. One newly emerging area of application for hydrophobic and super-hydrophobic surfaces is corrosion inhibition.

The super-hydrophobic surfaces and coatings can fundamentally change how water interacts with surfaces, and the fact that earth is a water world, it can legitimately be said that this technology has the potential to literally change the world.

There are a number of recent experimental studies of how hydrophobicity can reduce corrosion, although there are few studies of the fundamental physicochemical mechanisms involved or potential applications to freshwater materials. Typically, electrochemical corrosion occurs when a metallic surface is oxidized while in contact with an electrically conducting solution called an electrolyte. A hydrophobic/super-hydrophobic surface with a non-homogeneous interface would have a reduced interfacial contact area between the electrolyte and the metallic surface.

Applications of hydrophobic coatings are useful in

- Water repellency
- Anti-corrosion
- Desalination
- Anti-bio-fouling
- Anti-icing
- Self-cleaning optical windows and lenses
- Viscous drag reduction

1.2.6 Mechanical properties of the coatings

The quality of the coating is of prime importance. In addition to corrosion resistance, there are many mechanical properties such as bond strength, brittleness, elastic modulus, fracture toughness, microhardness, shear modulus, and residual stress will govern the

quality of the coatings. The microhardness, brittleness and fracture toughness are the key mechanical properties of a coating. Indentation is the most popular technique to measure microhardness. There are numerous indentation techniques available. Vicker's hardness technique is quite popular due to its non-destructive nature, simplicity, and minimal machining requirement to prepare the sample. Indentation hardness is a measurement of the size of an indentation made by a diamond pyramid-shaped indenter of specified size and shape pressed into a polished surface by a known load as shown in **Fig. 1.24**. The surface is normally not etched prior to the indentation. It has the four-fold symmetry but makes a deeper indentation and is more inclined to cause fractures in brittle materials than the other types. Therefore, in our present study the Vickers indentation technique is used to study fracture toughness, microhardness and brittleness index of the coatings and the substrate. Fracture toughness is calculated using the crack length obtained by the indentation with higher loads.

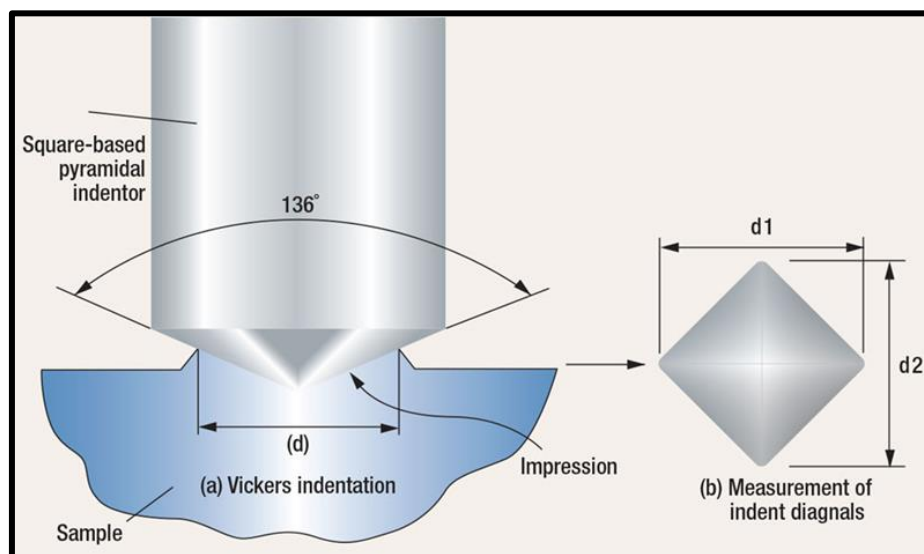


Fig. 1.24 Schematic representation of the Vicker's Indenter

1.3 Literature review

Details of literature review carried out on various articles published on metallic thermal spray coatings with finite element analysis simulation, ceramic- metal matrix composite coatings and ceramic nanocomposite thermal spray coatings are summarized.

1.3.1 The literature on metal alloy coatings.

The fabrication of components working in seawater applications like pump impellers, pump casings, valve bodies, and valve blades are of carbon steels (Levy et al 2017, Okano et al 2016). But, pitting and general corrosion is very frequently experienced in materials used for components working in seawater (Levy et al 2017) . This requires the use of costly corrosion-resistant materials like stainless steel viz. SS-309Mo, Duplex Stainless Steel, Inconel-625, Inconel-718, Hastelloy-C276 and Hastelloy-C22 for fabricating components (Ghosh & Ramgopal 2005, Pawel 1993, Tang et al 2013). Among these, nickel-based alloys are the most important corrosion-resistant materials (Li et al 2016, Zhang & Liu 2016). Since nickel dissolves many elements in its solid solution owing to a wide variety of applications (Li et al 2015, Silva et al 2016). The alloy Inconel-625 (UNS N0662) has very good weldability, high creep strength, high yield strength, tensile strength, good oxidation resistance and has excellent resistance to pitting and crevice corrosion (Moradi & Ketabchi 2015, Xu et al 2013). In view of the discovery of its excellent corrosion resistance to a variety of corrosive environments, it became an important alloy in several different industries such as aerospace, aeronautical, marine industries, petrochemical, oil and gas industries (Silva et al 2016). The Cr, Mo, Nb, and W are the important elements responsible for its resistance to harsh corrosive environments. The presence of Nb and Mo in the Nickel-chromium matrix makes Inconel 625 a special alloy (Shao et al 2017).

A paper on “Laser cladding of Inconel 625 wire for corrosion protection” is reported by (Abioye et al 2015) in which the corrosion performance of the coating is evaluated. The stainless steel exhibited localised (pitting) corrosion however, it was fully protected by the Inconel 625 wire laser coating in the saline solution.

An article on " Microstructural and mechanical properties of resistance spot weld of Inconel 625 supper alloy” is presented by (Rezaei Ashtiani & Zarandooz 2016). This study was carried out to evaluate the microstructural and mechanical properties of resistance spot-welded Inconel 625 alloy. The effects of welding parameters on the mechanical properties of the spot weld in terms of peak load, fracture energy, and failure mode were investigated.

An article “Corrosion of Incoloy 800H alloys with nickel cladding in FLiNaK salts at 850 °C” is published by (Dai et al 2018). The corrosion of 800H alloy with and without Ni-cladding, as well as GH3535 alloy, in molten FLiNaK salts at 850 °C has been investigated. Results show that Cr and Fe are depleted from the alloys surface and grain boundaries, where “diffusion paths” are formed. The corrosion process is mainly controlled by the redox reaction of impurity metal ions with Fe and Cr at the alloy surface.

A report entitled “Modeling of the residual stresses in plasma-spraying of functionally graded ZrO₂/NiCo CrAlY coatings using finite element method” is reported by (Zhang et al 2005). Their major conclusion was the thermo-mechanical behaviours and the distribution of residual stresses in functionally graded ZrO₂/NiCo CrAlY coatings due to thermal spraying were analyzed by thermo-mechanical finite element analysis (FEA) can be used to optimize the design and processing of some plasma-spraying coating.

An article “Modeling residual stresses generated in Ti-coatings thermally sprayed on Al₂O₃ substrates is reported by (Zimmerman et al 2013). They concluded that the magnitude of residual stresses in the Ti-coating increases with its thickness, reaching a maximum of 200 MPa in the thickest coating.

A study on the “ANSYS Simulation of Residual Strains in Butt-welded joints” by (Atroshenko et al 2014) and they calculated residual strains in welding using numerical modelling.

The article “Numerical Simulation of Similar and Dissimilar Materials Welding Process; Quantifications of Temperature, Stress, Strain and Deformation” (Ranjit 2015) reports a 3-Dimensional welding simulation was carried out using ANSYS in order to predict temperature, stress, strain and deformation in the joining of similar and dissimilar materials.

In addition, extensive research on estimating residual stress using simulation techniques like ANSYS birth and death analysis has been carried out on butt and fillet welds used for joining plates and pipes (Hashemzadeh et al 2015, Ranjbarnodeh et al 2011, Zhu et al 2010). But, no papers are available which estimate and analyze residual stresses in

multilayer, multi-process hybrid coating deposition using ANSYS Analysis for reduction in residual stresses in base materials like Low Carbon Steel.

However, it is very expensive to fabricate the components of Inconel-625 on a large scale. A thin layer of this alloy can be coated on a low-cost base material such as low carbon steel with the required yield and tensile strength to enhance its corrosion resistance property and reduce the cost (Kim et al 2015). Weld overlay is one of the thermal spray coating techniques used to manufacture and repair the industrial components. In the weld-overlay process, a thin layer of material is deposited over a base material to improve its properties (Kang et al 2017, Singh et al 2018, Sowrirajan et al 2018). But, the higher residual stresses induced during welding or mismatch of thermal coefficients, micro-crack propagation, and formation of precipitates are problems that leads to premature failure of components (Okano et al 2016, Yu et al 2017). Therefore, choosing a proper welding method to coat is also very important to avoid distortion of the welding structure and the unacceptable microstructure. There is a gap in existing research on methodology of improvement of seawater corrosion resistance of low-cost base materials like Low Carbon Steel through application of multiple coating layers by a combination of optimum cost-effective processes and techniques.

1.3.2 Literature on cermet and ceramic-graphene composite coatings

Carbon-based nanocomposite materials play a significant role in improving the corrosion resistance, because of its enhanced mechanical, microstructural and electronic properties (Chen et al 2018, He et al 2018, Xiong et al 2016). In addition, some of the nanocomposites show hydrophobic properties with improved corrosion protection (Barai et al 2018, Chen et al 2018, Nagy et al 2007, Venkateswara Rao & Ranjith Kumar 2018).

An article “Role of Powder Treatment and Carbon Nanotube Dispersion in Fracture Toughening of Plasma-Sprayed Al_2O_3 -Carbon Nanotube Nanocomposite” reports that Al_2O_3 ceramic reinforced with 4-wt% multiwalled carbon nanotube (CNT) is plasma sprayed on AISI 1020 low carbon steel for improving the fracture toughness of coating (K Balani et al 2007).

An article entitled “Wear Behavior of Plasma-Sprayed Carbon Nanotube-Reinforced Aluminum Oxide Coating in Marine and High-Temperature Environments” reports a relative improvement in the wear resistance of Al₂O₃-8 wt% CNT coating compared to Al₂O₃ was 72% at 298 K, 76% at 873 K, and 66% in seawater (A. K. Keshri et al 2011).

NT Kirkland et al. in 2012 published a manuscript “Exploring graphene as a corrosion protection barrier” and they found that the graphene coated layer substantially reduces the aqueous corrosion rate of nickel and copper substrates.

M. N. Hussain et al in the year 2014 reported an article on the effect of Plasma spray nanocomposite coating on Mild Steel”. This report gave an inference that the addition of Graphene powder to Al₂O₃:13%TiO₂ has resulted in lower Microhardness and can be used in applications with the bending load. Also, if graphene content increased the electrical and thermal conductivity increases.

Jian Chen Hu et al. in 2014 wrote a review article on the use of Graphene as a Protective Coating against Corrosion. They concluded that the ultra-dense network of carbon atoms that form graphene is totally impermeable to protect the material from corrosion, and at the same time, it is so thin that it keeps unaltered the chemical properties of the protected material.

N. W. Pu et al. in 2015 grown Graphene on stainless steel for ecofriendly anticorrosion coating for polymer electrolyte membrane fuel cell bipolar plates. Graphene coating was carried out by the CVD technique. The pre-plated nickel layer can help graphene completely cover the stainless steel surface. The graphene coating on stainless steel has enhanced its anti-corrosion property.

A. S. Sai Pavan and Sutapa Roy Ramanan in 2016 conducted a study on corrosion-resistant graphene films on low alloy steel. The graphene oxide was prepared by the modified Hummers method and they coated on low alloy steel by dip-coating method. Three layers of graphene films were able to reduce the corrosion rate by 99 %.

Andy Nieto et al. in 2016 reported a review article on Graphene reinforced metal and ceramic matrix composites. This review critically examines the current state of graphene

reinforced metal (GNP-MMC) and ceramic matrix composites (GNP-CMC). The use of graphene as reinforcement for structural materials is motivated by their exceptional mechanical/functional properties and their unique physical/chemical characteristics.

Česánek, Z., et al. (2018) reported an article “High-temperature corrosion behavior of selected thermally sprayed coatings in corrosive aggressive environment” (Česánek et al 2018). The Stellite6 and Cr₃C₂-25% NiCr coatings were deposited using HP/HVOF thermal spraying technology. The corrosion test was conducted in the corrosive-aggressive environment of molten salts mixture in the composition of 40% Na₂SO₄-60% V₂O₅, simulating the corrosion environment of boilers for residual fuel oils. The corrosion test under cyclic conditions included 50 cycles at the temperature of 750 °C and subsequent cooling at the room temperature for 20 min.). In comparison with Cr₃C₂-25% NiCr coating, both Stellite6 and Hastelloy C-276 coatings provided the substrate material with sufficient protection against high-temperature corrosion. The corrosion mechanism of Hastelloy C-276 coating was based on the formation of protective oxide layer which prevented further penetration of corrosive media. Stellite6 coating exhibited the corrosion attack along splat boundaries resulting in spat delaminating into the build-up. The corrosion mechanism of Cr₃C₂-25% NiCr coating included the attack on NiCr matrix resulting in gradual separation of carbide phases into the corrosive environment.

Jin, B., et al. in 2019 presented an article “Enhanced corrosion resistance in metal matrix composites assembled from graphene encapsulated copper nanoflakes”. Corrosion protection of metals is of great importance due to their widespread use. Graphene (Gr) has shown promising corrosion resistance as a coating for metals, however, its excellent strengthening effect that has been widely shown is suppressed in such coating applications.

This literature suggests that the graphene is one of the wonder anticorrosion material and can be used as the second phase material in the ceramic materials to make composite to increase the corrosion resistance and to improve mechanical properties. Also the amount of graphene or graphene oxide content in graphene reinforced ceramic matrix composites plays a crucial role.

1.4 Scope and objectives of the work

1.4.1 Scope of the Work

There is a scope to improve the sea water corrosion resistance of base material like Low Carbon Steel which are widely used in various industries as mentioned in previous section, because of its low cost and advantages like weldability, machinability etc. There are different coating materials and coating techniques to improve the corrosion resistance and mechanical properties of the low carbon steel.

The current study may help to bridge this gap by finding the better coating materials in metal alloys, ceramic-metal matrix composite or ceramic-nanocomposite with different coating techniques. A combination of coating processes like high velocity oxy fuel (HVOF), atmospheric plasma spray (APS) , gas tungsten arc welding overlay (GTAW), shielded metal arc welding overlay (SMAW) and a combination of coating materials like stainless steel such as SS-309Mo, nickel alloy such as Inconel-625, ceramic-graphene composite and ceramic metal composite called cermet.

These combination of coatings and coating materials will enhance the sea water corrosion resistance of low cost, low corrosion resistant like Low Carbon Steel (IS 2062 Grade B), thereby resulting in huge savings to industry, which are currently using very costly materials like Inconel-625 or Hastelloy-C276 for new equipment in sea water applications.

Further, these coatings can also be used for renovation of old equipment which has corroded during operation in sea water environment, resulting in extension of their service life by a few more years. This will be helpful to industry in reducing equipment down-time and improving productivity.

s

1.4.2 Objectives of the Present Work

1. To improve corrosion resistance of low cost base materials like Low Carbon Steel (IS 2062 Grade B) with different coating materials such as metal alloy, ceramic metal composite and ceramic-nanocomposite using thermal spray coating techniques.

2. To select optimum weld overlay technique and coating material (between super alloy Inconel-625 and SS-309Mo) on low carbon steel coating using ANSYS thermal and mechanical stress analysis through reduction in residual stresses.
3. Coating the material suggested by the best model selected from ANSYS simulation on low carbon steel using weld overlay technique.
4. To coat the low carbon steel with ceramic metal matrix composite and ceramic-nanocomposite (GNP-Ceramic composite) by thermal spray technique.
5. To characterize the structural, morphological and compositional features of the substrate with and without coatings.
6. To investigate the corrosion, wetting and mechanical properties of the substrate with and without coatings.

CHAPTER 2

Experimental Details

CHAPTER 2

EXPERIMENTAL DETAILS

Overview

In this chapter, the ANSYS simulation used for weld overlay coating, spray drying procedure for composite powder preparation, thermal spray coatings such as Weld Overlay (WO) coating, HVOF and APS processes are described. The experimental conditions used for characterization of the samples using x-ray diffraction (XRD), scanning electron microscopy (SEM)/Field Emission SEM (FESEM), energy dispersive x-ray analysis (EDS), Raman Spectroscopy, Fourier Transfer Infrared (FTIR) Spectroscopy and X-Ray Photoelectron spectroscopy (XPS) are briefly explained. The porosity of the coatings are explained with the help of Brunauer, Emmett and Teller (BET) surface analysis. The investigation of corrosion behavior of the samples by three electrode electrochemical setup (Biologic SP150), mechanical property by Clemex's microhardness tester and wetting properties by Holmarc's contact angle meter are discussed.

Acknowledgment note: We acknowledge IIT-Patna for APS facility and Spray Met-Bangalore for HVOF coating facility.

2.1 Materials

2.1.1 Substrate and coating materials

Table 2.1. Composition of the substrate and the coating material

Material & form	C	Mn	P	S	Si	Cr	Mo	Ni	Fe	Nb
BM (metal plate)	0.22 (max)	1.50 (max)	0.045 (max)	0.045 (max)	0.40 (max)	-	-	-	Rem	-
SS-309 Mo (metal rod)	0.12 (max)	1.0- 2.5	0.030 (max)	0.030 (max)	0.30- 0.65	23.0- 25.0	2.0-3.0	12.0- 14.0	Rem	-
Inconel-625 (metal rod)	0.10 (max)	0.50 (max)	0.015 (max)	0.015 (max)	0.50 (max)	20.0- 23.0	8.0- 10.0	58.0 (min)	5.0 (max)	3.15- 4.15
Cermet (powder)	75%NiCr-25%Cr ₂ C ₃									

Ceramic	<i>I.</i>	α -Al ₂ O ₃ , α -Al ₂ O ₃ -(0.5, 1, 1.5 and 2 wt%)GO
composites	<i>II.</i>	ZrO ₂ , ZrO ₂ -(0.5, 1, 1.5 and 2 wt%)GO

(powder)

Rem–Remaining; min–Minimum; max–Maximum

The substrate used for depositing coating material is low carbon steel conforming to the Indian standard IS-2062 Grade-B (BM) which is equivalent to ASTM standard A36 low carbon steel. The reported data on chemical composition (weight %) is given in **Table 2.1**. Different coating materials such as metal alloy (Inconel-625), ceramic-metal composite (75NiCr-25Cr₂C₃), Alumina-Graphene oxide composite and Zirconia-Graphene oxide composites are coated on the substrate using different coating techniques. The composition of the coating materials are also given **Table 2.1**.

2.2 Synthesis of Composites for coating

2.2.1 Synthesis of Graphene Oxide (GO) by Hummers method

The raw materials like Graphite flake, H₂SO₄, NaNO₃, NaOH, KMnO₄ H₂O₂ (30%), and HCl were purchased from Sigma-Aldrich (USA). All the chemicals were of analytical reagent grades and are used as received condition, without any further purifications.

Graphene oxide is synthesized by employing modified Hummers' method as shown in **Fig. 2.1**. Briefly, 1:1 ratio of graphite powder and NaNO₃ are mixed in 25 mL of concentrated H₂SO₄ for 30 min using a magnetic stirrer. Then, 6 times of graphite powder amount of KMnO₄ is slowly added into the above solution along with stirring while maintaining the temperature of the solution below 20 °C using an ice bath. The reaction mixture is stirred until oxidation is completed, and color of mixture changes from violet to violet brownish. After that, 140 mL of deionized (DI) water is added slowly while maintaining the temperature of the reaction to 95 °C using a water bath to achieve a dark brown solution. The reaction is completed by adding 30% H₂O₂ solution dropwise, which makes solution bright yellow indicating the formation of GO. The as-prepared GO is repeatedly washed using ethanol, diluted HCl and DI water until the pH of the solution became neutral. After a thorough cleaning, the sample is dried at 60 °C for 24 hours.

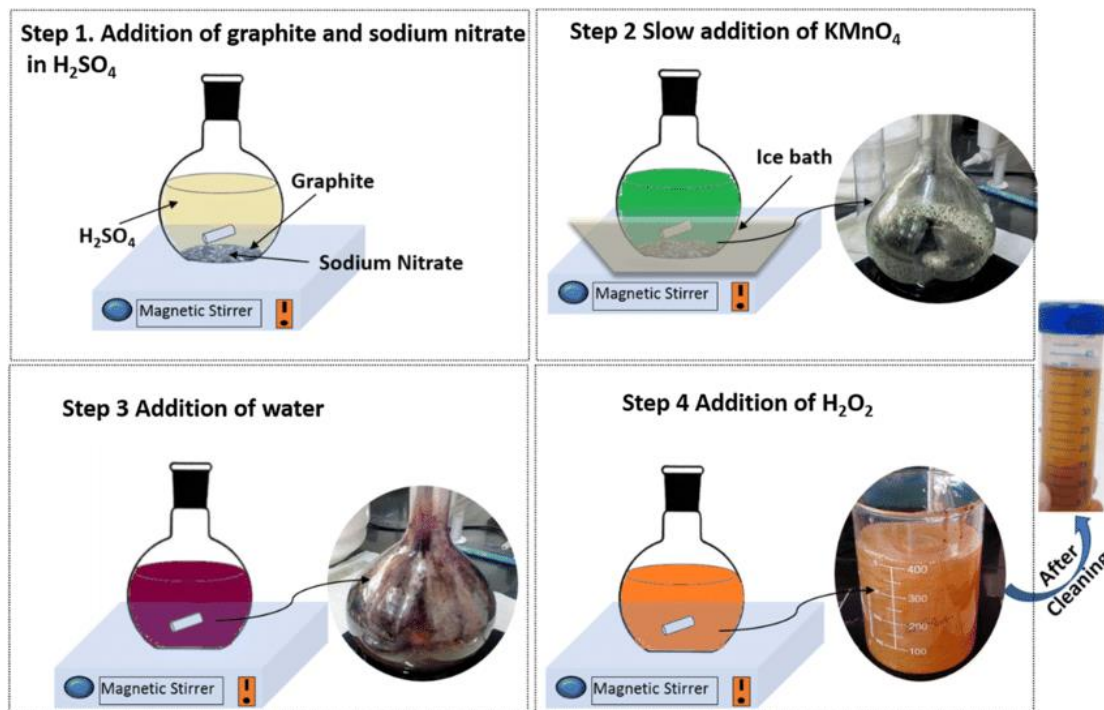


Fig. 2.1 Schematic representation of stepwise synthesis graphene oxide by Hummer's method (Pareek et al 2019).

2.2.2 Synthesis of Composite powder by Spray Drying process

In all processes implemented to manufacture ceramic powders, the resulting size distribution is generally not adapted to that requested for spraying. Very often, and especially with crushing, grinding, milling, etc., many fine particles (below $5\ \mu\text{m}$ average diameter) are produced, which are not usable for conventional spraying without agglomerating them. Beside to produce cermet particles, it is necessary to mix rather fine ceramic and metal or alloy particles and form granules of their mixtures as shown in **Fig. 2.2**.

Spray-drying technique is one of the most versatile ones to manufacture particles usable in spray processes from small diameter particles. In spray-drying, agglomerated powders are produced from suspensions (often water-based) called slurry. Fine droplets of suspension are atomized into a drying chamber where they are heated by a stream of hot air or by the radiation of the hot chamber wall or both in some cases. The rapid heat and mass transfers which occur during drying combined

with the presence of various slurry compounds result in dried granules. These granules present large shape varieties: uniform solid spheres, elongated spheres, pancake shaped, donut shaped, needle-like, or hollow granules (Goyal et al 2017). In order to keep quasi-spherical shapes, particles are sintered in rotating furnaces where diffusion occurs within particles but not between themselves. In some other cases, particles are only calcinated; i.e., fired or heated at a temperature high enough to eliminate volatile constituents (which could induce otherwise the de-agglomeration of particles upon penetration in the hot gas spray stream). However, calcinated particles generally result in poor quality coatings (structural heterogeneity, large size distribution of voids, etc.).

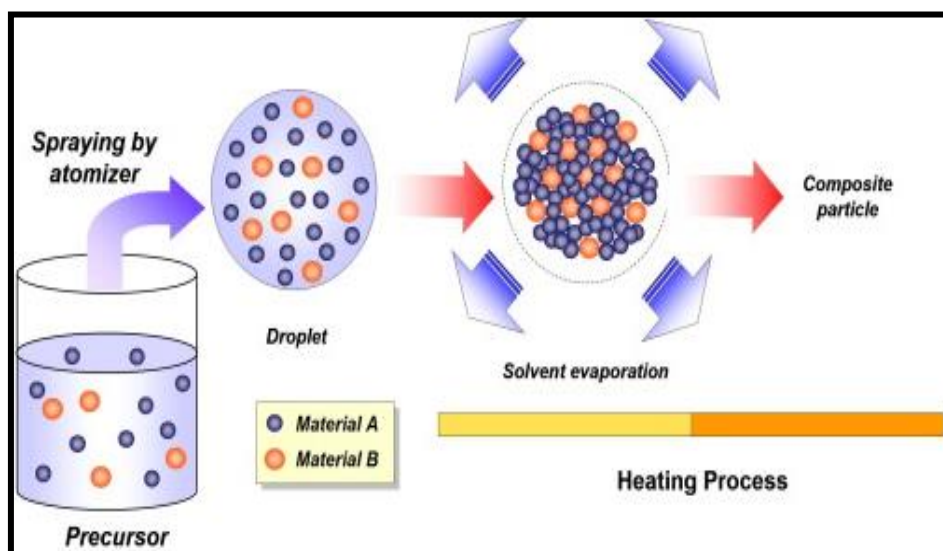


Fig. 2.2 .Schematic representation of spray drying process [pub.rsc.org]

- ✓ The input temperature was controlled such that output temperature is between 95 °C–100 °C.
- ✓ The atomizer pressure was held at 16 psi and feed was between 1.5 to 2 litres per hour.
- ✓ The solid density was about 50–60 wt%.
- ✓ The feed stocks had hollow disc like and solid spherical shapes.

- ✓ The average particle size of the spray dried powders are in the range of 20–70 μm .
- ✓ The different materials like 75NiCr-25Cr₂C₃, α -Al₂O₃, α -Al₂O₃-(0.5, 1, 1.5 and 2 wt%)GO, ZrO₂, ZrO₂-(0.5, 1, 1.5 and 2 wt%)GO composites are prepared via spray drying process.

2.3 Coating methods

2.3.1 Weld Overlay coating

For weld coating SS-309Mo and Inconel-625 materials are selected for weld overlay coatings on low carbon steel. SS-309Mo is chosen as buffer coating layer because of its low cost, higher chromium and nickel contents, and ability to tolerate 25% dilution by low carbon steel. After dilution by substrate as demonstrated by Shaeffler diagrams, SS-309Mo will still retain its ductile austenitic structure with 4-10% ferrite, and does not become brittle (Zhao et al 2019). The presence of ferrite in the weld overlay will also help in preventing hot cracking of SS deposit. This is due to higher solubility of impurity elements in ferrite, leading to less inter-dendritic segregation of low melting point impurities and less cracking tendency (Liu et al 2020). Inconel-625 material is chosen as the top coating layer because of its excellent corrosion resistance to sea water, as shown by its high Pitting Resistance Equivalent Number (PREN) of around 51 PREN formula for Stainless Steel and Nickel Alloys is as shown in eqn. 2.1 (Kartsonakis et al 2016) (Wang et al 2011).

$$\text{PREN} = \% \text{Cr} + 3.3 \times (\% \text{Mo}) + 16 \times (\% \text{N}) \quad (2.1)$$

2.3.1.1 ANSYS simulation for selection of best WO coating

The multilayer coating process on substrate CS, with dimensions 50 mm x 40 mm x 6 mm is simulated using a finite element model developed using ANSYS. The first and second deposited weld overlay layer thickness is 2 mm each. Total coating thickness is 4 mm, which provides adequate component life in corrosive environment.

The eight-node brick elements are used in meshing the finite element model. To simulate moving heat source element, ANSYS birth and death technique is used. Element type SOLID70 is used for thermal transient analysis, which has a temperature as a single degree of freedom at each node. For structural transient analysis, element type SOLID185 with three translational degrees of freedom at each node is used.

Table 2.2 IS-2062 Grade-B Temperature Dependent Properties (ASME, 2015)

Temperature (Kelvin)	Density (Kg/m ³)	Specific Heat (J/Kg/K)	Linear coefficient of thermal expansion (K ⁻¹) x 10 ⁻⁵	Thermal Conductivity (W/m/K)	Yield Stress (MPa)	Young's Modulus (GPa)	Poisson Ratio
294	7880	444.0	1.098	64.60	250	206.8	0.295
366	7880	452.4	1.152	63.15	227	196.5	-
477	7800	511.0	1.224	55.24	213	194.4	0.300
589	-	561.3	1.296	49.87	194	186.0	-
700	7760	611.6	1.350	44.79	166	169.0	-
811	-	661.8	1.404	39.71	150	117.0	-
922	7600	762.3	1.458	34.86	-	55.0	0.315
1033	7520	-	1.405	30.46	30	6.9	0.320
1144	-	1005.3	1.305	28.37	-	-	-
1255	7390	-	-	27.62	-	-	0.327
1366	-	-	-	28.52	-	-	-
1477	7300	1189.6	-	-	-	-	0.335
1673	7250	-	-	-	-	-	0.341

Table 2.3 SS-309Mo Temperature Dependent Properties (ASME, 2015) (Bureau of Indian Standard Publication, 2011)

Temperature (K)	Density (Kg/m ³)	Specific Heat (J/Kg/K)	Linear coefficient of thermal expansion (K ⁻¹) x 10 ⁻⁵	Thermal Conductivity (W/m/K)	Yield Stress (MPa)	Young's Modulus (GPa)	Poisson Ratio
273	8039	456	1.570	13.29	350	200.0	0.26
373	7997	494	1.650	14.99	-	192.0	-
473	7954	523	1.690	16.62	262	184.0	-
573	7910	544	1.730	18.19	238	176.0	0.29
673	7864	560	1.767	19.72	221	168.0	0.34
773	7817	573	1.778	21.26	200	160.0	0.33
873	7769	584	1.812	22.81	-	152.0	0.32
973	7720	597	1.843	24.42	172	144.0	0.31
1073	7669	613	1.872	26.09	148	135.0	0.30
1173	7617	635	1.899	27.86	120	127.0	-

1273	7563	664	1.927	29.76	-	119.0	-
1373	7509	702	1.953	31.81	-	105.0	-
1473	7453	752	1.979	34.03	-	20.0	-
1573	7396	815	2.002	36.46	-	7.0	-
1673	7355	869	2.021	38.29	-	5.6	-

Table 2.4 Inconel-625 Temperature Dependent Properties (ASME, 2015) (Bureau of Indian Standard Publication, 2011)

Temperature (K)	Density (Kg/m ³)	Specific Heat (J/Kg/K)	Linear coefficient of thermal expansion (K ⁻¹) x 10 ⁻⁵	Thermal Conductivity (W/m/K)	Yield Stress (MPa)	Young's Modulus (GPa)	Poisson Ratio
294	8440	410	-	9.8	330	204.8	0.308
366	8414	427	1.28	10.8	290	200.6	0.310
477	8398	456	1.31	12.5	265	193.7	0.312
589	8365	481	1.33	14.1	260	187.5	0.313
700	8332	511	1.37	15.7	255	180.6	0.312
811	8278	536	1.40	17.5	-	173.1	0.321
922	8211	565	1.48	19.0	245	165.5	0.328
1033	8112	590	1.53	20.8	225	157.2	0.329
1144	-	620	1.58	22.8	200	148.2	0.330
1200	-	-	1.62	-	-	-	-
1255	-	645	-	25.2	100	-	-
1366	-	670	-	-	-	-	-

Temperature dependent material properties of IS-2062 Grade-B low carbon steel, SS-309Mo and Inconel-625 given in **Table 2.2**, **Table 2.3** and **Table 2.4** respectively which are used in ANSYS transient thermal and structural analysis, for evaluation of residual stress in the base material. The standard reference temperature for thermal strain calculations is taken as 293K.

The mesh model used in the analysis for substrate plate with two layers of weld deposition is shown in **Fig. 2.3(a)**. The first coating layer on substrate is SS material of 2 mm thickness, while the second coating material Inconel-625 is of 2 mm thickness. **Fig. 2.3(b)** shows the moving heat source due to the welding process. ANSYS thermal and structural program was developed to simulate this coating process layer by layer. Each weld layer consisted of 200 elements. In the ANSYS birth and death analysis, the coating elements are first killed and then given birth to one by one with time, to simulate the welding process. In the alternate skip welding technique adopted (**Fig. 2.3(a)**), the elements are given birth in column wise from 1 to

20 in the first layer, then skipping elements 21 to 40 in the next column and then elements 41 to 60 are given birth, and the welding process continues. The black arrow mark in **Fig. 2.3(a)** shows the direction of welding progress, starting with element 1 and proceeding to 20, then welding 41-60, 81-100, 121-140, 161-180 in the first series. After completing the first series of skip welding, the next series of giving birth to elements 21 to 40 (blue arrow) is started. Thus, the first layer is deposited by alternate skip welding. The process is then repeated for depositing the next layer of coating. This technique of alternate skip welding is used for obtaining low residual stresses in the coatings.

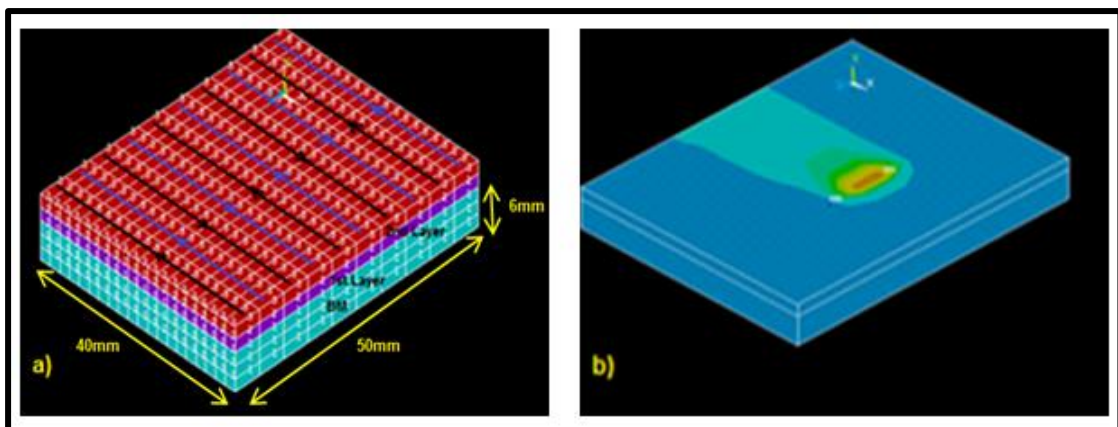


Fig. 2.3 (a) ANSYS Model of skip welding of first and second layer (weld coatings on substrate with dimensions) and (b) moving heat source due to welding

Heat is generated in these elements one by one as they take birth, due to the input of welding current and voltage and then dissipated as the welding progresses to other elements. Finally, on completion of welding, convection is applied on the weld top and side surfaces with a natural convection heat transfer coefficient of $5 \text{ W/m}^2/\text{K}$ and the weld deposits are cooled to room temperature of 308 K.

Twelve different models are simulated using the combination of two coating materials Inconel 625 and SS-309Mo on substrate, two weld overlay technique GTAW (Gas Tungsten Arc Welding) and SMAW (Shielded Metal Arc Welding), substrate thickness and substrate preheat temperature. The best model with low residual stress is chosen for weld overlay coating.

2.3.1.2 Weld Overlay Coating of SS-309-Mo and Inconel-625 on Substrate

The best model among 12 different model has been chosen for WO deposition. The GTAW which is a low heat input method is used for deposition of 2 mm thick SS-309Mo as a first layer which acts as buffer layer on substrate to minimize the dilution. The SMAW which is a high heat input method is used for weld overlay deposition of 2 mm thick Inconel-625 on the top surface of 2 mm thick SS-309Mo weld overlay deposition. Total coating thickness is 4 mm, which provides an adequate component life in the corrosive environment (Al-Fozan & Malik 2008). In addition, an alternate Skip welding technique is used in each weld overlay type in order to reduce the residual stresses as mentioned earlier. Henceforth, the substrate IS2062 grade B carbon steel is termed as (CS). The weld overlay deposition of stainless steel SS309Mo (SS) on the CS is termed as SSCS. The weld overlay deposition of Inconel 625 (I) on top of SS309Mo (SS) weld overlay and CS is termed as ISSCS. **Fig. 2.4** shows the thickness of different layers and the material codes used to represent these layers.

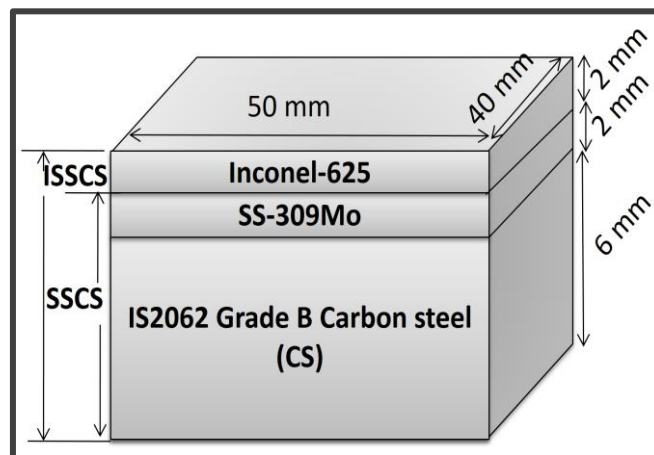


Fig. 2.4. Schematic representation of weld overlay deposition of SS-309Mo and Inconel625 on the substrate (CS).

The steel plate bottom surface is placed on a non-conducting base to reduce the rapid dissipation of heat, which will increase residual stresses. The sides of base plate are tack welded to prevent movement and distortion of base plate. The welding current, welding voltage, welding speed and heat input used for depositing the weld material

are given in **Table 5**. The welding heat input is calculated using welding efficiency (N), welding speed (S), Current (I) and Voltage (V), as shown in equation 2, adopted from TWI (The Welding Institute, UK). The Welding Heat generated per unit volume is then calculated based on weld metal volume deposited per unit time (Quintino et al 2013).

$$\text{Welding Heat Input} = \frac{N \times I \times V}{S}$$

(2.2)

Table 2.5. Welding Parameters for Weld Deposition.

Parameters	Welding Process	
	GTAW	SMAW
Welding Consumable Size (mm)	2.4	3.2
Current (I) (Ampere)	90	120
Voltage (V)	10	25
Welding Speed (mm/sec)	2	2
Welding Efficiency (N %)	60	80
Welding Heat Input (KJ/mm)	0.27	1.20
Welding Heat Generated (W)	540	2400
Heat generated per unit volume. (W/mm ³)	27	120

2.3.2 Coating of 75Cr₃C₂-25(NiCr) cermet by HVOF process

A commercially available 25(NiCr)-75Cr₃C₂ cermet powder with particle size of -45/+15micron and having spherical profile was used in this study. Deposition of the cermet powder onto mild steel substrate was done by HVOF process at M/s Spraymet, Bangalore (India). An average coating thickness of 180 micron was deposited on the substrate. For the coating of cermet- (75Cr₃C₂-25(NiCr)) on the substrate the process parameters used by the HVOF process are depicted in the **Table 2.6**.

Table 2.6. The HVOF process parameters used for coating of 75Cr₃C₂-25(NiCr)

Process parameters	Value
1. Operating power	72 KW
2. Current	3000 A
3. Voltage	24 V
4. Primary gas flow rate	20 l/min
5. Secondary gas flow rate	200 l/min
6. Spray distance	250 mm
7. Powder feed rate	25 g/min

2.3.3 Coating of Alumina-xGO and Zirconia-xGO (x- 0.0, 0.5, 1.0, 1.5 and 2.0 wt.%) composites by APS process

In the present work Alumina- xGO composite and Zirconia-xGO (x- 0.0, 0.5, 1.0, 1.5 and 2.0 wt.%) composites are coated using APS coating. Prior to plasma spray coating, the substrate was grit blasted with 20 grit size alumina to get uniform surface roughness. Then the substrate was degreased and cleaned via ultrasonicator in water and ethanol and was preheated for better adhesion of the coatings. The spray dried powders were sprayed on the substrate using 9 MB plasma gun (Oerlikon Metco, Switzerland) to deposit coatings. The thickness the coatings is about 300 μ m. The optimized plasma spray process parameters used to prepare the composite coatings are enlisted in **Table 2.7** and **Table 2.8** for alumina-GO and Zirconia-GO composites.

Table 2.7. Atmospheric Plasma Spray process parameters employed for Alumina-xGO composite coatings.

Parameters	Value((units)
Substrate preheat temperature	200 ($^{\circ}$ C)
Powder feed rate	13 (g/min)
Stand-off distance from substrate	100 (mm)
Current	510 (A)

Voltage	66 (V)
Secondary gas flow, Hydrogen	11 (SCFH*)
Primary gas flow, Argon	110 (SCFH*)

*SCFH-Standard Cubic Feet per Hour

Table 2.8. Process parameters used for plasma spray deposition of Zirconia-xGO composites coatings.

Process Parameters	Value
Current	500 A
Voltage	65-70 V
Primary gas	Argon
Flow rate and pressure of Argon	85 SCFH* and 110 psi
Secondary gas	Hydrogen
flow rate and pressure of Hydrogen	16 SCFH* and 50 psi
Powder feed rate	40 g/min
Spray distance	2" to 3"

2.4 Characterizations of the samples

All the coatings and the substrate are subjected to their structural, functional, morphological, compositional and surface porosity characterizations with the help of various techniques. The instrumental models and parameters used for characterization are briefly given in upcoming sections.

XRD: The structural analysis of all the samples were performed using Rigaku miniflex 600 XRD. The XRD patterns of all the samples were recorded using Cu-K α (1.5406 Å) radiation, in continuous scan mode with the scanning rate of 2° min⁻¹ from 3° to 90° and x-ray generator power is set at voltage of 40 kV and 15 mA current. The XRD patterns of all the samples were analyzed and indexed using JCPDS data with the help of Xpert High score plus software

Raman Spectroscopy: Raman Spectra of the samples were recorded using spectrometer (SEKI Technotron corp Model:STR-300) with a spectral resolution of 0.75 cm^{-1} by exciting the samples using a laser source of 785 nm (monochromator with Grating-600 g mm^{-1}) having confocal depth resolution of 2 μm .

FTIR: The spray dried alumina, zirconia and its composites with graphene oxide are pelletized with KBr and are subjected to FTIR analysis using Shimadzu FTIR spectrometer.

XPS: Chemical composition of the samples were determined using XPS (SPECS), using non-monochromatic Al $K\alpha$ radiation (1486.8 eV). The binding energies reported here were calculated with reference to C1s peak at 284.6 eV with a precision of 0.1 eV. All the samples were sputter cleaned for 5 min using an ion beam for XPS measurements.

FESEM and EDS: The morphology and compositional analysis of the samples were done using FESEM and EDS with mapping (ZIESS, Sigma HD, UK)) operated at 5 kV.

TEM: The HR-TEM (JEOL 2100 microscope) was used for imaging the high-resolution lattice fringes of the samples with an operating voltage of 200 kV. The d-spacing and the corresponding SAED pattern of samples using HR-TEM.

BET: The specific surface area and pore diameter of the samples were evaluated using the BET method from the nitrogen adsorption-desorption isotherms obtained using a BELSORP mini II instrument (BEL Japan Co., Ltd).

2.5 Study of corrosion, mechanical and wetting Properties of the samples

2.5.1 Electrochemical Corrosion properties of the coatings

All corrosion is an electrochemical process of oxidation and reduction reactions. As corrosion occurs, electrons are released by the metal (oxidation) and gained by elements (reduction) in the corroding solution. Because there is a flow of electrons (current) in the corrosion reaction, it can be measured and controlled electronically.

Therefore, controlled electrochemical experimental methods can be used to characterize the corrosion properties of metals and metal components in combination with various electrolyte solutions.

The electrochemical corrosion testing method is used for study the corrosion resistance properties of the coatings and the substrate. Prior to the electrochemical corrosion test, the samples were prepared as per ASTM Standard E3-11 (Shrestha et al 2001). The three electrode system electrochemical test method similar to ASTM Standard G61 was used for detecting the corrosion resistance using Biologic SP150 workstation as shown in **Fig. 2.5**. The Saturated Calomel Electrode (SCE) and Platinum (Pt) wire were used as reference and the counter electrode respectively. The coating and substrate samples were used as the Working Electrode (WE). Only the coated surface of the working electrode was exposed to 3.5 wt. %NaCl electrolyte (equivalent to sea water) prepared according to ASTM standard G5 (Balan et al 2018), which acts as the corrosion medium (pH = 7.7 at room temperature of 22 °C). In order to retain the solution chemistry, each test was conducted with fresh electrolyte. The Linear polarization resistance (LPR) and electrochemical impedance spectroscopy (EIS) techniques are used for corrosion evaluation of the coatings and the substrate.

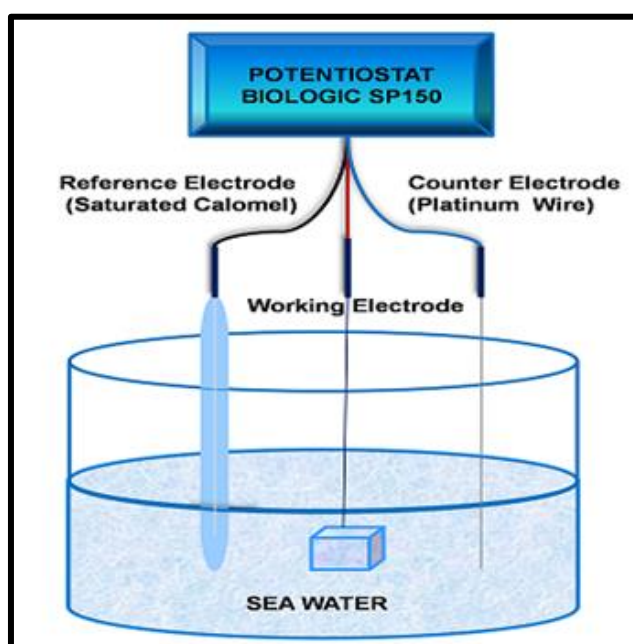


Fig. 2.5. Schematic representation of three electrode electrochemical set up.

2.5.1.1 LPR: This tests were carried out with a potential ramp of 50 mV around an equilibrium potential, at a given scan rate of 0.166 mVs⁻¹. The electrochemical corrosion parameters have been obtained using the linear polarization curve. The polarization resistances were calculated using the current density and the Tafel slopes. The polarization resistance (R_p) and the corrosion rates (CR) were expressed in mmpy, which was determined from the Tafel extrapolation method using the equation 2.3 and 2.4.

$$R_p = \frac{\beta_a \beta_c}{I_{corr} \times 2.303 (\beta_a + \beta_c)} \quad (2.3)$$

$$CR = \frac{K_1 I_{corr} EW}{\rho A} \quad (2.4)$$

Where I_{corr} is known as the corrosion current density ($\mu A/cm^2$), β_a and β_c are the anodic and cathodic branch of Tafel slopes respectively. K_1 is the corrosion unit (3272 mmpy) and EW is referred to as the equivalent weight of the coating material (g), ρ is the density (g/cm^3) and A (cm^2) is the area of the surface exposed.

2.5.1.2 EIS: The EIS tests were is carried out using an AC signal of 10 mV amplitude, in the frequency range from 100 mHz to 200 kHz and the corresponding Nyquist plots and Bode plots were analyzed. The Nyquist plots were fitted to get the equivalent circuit and the corresponding fitting elements are tabulated.

2.5.2 Mechanical properties of the coatings

The microhardness of the coatings and the substrate are measured using Clemex micro-hardness tester (Clemex Technologies Inc. Canada) with Vickers indenter (**Fig. 2. 6**) at a particular load and dwell time. Vickers Hardness (H_v) of coatings and substrate are measured using equation 2.5 (Matthews et al 2003)

$$H_v = 1.854 \frac{P}{d^2}$$

(2.5) Where, P is the applied load in gram force (N) and d is the diagonal length measured in micro-meter (μm). The Vicker's hardness (H_v) is converted to GPa by a conversion factor 0.009807.

The crack length of the coatings is obtained with higher loads. The fracture toughness K_{IC} of the plasma sprayed coatings are calculated using the equation 2.6

$$K_{IC} = \frac{P}{C^{\frac{2}{3}}(\beta_0)}$$

(2.6)

Where K_{IC} is the fracture toughness in MPa m^{1/2}, P is the load applied in gram force (N), C is the crack length in μm and β_0 is a constant =7 for Vicker's indenter.

The brittleness index (Bi) of the coatings is calculated from the fracture toughness K_{IC} and hardness (H_v) of the coatings and the substrate using the following equation 2.7

$$Bi = \frac{H_v}{K_{IC}}$$

(2.7)



Fig. 2.6 Photograph of Clemex microhardness tester.

2.5.3 Wetting properties of the coatings

The sessile drop technique is used to quantify the contact angle for the all coatings and substrate samples using Contact angle meter (Model: HO-IAD-CAM-01) procured from Holmarc Opto-mechatronics Pvt.Ltd which is shown in **Fig. 2.7**. This is an advanced model with automated dispenser, rotatable substrate holder and temperature controller. The contact angle meter comprises a motorized micro-syringe

pump for the precise dispensing of the droplet, a source of light projected on a sessile water droplet of on the sample which is dispersed from the micro-syringe and high-speed camera interface for measuring the CA of liquids on solid surfaces.

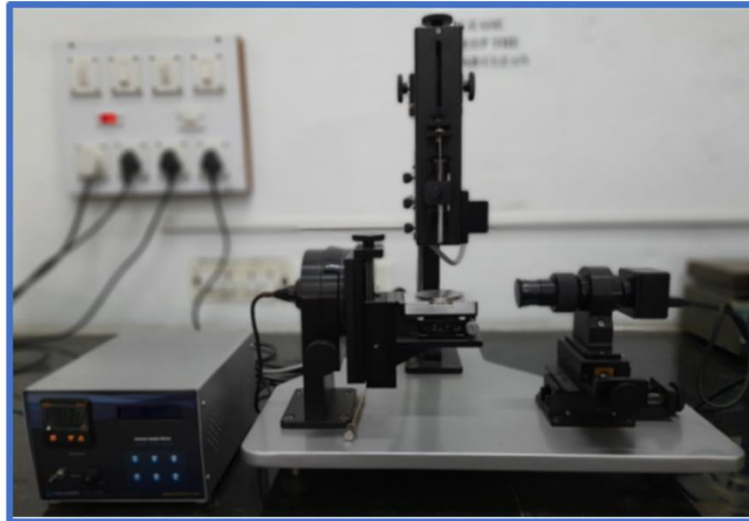


Fig. 2.7. Photograph of the Holmarc's Contact angle meter.

The contact angle of any liquid drop on the coating surface is defined as the mechanical equilibrium of the liquid drop under the action of three interfacial tensions (γ_{lv} , γ_{sv} and γ_{sl}) and is called as Young's equation 2.8 (Makkonen 2016).

$$\gamma_{lv} \cos \theta_Y = \gamma_{sv} - \gamma_{sl}$$

(2.8)

Where θ_Y is the Young's contact angle, γ_{lv} , γ_{sv} and γ_{sl} are the liquid vapour interfacial tension, solid vapour interfacial tension and solid/liquid interfacial tension respectively.

In the present work

- Solid- top surface of the coatings and the substrate
- Liquid- 10 μ l of 3.5wt.% NaCl salt solution
- Vapour- air.

CHAPTER 3

Weld overlay of Inconel-625 on the substrate with SS-309Mo as buffer layer: Corrosion, mechanical and wetting properties.

Outcome

1. “Finite Element Analysis of Thermal Residual Stresses in SS-309Mo and Inconel-625 Multilayer Hybrid Coatings on Low Carbon Steel” **International Journal of Fatigue-Elsevier**
2. “Corrosion protection of low-cost carbon steel with SS-309Mo and Inconel-625 bimetallic weld overlay” January 2019, **Material Research Express-IOP**
3. “Electrochemical impedance behaviour of SS-309Mo and Inconel 625 weld overlay on carbon steel at different applied voltages” **AIP Conference Proceedings**

CHAPTER 3

Weld overlay of Inconel-625 on the substrate with SS-309Mo as buffer layer: Corrosion, mechanical and wetting properties.

Overview

In this chapter, the ANSYS FEA simulation is used for the selection of the best configuration with low residual stress for the weld overlay of Inconel-625 on a substrate with SS-309Mo as a buffer layer. The best model has been coated using the weld overlay method. The results obtained by XRD and SEM characterization are discussed. The investigation of the corrosion behavior of the samples by three-electrode electrochemical corrosion test using EIS and LPR techniques are discussed. The stability of the anti-corrosion coatings is studied using Immersion tests. The mechanical property of the coatings is also studied.

3.1. Introduction

The fabrication of components working in seawater applications like pump impellers, pump casings, valve bodies, and valve blades are of carbon steels (Levy et al., 2017; Okano et al., 2016). But, pitting and general corrosion is very frequently experienced in materials used for components working in seawater (Ghosh and Ramgopal, 2005; Lillard et al., 1994). This requires the use of costly corrosion-resistant materials like stainless steel viz. SS-309Mo, Duplex Stainless Steel, Inconel-625, Inconel-718, Hastelloy-C276, and Hastelloy-C22 for fabricating components (Pawel, 1993; Tang et al., 2013; Totolin et al., 2016). Among these, nickel-based alloys are the most important corrosion-resistant materials (McLouth et al., 2018; Patel et al., 2016; Singh et al., 2018; Zhang and Liu, 2016). Since, nickel dissolves many elements in its solid solution enables it for a wide variety of applications (Li et al., 2015; Rodriguez et al., 2017; Silva et al., 2016). The alloy Inconel-625 (UNS N0662) has very good weldability, high creep strength, high yield strength, tensile strength, good oxidation resistance and has excellent resistance to pitting and crevice corrosion (Dinda et al., 2009; Moradi and Ketabchi, 2015; Xu et al., 2013). In view of the discovery of its excellent corrosion resistance to a variety of corrosive environments, it became an important alloy in several different industries such

as aerospace, aeronautical, marine industries, petrochemical, oil and gas industries (Silva et al., 2016). The Cr, Mo, Nb, and W are the important elements responsible for its resistance to harsh corrosive environments. The presence of Nb and Mo in the alloy makes Inconel 625 a special alloy (Shao et al., 2017).

However, it is very expensive to fabricate the components of Inconel-625 on a large scale. A thin layer of this alloy can be coated on a low-cost base material such as low carbon steel with the required yield and tensile strength to enhance its corrosion resistance property and reduce the cost (Kim et al., 2015). Weld overlay is one of the thermal spray coating techniques used to manufacture and repair the industrial components. In the weld-overlay process, a thin layer of material is deposited over a base material to improve its properties (Kang et al., 2017; Singh et al., 2018; Sowrirajan et al., 2018). The thin surface material has superior properties over the base material and protects it from various types of deterioration such as corrosion, wear, abrasion, heat impact, etc. But, the higher residual stresses induced during welding or mismatch of thermal coefficients, micro-crack propagation, and formation of precipitates are problems which lead to premature failure of components (Okano et al., 2016; Yu et al., 2017). Therefore, choosing a proper welding method to coat is also very important to avoid distortion of the welding structure and the unacceptable microstructure in dissimilar welding, which will lead to corrosion of components (Dong et al., 2018; Kartsonakis et al., 2016; Moteshakker and Danaee, 2016; Shao et al., 2017; Sumitra et al., 2019; Wang et al., 2011; Xu et al., 2016).

In this chapter, the corrosion behaviour of the IS2062 Grade B substrate with Inconel-625 coating is reported. SS-309Mo is chosen as the intermediate layer with the help of Schaeffler Diagrams because of its higher chromium and nickel contents, ability to tolerate dilution. The use of SS-309Mo as an intermediate layer will thus prevent the martensitic structure formation due to dilution by low carbon steel and cracking. The Inconel-625 is chosen as the top coating layer because of its excellent corrosion resistance to seawater. The linear polarization resistance (LPR) and electrochemical impedance spectroscopy (EIS) techniques are used to evaluate the corrosion properties of the substrate, intermediate layer, and the top layer. The stability of the weld overlay depositions is investigated using immersion tests.

3.2. Brief Methodology

Prior to the corrosion test, the samples were prepared according to ASTM Standard E3-11 (Mohammadi Zahrani and Alfantazi, 2012). The sample on which corrosion studies have to be carried out was cleaned with water and acetone after polishing the surface with grit 80 to 2000 SiC emery papers and 0.3 microns and 0.1 micron alumina suspension. The three-electrode system electrochemical test method which is similar to ASTM Standard G61 (Sturgeon, 2003) was used to record the corrosion behaviour of CS, SSCS, and ISSCS coupons. The test sample under consideration for the corrosion study acts as a Working Electrode (WE). Only the top surface of the weld overlay deposition (WE) was exposed to the electrolyte. The 3.5 wt.% NaCl solution prepared according to ASTM standard G5 (Balan et al., 2018). The WE was immersed in the electrolyte, which acts as the corrosion medium ($\text{pH} = 7.7$ at room temperature of 22°C).

Linear polarization resistance (LPR) and Electrochemical Impedance Spectroscopy (EIS) are used to evaluate anticorrosion properties. LPR measurements were carried out with a potential ramp of 50 mV around equilibrium potential, at a scan rate of 0.166mVs^{-1} . The electrochemical corrosion parameters were obtained using the linear polarization curve. The polarization resistances were calculated using the current density and the Tafel slopes. The corrosion rates (CRs) were expressed in mmpy, which was determined by the Tafel extrapolation method. The EIS of the samples was carried out in 3.5 wt.% NaCl solution in an applied frequency range of 100 mHz to 200 kHz at an AC signal of 10 mV amplitude.

3.3. Results and discussion

3.3.1 ANSYS FEA analysis for selection of the best model for WO coating based on low residual stress.

The present study is carried out to identify the most suitable buffer and the top coating layer, using different welding techniques like Gas Tungsten Arc Welding (GTAW) and Shielded Metal Arc Welding (SMAW). Buffer is the coating layer between the base metal and the top coating layer. The aim is to limit surface tensile residual stress in the coating

to below industry stress threshold of around 30 MPa to prevent stress corrosion cracking, by using different combinations of coating materials and welding techniques. The ANSYS birth and death simulation technique have potential applications in predicting optimum combinations of coating materials and welding techniques required for achieving low coating residual stress (Zhao et al., 2019). SS-309Mo and Inconel-625 welding consumables are used for depositing welds on low carbon steel plates. To minimize the dilution of the first weld layer with base metal, it is often necessary to deposit multiple weld layers using different welding techniques on low carbon steel. Dilution is the contamination of corrosion-resistant weld metal by non-corrosion resistant base metal.

3.3.1.1 Simulation

Finite element analysis of the coating process using welding parameters mentioned is carried out on twelve different models, as described in **Table 3.1**, based on ANSYS birth and death analysis to calculate the welding residual stress in both base material and coatings. The results of the residual stress analysis, with maximum values of residual stress in BM and coating layers (SS and INC) are shown in **Fig. 3.1** to **Fig. 3.4**. Different colors and contours in the figures indicate different values of residual stresses. The residual stresses are attributed to the mismatch of thermal expansion coefficients between the coating and BM.

The ANSYS welding simulation was considered as a sequential coupled field thermo-structural analysis and the element birth and death technique were employed for the simulation of weld coating. Since the substrate, and coatings SS-309Mo, Inconel-625 are ductile materials, the von Mises yield criterion is applied. The von Mises stress is used to predict the yielding of ductile materials under any loading condition. The yielding of materials begins when the second deviatoric stress invariant J_2 reaches a critical value.

Table 3.1. Twelve different combinations of Coating Materials and Welding Process

Model	Process	Residual Stress (MPa)		
		BM* (CS)	Coating Layer 1	Coating Layer 2
Model-1	GTAW*	129	63.2 (SS)	
Model-2	SMAW*	187	191.4 (SS)	
Model-3	GTAW	122	45.0 (INC)	
Model-4	SMAW	169	62.2 (INC)	
Model-5	GTAW	146	51.7(SS)	
	GTAW			20.3 (SS)
Model-6	SMAW	190	67.2 (SS)	
	SMAW			26.4 (SS)
Model-7	GTAW	134	46.6 (INC)	
	GTAW			17.5 (INC)
Model-8	SMAW	164	57.0 (INC)	
	SMAW			21.4 (INC)
Model-9	GTAW	139	48.5 (SS)	
	GTAW			18.3 (INC)
Model-10	SMAW	162	56.4 (SS)	
	SMAW			21.3 (INC)
Model-11	GTAW	153	54.1 (SS)	
	SMAW			21.2 (SS)
Model-12A (Without preheat, BM thickness- 6 mm)	GTAW	145	50.5 (SS)	
	SMAW			19.0 (INC)
Model-12B (With 100°C preheat, BM thickness-6 mm)	GTAW	137	47.8 (SS)	
	SMAW			18.0 (INC)
Model-12C (BM thickness- 7 mm)	GTAW	174	60.4 (SS)	
	SMAW			22.6 (INC)
Model-12D (BM thickness- 8 mm)	GTAW	192	25.3 (SS)	
	SMAW			25.3 (INC)

The von-Mises residual stress distribution was obtained for twelve different combinations of weld coating and welding techniques as shown in **Table 3.1**. In this simulation, the use of alternate skip welding technique and BM preheating to a temperature of 100 °C resulted in low coating residual stress in the final coating layer, much lower than the yield stress of the corresponding material. This ANSYS simulation technique has potential applications in predicting optimum combinations of coating materials and welding techniques for components requiring minimal residual stress.

FEM Model-1 to 4 (without BM preheat)

FEM Analysis using ANSYS Birth and Death technique was carried out on the Models-1 to 4 given below and the residual stress contours obtained are shown in **Fig. 3.1**. Model-1 is of single-layer coating of SS by GTAW process on BM. Model-2 represents the Single-layer coating of SS by SMAW process on BM. Model-3 represents the single-layer coating of INC by GTAW process on BM. Model-4 represents the single-layer coating of INC by SMAW process on BM. The residual stress in the middle section of the coating in **Fig. 3.1** is higher compared to corners, because of resistance to contraction of the middle section by surrounding coating material. The residual stresses obtained in Models-1 to 4 are given in **Table 3.1**. Since GTAW process is a low heat input process compared to SMAW, adopting GTAW process results in lower coating dilution with the base material. Also, the lower heat input of GTAW process results in lower differential expansions and consequently lower residual stresses, as shown in **Table 3.1** compared to SMAW process.

The stresses are lower in Models-3, 4 compared to Models-1, 2 because of the coefficient of linear expansion of INC coating material (given in chapter 2). This results in lower differential expansions and lower residual stresses. But the coefficient of linear expansion of the SS (given in chapter 2) used in Models-1, 2 is more than BM, resulting in higher differential expansions and higher residual stresses.

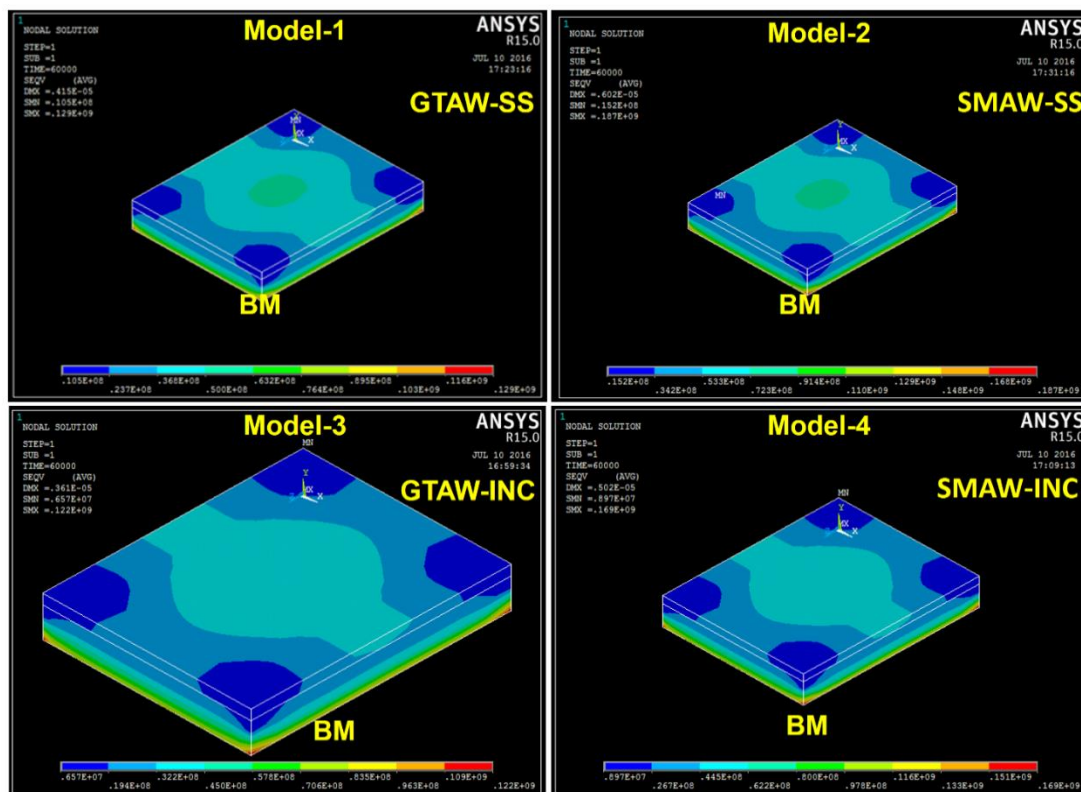


Fig. 3.1 Single layer residual stress comparison with process and coating variation.

FEM Model-5 to 8 (without BM preheat)

FE Analysis using ANSYS Birth and Death technique was carried out on the Models-5 to 8 given below and the residual stress contours obtained are shown in **Fig. 3.2**. Model-5 is a multilayer coating of SS by GTAW process on BM. Model-6 is a multilayer coating of SS by SMAW process on BM. Model-7 is a multilayer coating of INC by GTAW process on BM and Model-8 is a multilayer coating of INC by SMAW process.

The residual stresses obtained in Models-5 to 8 are given in **Table 3.1**. The coating residual stress values in the multilayer process of Models-5 to 8 are lower compared to the single-layer process followed in Models-1 to 4 (**Table 3.1**), due to interlayer stress relieving and also reduction in the thermal mismatch between coating layers 1 and 2. This results in lower differential expansions and lower residual stresses. But, the coefficient of linear expansion of SS coating material used in Models-5, 6 is more than BM, resulting in higher differential expansions and higher residual stresses. Though residual stress

obtained for Model 7 is minimum, the cost of INC is much more than the SS. Therefore, Model-7 cannot be taken as the best model.

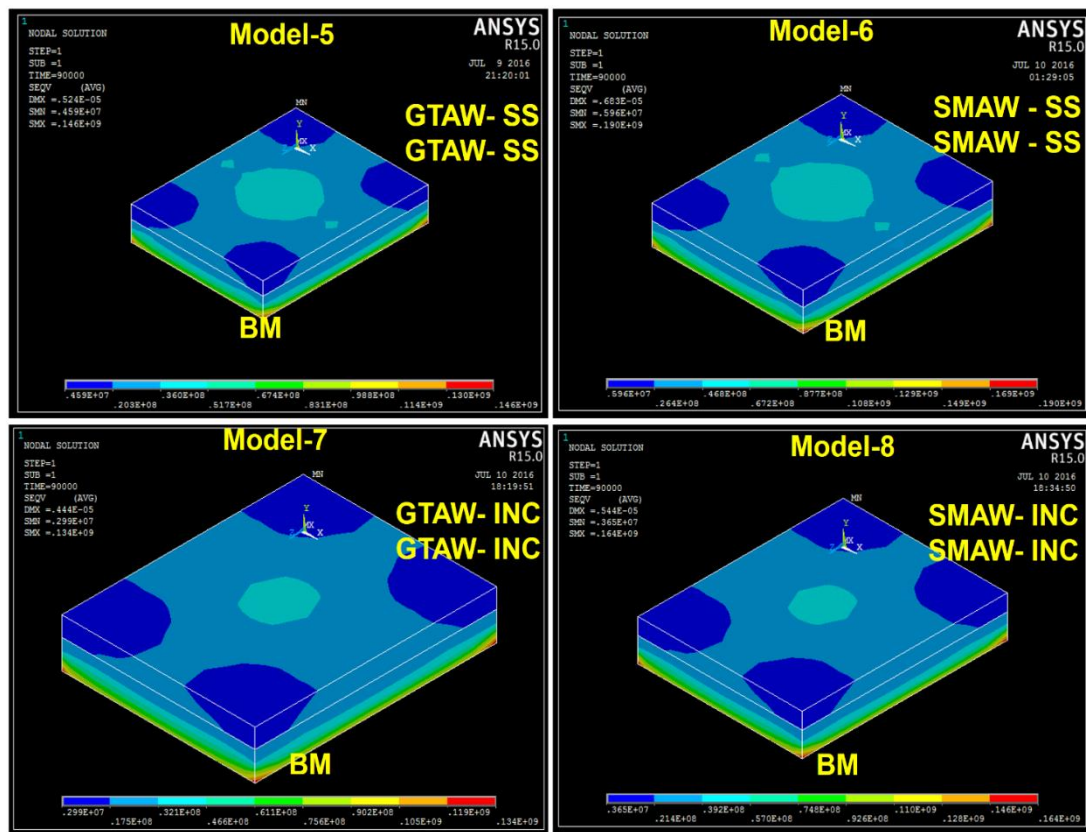


Fig. 3.2 Multilayer residual stress comparison with a single process and a single material.

FEM Model-9 to 12/12A (without BM preheat)

Fig. 3.3 shows the residual stress contours obtained from ANSYS birth and death technique results of the Models-9-12. Model-11 represents multilayer coating of SS first layer by GTAW and SS in the second layer by SMAW process on 6 mm thick BM, having more residual stress than the model 9, 10, and 12. The residual stresses obtained are given in **Table 3.1**. The residual stress values in the top layer of coating in Models-9, 10 which uses different materials for different layers, are much lower compared to Models-5 to 8 (**Table 3.1**), where a single material was used for both coating layers. Therefore, the use of SS as a buffer layer, results in obtaining lower residual stresses in INC top layer due to the interlayer stress relieving. Also, the buffer layer prevents dilution of the top layer with the BM.

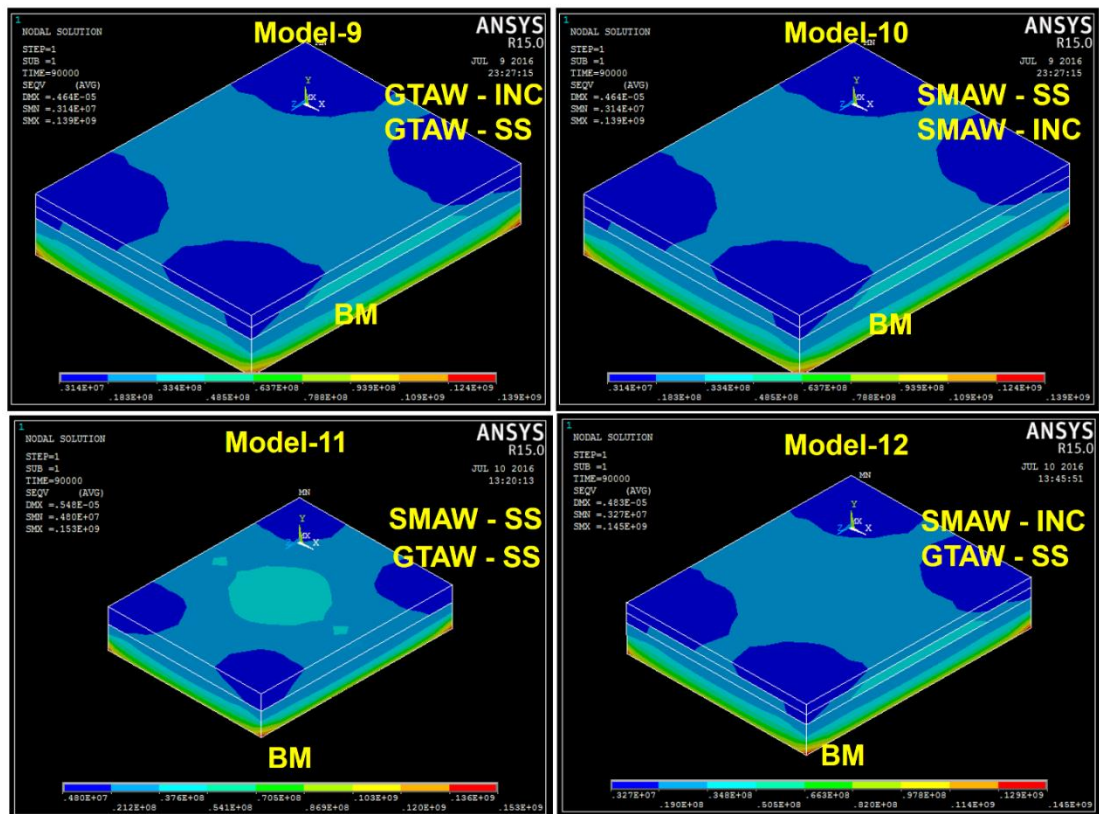


Fig. 3.3 Multilayer residual stress comparison with process and coating material variation.

FEM Model-12A and 12B (Effect of BM preheat)

Fig. 3.4 shows the models 12A and 12B of FEM with and without BM preheated to 100°C respectively. A comparison of residual stresses obtained in Models-12A and 12B is shown in Table 3. Preheating of BM to 100°C, as carried out in Model-12B results in lower cooling rates of weld overlay materials and therefore lower residual stresses in coatings, compared with Model-12A in which BM is not preheated.

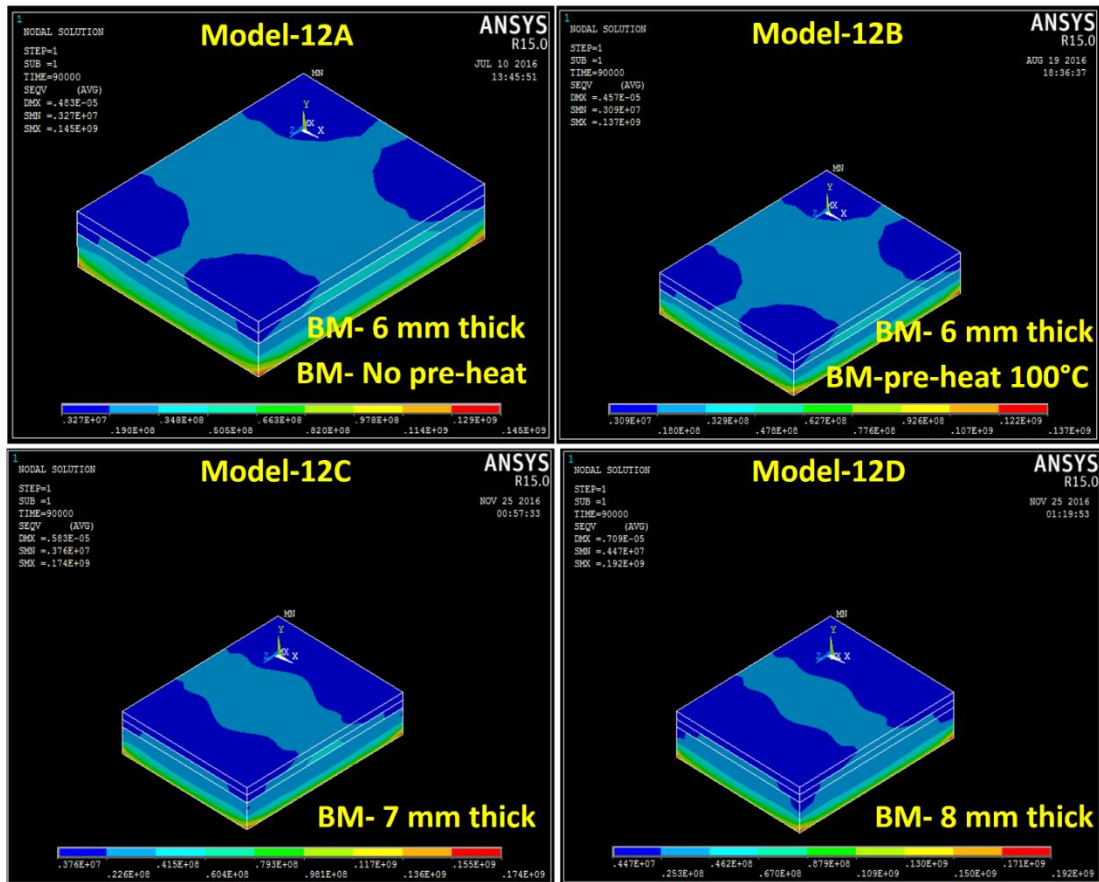


Fig. 3.4 Multilayer residual stress comparisons with BM preheat and without preheat variation and BM thickness variation.

FEM Model-12A, 12C and 12D (Effect of BM thickness)

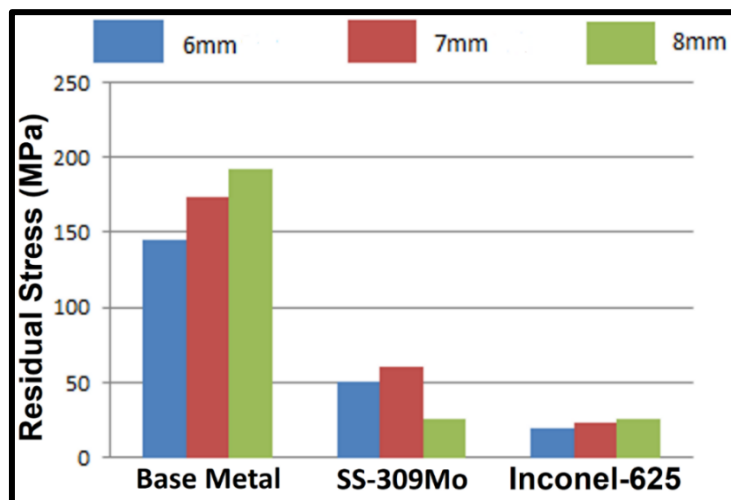


Fig. 3.5 Residual Stress for multilayer coating with variation in BM thickness

The residual stress contours obtained using ANSYS Birth and Death technique for the model- 12A, 12C and 12D are depicted in **Fig. 3.4**. The thicknesses of the BM are 6 mm, 7 mm and 8 mm for Model 12A, 12C and 12D respectively. The corresponding residual stress values obtained are tabulated in **Table 3.1**. When the BM thickness was changed from 6 mm to 8 mm, the residual stress in the final coating layer of INC changed from 19.0 MPa to 25.3 MPa which can be witnessed from **Fig. 3.5**. The slight increase in coating residual stress is due to higher restraint on the coatings, due to an increase in base material thickness. The base material residual stress has also increased due to the higher restraint. The reduced surface residual stress of Inconel-625 final layer coating obtained is below 30MPa, which is the industry threshold, which will also help in preventing severe corrosion-related problems like stress corrosion cracking and corrosion fatigue.

In conclusion, Based on the ANSYS birth and death residual stress analysis conducted on twelve different combinations of coatings and welding techniques, the following conclusions can be drawn.

- a) All the residual stresses in the twelve models are found to be much below the yield strength of the respective materials. The coating residual stress values in the multilayer process are much lower compared to the single-layer process, which is due to the interlayer stress relieving and also reduction in the thermal mismatch between coating layers 1 and 2.
- b) The residual stresses in the base material and coatings increase with an increase in the base material thickness is due to higher restraint.
- c) A multilayer coating simulation of alternate skip welding of SS-309Mo weld overlay as a first layer by GTAW and Inconel-625 weld overlay as second final layer by SMAW process for the 6 mm thick base metal preheated to 100°C, was the best model among twelve combinations with 18 MPa surface residual stress.
- d) The very low values of surface residual stress obtained in the final layer of Inconel-625 coating are below 30MPa, which is the industry threshold.

3.3.2 Weld Overlay Coating of Model 12B.

3.3.2.1 Structural Analysis

The weld overlay deposited samples were subjected to the powder X-ray diffraction (XRD) for structural analysis.

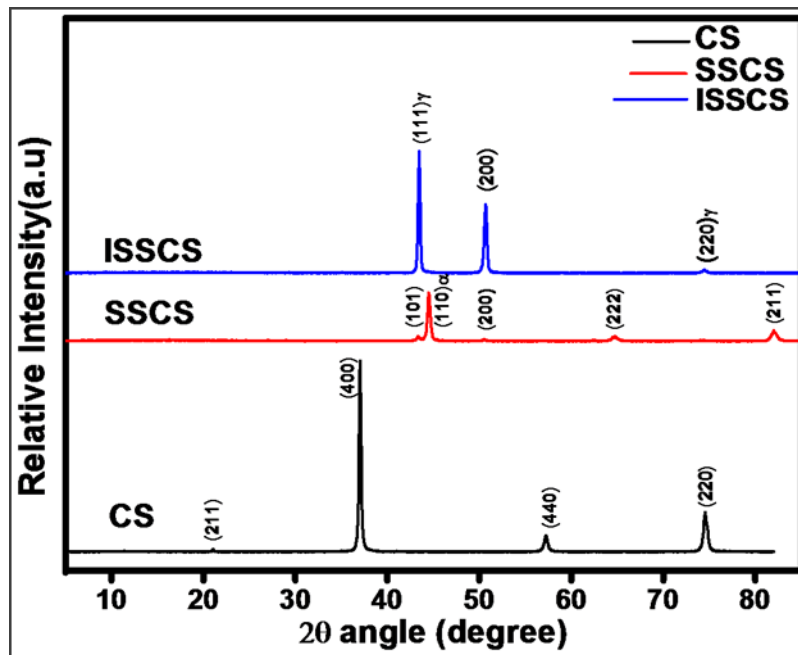


Fig. 3.6 XRD plot of the substrate (CS SSCS and ISSCS.),

Fig. 3.6 shows the XRD patterns of CS, SSCS, and ISSCS. The peaks in the XRD spectrum of the substrate (CS) match with the JCPDS file number 39-0238. The major peaks of CS are at 21.1°, 37°, 57.2° and 74.5° angles and correspond to (211), (400), (440) and (220) planes. The XRD pattern of SSCS has peak positions at 43.3°, 44.5°, 50.6°, 64.7° and 82° angles. It was noticed that SSCS has a dominating austenitic face-centered cubic (FCC) structure. The XRD pattern of the weld overlay deposited Inconel-625 (ISSCS) top layer shows major peaks at the angles 43.5°, 50.7° and 74.5°, which correspond to (111), (200) and (220) planes, respectively. However, the major peak positions of pure Inconel-625 are found to be at angles 44.5°, 51.9° and 76.4° according to the JCPDS file number (01-074-208). This slight shift in the peak position is attributed to the alloying elements in the Inconel 625, which form the solid solution (Abioye et al., 2015). The phase close to the γ -Nickel FCC structure is found on the top surface of

ISSCS indicating that, there is no dilution or any foreign material in the weld overlay deposition.

3.3.2.2 Surface morphology

The surface morphology of the weld overlay depositions was examined with the help of SEM. **Fig. 3.7** (a) shows the microstructure of the weld overlay deposited sample which depicts the substrate (CS), SSCS intermediate layer and the ISSCS top layer. **Fig. 3.7** (b) shows the surface morphology of SSCS, indicating the austenitic structure of the steel.

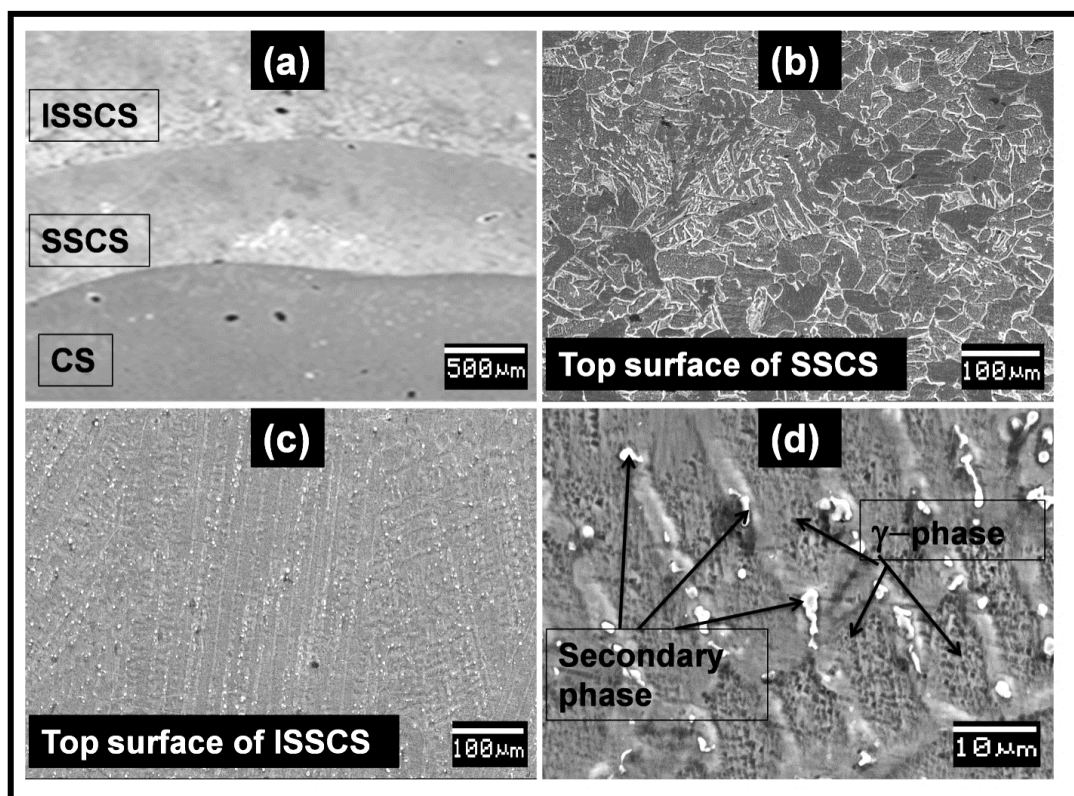


Fig. 3.7 SEM of (a)CS, SSCS and ISSCS at the cross-section, (b)top surface of SSCS (c) and (d) the top surface of ISSCS at lower and higher magnifications respectively.

Fig. 3.7 (c) and (d) show the microstructure of the top surface of the Inconel-625 (ISSCS) at lower and higher magnifications, respectively. The surface depicts the typical Inconel 625 welded microstructure. Further, the dendritic columnar structure can be seen in the micrographs, which shows the γ -Nickel phase and the secondary phases (**Fig. 3.7** (d)) similar to observations reported elsewhere (Abioye et al., 2015; Xing et al., 2014). From

these images, it can be seen that there are no defects like cracks or pores, which are major problems in the weld overlay deposition. This may be attributed to the lower residual stresses in the coating material, which is due to the reduction in the thermal mismatch between the coating and the substrate. More care is taken to obtain a good top layer because; the surface morphology plays an important role in the electrochemical corrosion mechanism.

3.3.3 Electrochemical Corrosion Behavior

3.3.3.1 Linear polarization resistance (LPR) measurements

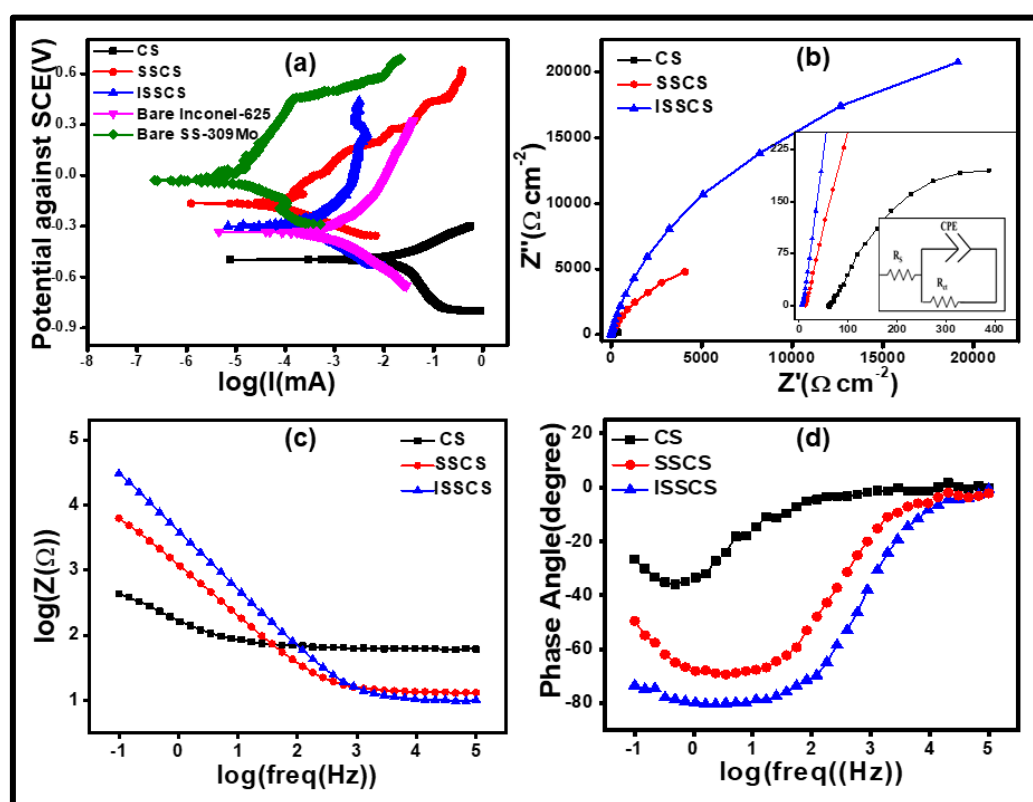


Fig. 3.8 (a) Tafel plot of CS, SSCS and ISSCS, bare SS-309Mo and Bare Inconel-625, (b) Nyquist Impedance Plot (with insets of enlarged Nyquist plot CS and equivalent circuit used for fitting), c) Bode plot and d) Bode impedance plot of CS, SSCS and ISSCS.

Fig. 3.8 (a) shows the Tafel plots of CS, SSCS, and ISSCS. The corrosion potential (E_{corr}) and corrosion current density (I_{corr}) were obtained from the intersection point of anodic (β_a) and cathodic (β_c) branch of Tafel slopes. Polarization resistance (R_p) is calculated

using Stern Geary eq.(2.3) whereas, the corrosion rate (CR) is calculated according to G102 ASTM standard using the eq.(2.4) (Singh et al., 2016) (Yang et al., 2017).

Table 3.2 Corrosion parameters obtained for substrate and weld coated samples from LPR test

Sample	E_{corr} (mV)	I_{corr} (μAcm^{-2})	β_a (mV)	β_c (mV)	CR (μmpy)	R_p ($\text{k}\Omega$)
CS	-477.89	21.091	409.0	128.6	169.68	2.02
SS-309Mo(bare)	-254.978	0.77	293.0	155.0	8.82	56.99
SSCS	-436.51	1.860	176.1	281.0	10.63	25.26
Inconel-625(bare)	-166.818	0.282	452.8	193	1.12	208.59
ISSCS	-306.27	0.293	273.8	171.9	1.16	156.50

As it is evident from the **Table 3.2**, the I_{corr} values of CS, bare SS309Mo, SSCS, bare Inconel 625 and the ISSCS are 21.09, 0.77, 1.86, 0.28 and $0.29\mu\text{Acm}^{-2}$ respectively. The decrease in corrosion current density is an indication of reduction in the corrosion rate (Sadeghimeresht et al., 2018; Wang et al., 2011). The R_p values are 2.02, 56.9, 25.26, 208.59 and 156.50 whereas the corrosion rates are 169.68×10^{-3} , 8.82×10^{-3} , 10.63×10^{-3} , 1.12×10^{-3} and 1.16×10^{-3} mmpy for the CS, bare SS-309Mo, SSCS, bare Inconel-625 and the ISSCS layer respectively. The R_p values for the weld overlay coatings have increased while the CR has decreased drastically. The CR , I_{corr} and RP values of SSCS and the bare SS-309Mo indicate that the corrosion properties have changed from its bulk form to that of weld overlay deposited samples. The reason for these changes is due to the distortions, effect of heat during weld overlay, etc. However, in the case of bulk Inconel-625 and the ISSCS samples, the CR , I_{corr} , and R_p values are nearly the same. The high molybdenum and chromium content in the Inconel-625 makes it very much resistant to corrosion. The niobium stabilizes the alloy against sensitization during weld overlay, thereby preventing subsequent inter-granular cracking. The introduction of the intermediate layer of SS-309Mo reduces the thermal stress between the substrate and the anticorrosive layer, thereby helping to retain the bulk anticorrosive properties of the Inconel-625. LPR studies

of the coatings show that the Inconel-625 is a good anticorrosive coating with an SS-309Mo intermediate layer.

3.3.3.2 Electrochemical Impedance Spectroscopy (EIS)

The Nyquist plots of CS, SSCS, and ISSCS are shown in **Fig. 3.8** (b) and inset is the enlarged Nyquist plot of CS. Nyquist plots of all samples show incomplete semicircular arcs. The radius of the semicircular arcs of coatings and bare material is in the order of $CS < SSCS < ISSCS$, which indicates the largest resistance of ISSCS in the electrolyte.

The EIS spectra of the samples are fitted to an equivalent circuit as in eq. 3.1 using EC-lab software with minimum values of $\chi^2 \sim 10^{-3}$ to explain the electrochemical behaviour of weld overlay depositions. The fitted equivalent circuit for CS and SSCS is shown in the inset of **Fig. 3.8** (b). The impedance (Z) of the weld overlay and substrate governs the electrochemical reactions at the working electrode and the electrolyte interface is given by

$$Z(\omega) = R_s + \frac{1}{\frac{1}{R_{ct}} + i\omega C} \quad (3.1)$$

where ω is the angular frequency (rad/s) equal to $2\pi f$ and f is the frequency (Hz). R_{ct} is the charge transfer resistance and R_s represents the solution resistance. C is the capacitance (F). Constant Phase Element (CPE) in CS and SSCS which represents the passive film capacitance (C) or double-layer capacitance. The presence of CPE indicates the inhomogeneity and surface roughness in CS and SSCS but the ISSCS samples have pseudo-capacitance (C) and in the circuit diagram the CPE is replaced by C for ISSCS sample (Jinlong et al., 2015; Jüttner, 1990; K et al., 2016; Li et al., 2005; Mansfeld, 1990; Mayavan et al., 2013; Wang and Alfantazi, 2014).

The solution resistance R_s is due to the metal ions formed at the interface by electrochemical reactions. The corrosion rate was controlled by the electrochemical reactions and the migration of ions (Meng et al., 2016). The significance of R_{ct} signals indicates interfacial charge transfer, which is the controlling step of the corrosion reaction (Hong et al., 2002). As per **Table 3.3**, the R_{ct} values of coating are very high i.e, for R_{ct} of ISSCS is 281.251 k Ω and for R_{ct} of SSCS is 32.72 k Ω when compared to the substrate

(CS). Since R_{ct} is the measure of electron transfer across the surface, therefore, it is inversely proportional to the corrosion rate indicating that ISSCS has the least corrosion rate (Yan et al., 2017). Thus, the EIS response of ISSCS, characterized by high charge transfer resistance R_{ct} , indicates it is electrochemically more stable. A coating with a larger capacitive loop is the indication of good corrosion resistance (Al Zoubi and Ko, 2018; Kumari et al., 2018). Since it is a bi-layer weld overlay deposition, the cracks or pores on the top layer will not reach the CS due to the presence of the intermediate layer SS-309Mo between the substrate and the top layer (Rashmi et al., 2017; RIBEIRO et al., 2015; Wang et al., 2016).

Table 3.3 Equivalent circuit fitting parameters

Circuit parameters	$R_s(\Omega)$	CPE/C(μF)	α	$R_{ct}(k\Omega)$
CS	62.78	2.339	0.63	0.81
SSCS	17.55	31.91	0.70	32.72
ISSCS	6.36	40.82	0.89	281.25

Fig. 3.8 (c) and (d) show the Bode impedance and Bode phase angle plot respectively, for the CS, SSCS, and ISSCS weld overlay depositions. **Fig. 3.8** (c) shows that the impedance has increased on the deposition of Inconel-625 which was also supported by the Nyquist plot. The Bode plot for the weld overlay depositions shows a capacitive behaviour, which is typical for the passive materials. The phase angle of about -83° , suggests that more stable film is formed on the weld overlay depositions in the electrolyte used and an onetime constant is observed.

Owing to the complex alloying elements in SSCS and ISSCS, many metal dissolution reactions can contribute to the corrosion rates in the anodic branch. Therefore, at the anode, the metal dissolution can be written as ($M_{aq}^{n+} + ne^- \leftrightarrow M_s$) and at the cathode, the reaction is due to the oxygen reduction ($O_{2(g)} + 2H_2O_{(aq)} + 4e^- \leftrightarrow 4OH_{(aq)}^-$) as the electrolyte solution is neutral (Gateman et al., 2018).

3.3.3.3 Stability by Immersion Test

Further, the stability of the SSCS and ISSCS weld overlay deposits were investigated by immersing in 3.5% NaCl solution for different periods (1hour, one day, seven days, and fourteen days). Only the top surface of the weld overlay deposition was exposed to the electrolyte and the rest of the sides was masked with Teflon tape to study the electrochemical behaviour of the depositions. The immersed samples were taken out and washed thoroughly with distilled water to remove the corrosion products and analysed using the LPR and EIS.

Fig. 3.9 (a) and (b) show the Tafel plots and **Fig. 3.9** (c) and (d) show Nyquist plots of SSCS and ISSCS samples respectively after immersion. From Tafel plots of SSCS, we can observe that there is a formation of the passive film in 7 days of immersion, whereas this film broke down on 14 days of immersion. This passive film layer is more stable in the ISSCS samples than SSCS samples and it provides good and stable anticorrosive properties to the ISSCS weld overlay. These results are also supported by the Nyquist plots. The impedance of ISSCS samples increases with an increase in the immersion time, while, the impedance of SSCS samples decreases on immersion for 14 days. This indicates the enhancement of the anticorrosive properties of CS on SS-309Mo and Inconel-625 weld overlay (Zhang et al., 2016).

The immersion studies confirmed the longer stability of weld overlay of SS-309Mo and Inconel-625 on CS. The inhomogeneous passive film formation in SSCS is mainly due to the high percentage of iron content in the SS-309Mo. The chloride ion incorporation in the stainless steel SS-309Mo attributes to the loose passive film ($Me + Cl^- = MeCl^{n-1}$) and therefore the breakdown of the passive film happens with time (Zhang et al., 2018). On the other hand, the higher Nickel content along with Mo, Cr, and Nb in the Inconel-625 helps the passive film to be stable, compact and uniform for a long duration (Qiu et al., 2017).

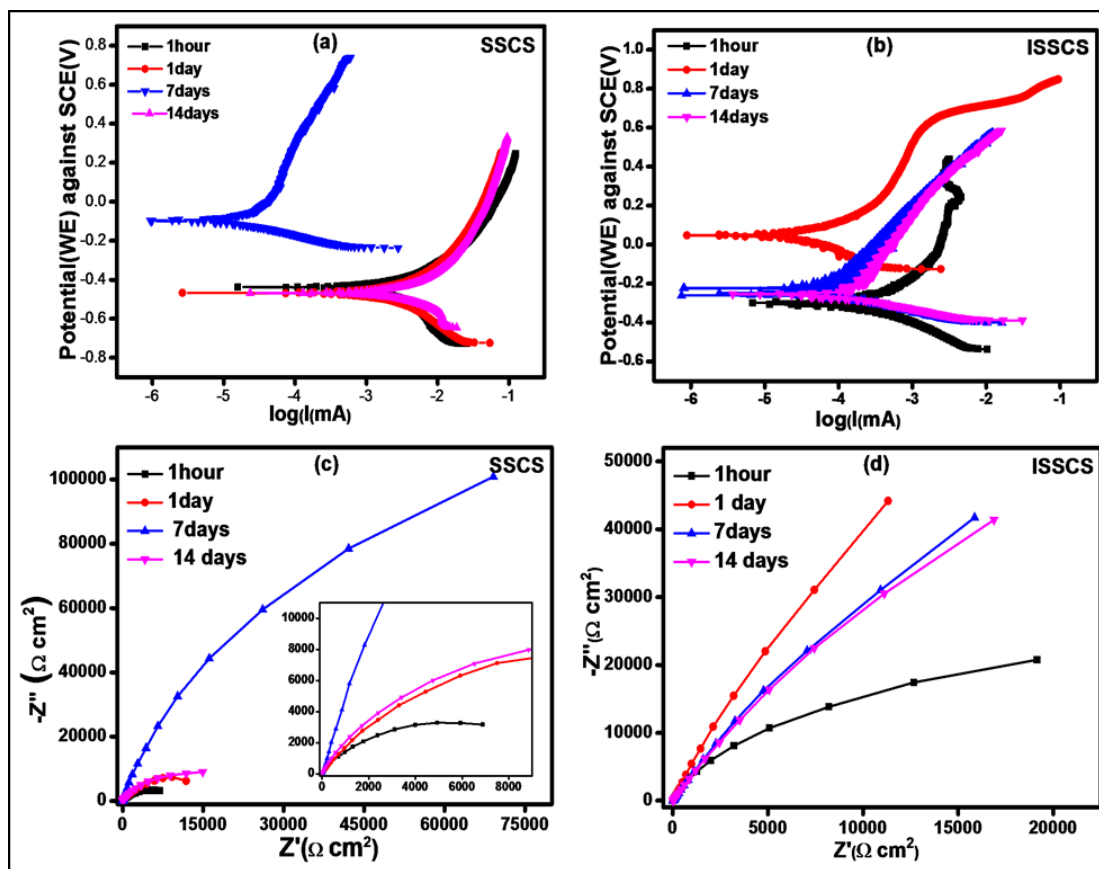


Fig. 3.9 (a) and (b) Tafel plots and (c) and (d) Nyquist plot of the SS-CS and ISS-CS respectively at different immersion periods namely 1 hour, 1 day, 7 days and 14 days.

In conclusion, the bi-layer weld overlay coating has been deposited on low carbon steel with SS-309Mo as the intermediate layer and Inconel-625 as the top layer. The intermediate layer SS-309Mo helps in preventing the dilution with the top layer. The top layer ISS-CS revealed higher corrosion resistance with a CR of 1.16×10^{-3} mmpy. Further, a decrease in I_{corr} and an increase in R_p confirm the good corrosion resistance of top layer weld overlay deposition. The CR, I_{corr} , and R_p values of ISS-CS are comparable with the bulk Inconel-625, which indicates that the weld overlay could achieve the intrinsic corrosion values as that of bulk Inconel-625 with just 2 mm layer thickness deposition. The immersion studies showed that the ISS-CS form a stable anticorrosive film on the substrate. Therefore, the Inconel-625 weld overlay with an intermediate layer of SS-309Mo can reduce the cost, distortions, and increase the corrosion resistance and durability of the carbon steel components used in the seawater.

3.3.4 Mechanical properties of the coatings.

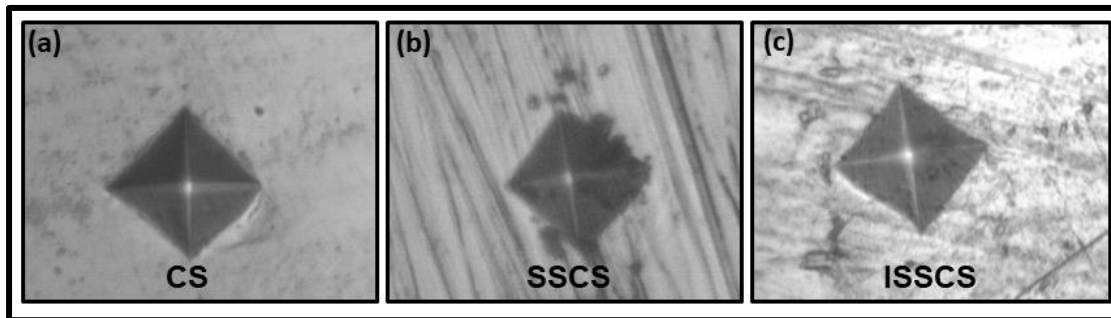


Fig. 3.10 Vicker's indentation on a) substrate (CS), b) SS-CS and c) ISS-CS

Fig. 3.10 (a) (b) and (c) show the microhardness indentation of CS, SS-CS and ISS-CS samples respectively which are obtained with 300 gf load for a dwell time of 10 seconds. The microhardness is obtained in H_v and is converted to GPa by a conversion factor and the values are tabulated in **Table 3.4**. The hardness of the CS sample is found to be 1.67 ± 0.13 GPa. Further, the microhardness of SS-309Mo is 1.96 ± 0.09 GPa whereas, for SS-CS, the microhardness has increased to 2.11 ± 0.10 GPa. Similarly, the microhardness has increased to WO coated Inconel-625 from 2.30 ± 0.07 GPa to 2.52 ± 0.11 GPa (ISS-CS). The increase in microhardness of the overlay presumably occurs due to the hardening of the metal due to quenching after the weld overlay. Since Inconel-625 alloy contains 3.5 wt% Nb, the formation of γ'' can occur if heated in the appropriate temperature range. The formation of substantial γ'' would result in an increase in overlay hardness. Also, the inter-dendritic and columnar microstructure in the weld overlay will lead to an increase in microhardness (Abioye et al., 2015; Xing et al., 2014).

Table 3.4 Hardness values for coated and uncoated samples in GPa

Sample	Microhardness (Gpa)
Base material (CS)	1.67 ± 0.13
SS-309Mo (SS)	1.96 ± 0.09
SSCS	2.11 ± 0.10
Inconel-625 (I)	2.30 ± 0.07
ISSCS	2.52 ± 0.11

3.4 Summary and Conclusions

The bi-layer weld overlay coating has been deposited on low carbon steel with SS30Mo as the intermediate layer and Inconel-625 as the top layer. This combination has been chosen with ANSYS FE analysis with minimal residual stress. A multilayer coating simulation of alternate skip welding of SS-309Mo weld overlay as a first layer by GTAW and Inconel-625 weld overlay as second final layer by SMAW process for the 6 mm thick substrate preheated to 100°C, was the best model among twelve combinations with 18 MPa surface residual stress. The intermediate layer SS-309Mo helps in preventing the dilution with the top layer. The top layer ISSCS revealed a higher corrosion resistance with a corrosion rate of 1.16×10^{-3} mmpy. Further, a decrease in I_{corr} and an increase in R_p confirm the good corrosion resistance of top layer weld overlay deposition. The CR, I_{corr} and R_p values of ISSCS are comparable with the bulk Inconel-625, which indicates that the weld overlay could achieve the intrinsic corrosion values as that of bulk Inconel-625 with just 2 mm layer thickness deposition. The immersion studies showed that the ISSCS form a stable anticorrosive film on the substrate. Also, the microhardness of the ISSCS was found to be 2.52 ± 0.11 GPa and that of bulk Inconel-625 was 2.30 ± 0.07 GPa which are nearly equal. Therefore, the Inconel-625 weld overlay with an intermediate layer of SS-309Mo can reduce the cost, distortions, increase corrosion resistance, hardness and durability of the carbon steel components used in the sea water.

CHAPTER 4

HVOF coating of Nickel Chromium-Chromium Carbide cermet: Corrosion, mechanical and wetting properties

Outcome of Chapter 4

1. “Mechanical and wetting properties of 25%NiCr-75%Cr₂C₃ cermet coated on low carbon steel using HVOF thermal spray technique” (**Physica B: condensed matter – Elsevier**)
2. Corrosion Behaviour and Characterization of Thermal Sprayed Coating of Nickel Chromium Cermet on Low Carbon Steel” January 2018, **Materials today: proceedings- Elsevier**
3. “Electrochemical corrosion behaviour of nickel chromium-chromium carbide coating by HVOF process” April 2018 **AIP Proceedings**

CHAPTER 4

HVOF coating of Nickel Chromium-Chromium Carbide cermet: Corrosion, mechanical and wetting properties

Overview

In this chapter, the results on corrosion, mechanical and wetting behaviour of 25(NiCr)-75Cr₃C₂ cermet coating on low carbon steel substrate by HVOF process are included. Different phases such as Cr₇C₃ and Cr₃C₂, along with Ni and chromium oxide (Cr₃O₂) constituents present in the coating were revealed by X-Ray Diffraction (XRD) analysis. The morphology of the coating obtained by a scanning electron microscope (SEM) confirmed the phases observed from the XRD analysis. LPR and EIS were used to study the corrosion behaviour of the cermet in 3.5wt% NaCl electrolyte solution. Also, the mechanical and wetting properties of the 25(NiCr)-75Cr₃C₂ coating are studied by micro-indentation and contact angle measurement respectively.

4.1 Introduction

Nickel chromium cermet coatings like 25(NiCr)-75Cr₃C₂ are widely used commercially because of its high-temperature erosion and corrosion resistance properties. Due to the high corrosion resistance of NiCr binder, Cr₃C₂- NiCr coatings can be used in the corrosive environment and the presence of carbide particles provides sufficient erosion and wear resistance. Many studies were reported on friction, wear, and erosion behavior of HVOF sprayed 25(NiCr)-75Cr₃C₂ coating (Kumar et al., 2013; Nguyen Van et al., 2019; Tailor et al., 2019). Coatings such as Chromium carbide with NiCr have been studied for wear resistance and heat resistance but, very little work has been done on seawater corrosion resistance of nickel chromium-chromium carbide cermet coating. Therefore an effort has been taken to study the corrosion behaviour, mechanical and wetting properties of thermal sprayed 25(NiCr)-75Cr₃C₂ coatings.

4.2 Brief methodology

The ceramic-metal composite 25(NiCr)-75Cr₃C₂ has been spray dried and coated using HVOF process. The coatings phase analysis, structural and morphological characterizations were done by XRD and SEM respectively. The LPR and EIS electrochemical techniques were used for evaluating corrosion behaviour. The reproducibility of the results was verified by repeating the experiments. Further, mechanical and wetting properties have been studied.

4.3 Results and discussion

4.3.1 Structural Analysis of the coating

The X-ray diffraction (XRD) pattern of substrate and 25(NiCr)-75Cr₃C₂ coated samples are shown in **Fig. 4.1** (a) and (b) respectively. XRD analysis was carried out to identify the different phases present in the substrate and the coatings. Different carbide phases such as Cr₇C₃ and Cr₃C₂ were detected along with Ni and chromium oxide (Cr₂O₃) phases, which are shown in **Fig. 4.1**(b). The Chromium oxides were formed by a reaction of chromium with oxygen that comes from the flame and also from the atmosphere, during the spraying process (Nguyen Van et al., 2019).

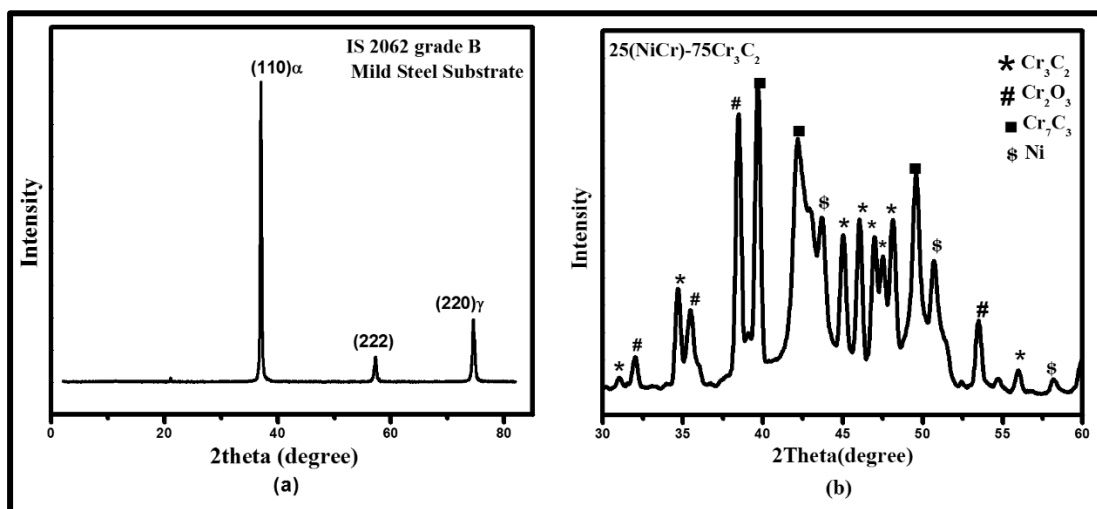


Fig. 4.1 XRD plot of (a) substrate (b) 25(NiCr)-75Cr₃C₂ coating on the substrate.

4.3.2 Morphological Analysis of the coatings

The SEM image of HVOF coated 25(NiCr)-75Cr₃C₂ cermet coating on the mild steel substrate is shown in **Fig. 4.2**. **Fig. 4.2** (a) and (b) show the microstructural evolution of HVOF sprayed 25(NiCr)-75Cr₃C₂ coating at lower and higher magnifications respectively. The coating is more uniform and dense which can be witnessed from the SEM images. The highly melted splats can be observed in the coatings. However, there are fewer pores, voids, very few un-melted particles (the brightest spots), few inclusions and oxides can be seen in the coatings which are generally characteristic features of thermal sprayed coatings (Tailor et al., 2019). Very dense and smooth coatings with no visible micro-cracks even at higher magnification prove that the good quality coating is achieved with the HVOF spraying technique due to its high-velocity impact on the substrate.

Cross-section images of the coatings are shown in **Fig. 4.2** (c) and (d). The backscattered micrograph of the cross-section (**Fig. 4.2(d)**) shows the different phases present in the coatings. The various shades of grey regions such as dark grey, light grey and darkest grey regions shown in the backscattered micrograph are attributed to Cr peaks indicating Cr₃C₂ phase; Ni peaks indicating Ni-Cr alloy phase, and two phase consisting of 25(NiCr)-75Cr₃C₂ composite phase respectively. The lightest regions are contaminants that might have occurred during the processing of the powder or during the coating process. Similar observations have been reported by (Shukla et al., 2015). The cross-section image shows a well-adhered coating on the substrate.

4.3.3 Electrochemical corrosion behaviour of the coatings

Electrochemical corrosion techniques such as Linear Polarization Resistance (LPR) and Electrochemical Impedance Spectroscopy (EIS) were used to study the corrosion behaviour of the substrate and substrate with cermet coating in 3.5wt% NaCl electrolyte solution.

4.3.3.1 LPR test

The Tafel plots of the 25(NiCr)-75Cr₃C₂ coatings and the substrate are shown in Fig. 4.3. The anodic and cathodic branches of the Tafel plot of the coated sample and the substrate are seen in the figure. The polarization resistance R_p for both the samples are calculated using the “Stern-Geary” equation 2.3. The values of I_{corr} and E_{corr} which were extracted from the Tafel slopes; R_p and corrosion rate (CR) are mentioned in Table 4.1 for both 25(NiCr)-75Cr₃C₂ coating and substrate samples.

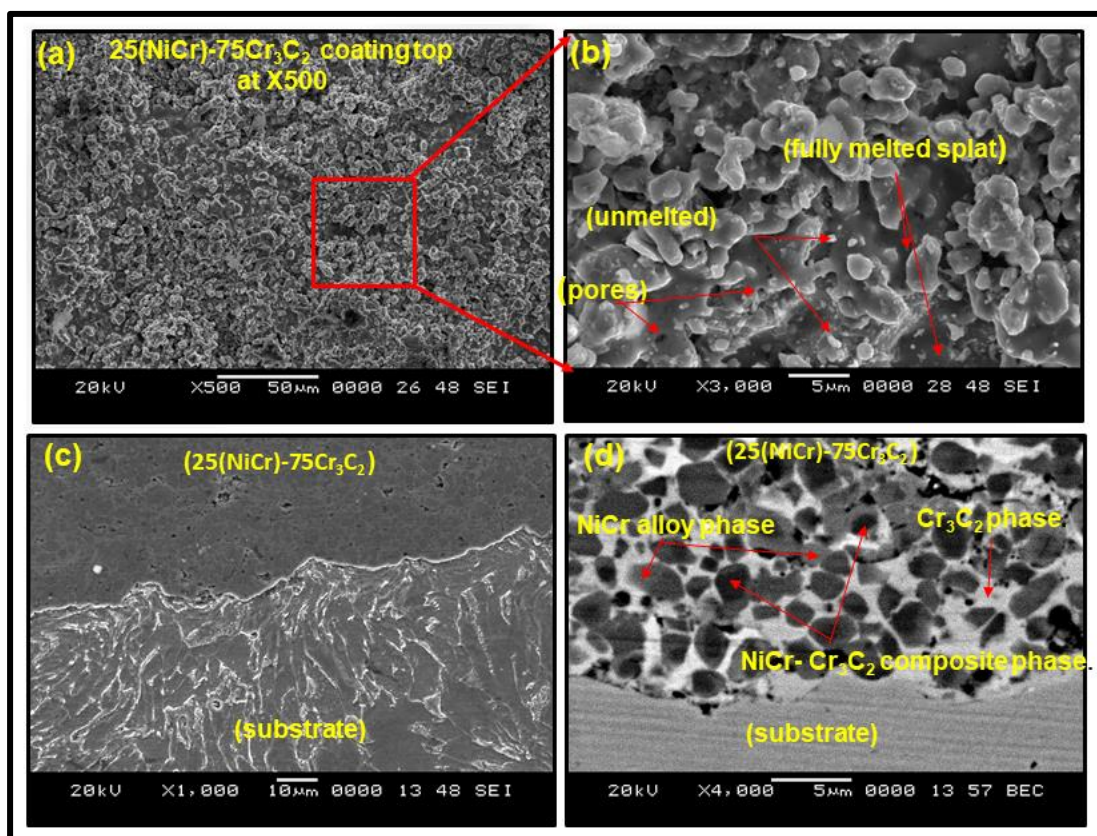


Fig. 4.2 SEM image of the 25(NiCr)-75Cr₃C₂ coated samples (a) as coated surface lower magnification (b) as coated surface higher magnification (c) Cross-section secondary electron image of the polished sample (d) Backscattered electron image showing different phases of the coatings in the cross-section view.

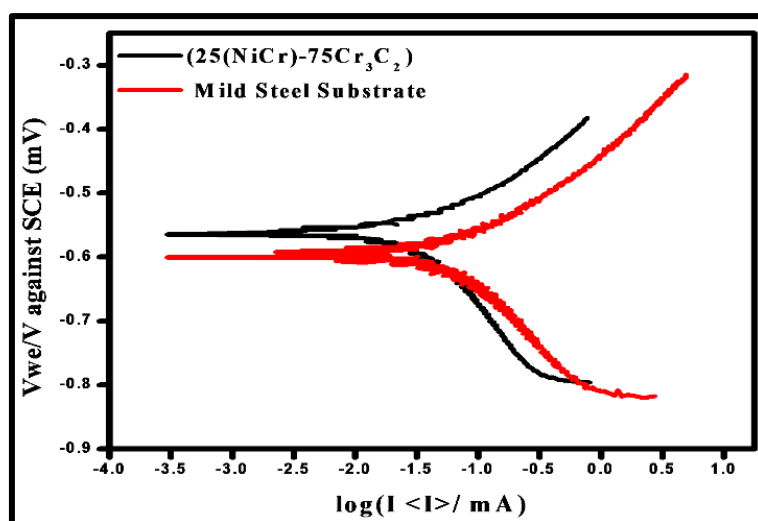


Fig. 4.3 Tafel plots of the 25(NiCr)-75Cr₃C₂ coating and the substrate.

Table 4.1 Corrosion parameters comprising of Coating and the substrate

Sample	E_{corr} (mV)	I_{corr} ($\mu\text{A}/\text{cm}^2$)	β_a (mV)	β_c (mV)	R_p (k Ω)	CR (mmpy)
Substrate	-477.89	21.09	409.00	128.60	2.01	0.50
Substrate with 25(NiCr)- 75Cr ₃ C ₂ coating	-488.25	06.89	263.00	157.00	6.21	0.10

The current density of the coated sample is found to be 6.878 ($\mu\text{A}/\text{cm}^2$) which is less than the substrate (21.091($\mu\text{A}/\text{cm}^2$)). The CR of the coated samples is five times less when compared to the substrate. The high current density and high anodic polarization of the substrate indicate the trans-passive stage and the formation of a passive layer on it. Whereas, the reduced corrosion current density of 25(NiCr)-75Cr₃C₂ coating indicates the higher corrosion resistance of the material.

4.3.3.2 EIS test

The EIS studies of the substrate and the 25(NiCr)-75Cr₃C₂ coated samples were performed in 3.5% NaCl solution in the frequency range of 10 kHz to 100 mHz, to investigate the electrochemical properties at the electrode/electrolyte interface. **Fig. 4.4** (a) shows the Nyquist plots of the substrate and the coated sample. The corrosion resistance of the material increased on coating. The Nyquist plots are fitted to their equivalent circuit using EC-lab software. The equivalent circuits for the substrate and

the coating are shown in **Fig. 4.4** (b) and (c) respectively. The elements of the equivalent circuits are tabulated in **Table 4.2**.

Table 4.2 Values of elements of Equivalent Circuit

Parameters	unit	Substrate	Substrate with 25(NiCr)-75Cr ₃ C ₂ coating
R_s	Ohm	10.78	1×10^3
$Q(\text{CPE})$	$\text{F} \cdot \text{sa}^{-1}$	0.01379	10×10^{-6}
R_{ct}	Ohm	234.7	100
C_{dl}	F	-	10×10^{-9}
α	-	0.67	0.8

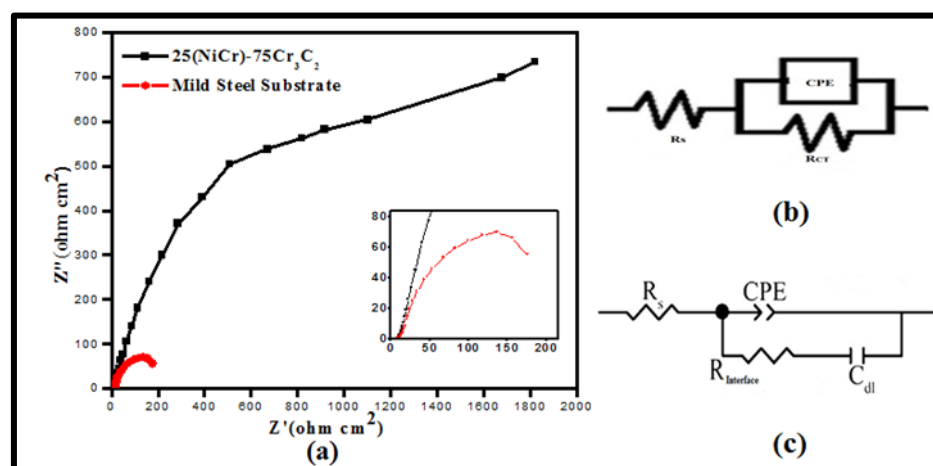


Fig. 4.4 (a) Nyquist Impedance plot of the substrate and the coating (b) Equivalent circuit of the substrate and (c) Equivalent circuit of the coating.

For the interpretation of the electrochemical behaviour of a system from EIS spectra, it is necessary to have an appropriate physical model of the electrochemical reactions occurring at the electrodes. Since the electrochemical cell presents impedance at a small sinusoidal excitation, it can be represented by an equivalent circuit (EC). The EC consists of various arrangements of resistances, capacitors and other circuit elements, and provides the most relevant corrosion parameters applicable to the substrate/electrolyte system. The representative data were analysed by fitting them in two most commonly used circuit models, with the results found more suitable for the system under study and the values of chi-square were less than 10^{-3} showing that the fitting is precise. Therefore, it could be concluded that the Nyquist plots were more

appropriate and it may have capacitive semicircles. The significance of R_{ct} signals indicates that there is an interfacial charge transfer, which is the controlling step for corrosion, has been effectively inhibited. An electrical double layer (C_{dl}) exists at the interface between an electrode and its surrounding electrolyte. This double layer is formed as ions from the solution ‘stick-on’ the electrode surface. Charges in the electrode are separated from the charges of these ions.

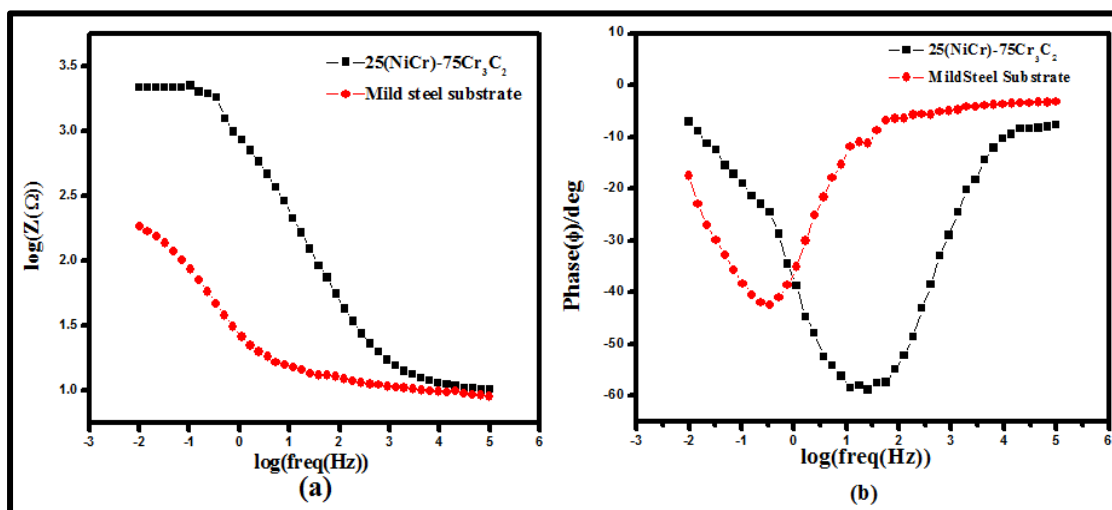


Fig. 4.5 (a) Impedance spectra (b) Bode plot for both 25(NiCr)-75Cr₃C₂ coating and the substrate.

Fig. 4.5 (a) and (b) shows the Impedance spectra and the Bode plots for the substrate with and without coating. Bode plot for the coating shows a typical passive material capacitive behaviour, indicated by medium to low frequency with phase angle approaching -60° , suggesting that a stable film is formed on the tested material in the electrolyte used. From **Fig. 4.5**(a), we can observe that the impedance of the material has increased on coating with 25(NiCr)-75Cr₃C₂ Cermet, which was also supported by Nyquist plot.

The impedance spectra obtained through the Nyquist and Bode plots showed the frequency response of the coating to the electrolyte. It also gave an insight into the interfacial reaction between the coating surface and the electrolyte. The impedance of the coating has increased when compared to the substrate.

The obtained result demonstrates that low-cost HVOF technique can be used to deposit superior quality Nickel and Chromium based coatings on components used in corrosive industrial applications, such as the marine environment.

4.3.4 Mechanical properties of the coatings

The microhardness of the HVOF thermal sprayed 25(NiCr)-75Cr₃C₂ coating and the substrate were measured using the Clemex Microhardness Tester-CMT having computer-controlled motorized turret provided by Clemex Technologies. The microhardness was measured by applying a load of 300 gf for a dwell time of 10 s using Vickers indenter. 10 different indentations at different locations on the coatings were taken to measure the microhardness and the mean value is reported. The cracks on the coatings are generated on the application of 1 kgf. The half crack length is measured. The microhardness and fracture toughness are calculated using equation.2.5 and equation.2.6 respectively.

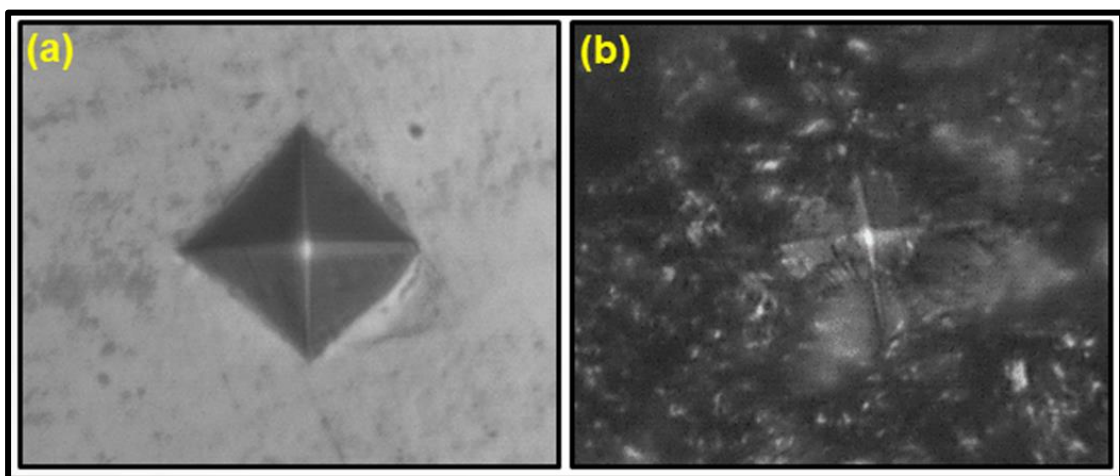


Fig. 4.6 Vicker's micro-indentation on a) Substrate low carbon steel IS2062 grade and b) thermal sprayed 25(NiCr)-75Cr₃C₂ coating.

Table 4.3 The mechanical properties of the substrate and the 25(NiCr)-75Cr₃C₂ coating.

Sample	Microhardness [GPa]	Fracture Toughness [MPa m ^{1/2}]
Substrate	1.56±0.078	1.6 ± 0.9
25(NiCr)-75Cr ₃ C ₂ coating	12.69±0.362	4 ± 1

Fig. 4.6 (a) and (b) shows the Vicker's micro-indentation of the substrate and 25(NiCr)-75Cr₃C₂ coating respectively. The diamond pyramidal-shaped indentations on the substrate and the coating were obtained. Microhardness of the substrate was found to be 159±8 H_v and that of the 25(NiCr)-75Cr₃C₂ coating was found to be 1294±37 H_v. This shows that the hardness value solely depends on the microstructure of the thermal sprayed coatings. The fracture toughness of the low carbon steel and the coating also calculated and are tabulated in **Table 4.3**. Thus, the coating demonstrated good mechanical behaviour with high microhardness and high fracture toughness.

4.3.5 Wetting properties of the coatings

The 3.5wt.%NaCl salt solution contact angle (CA) with the thermal sprayed 25(NiCr)-75Cr₃C₂ coating and the substrate were measured. For the present work about 10 µl of 3.5wt.%NaCl salt solution was dispensed on the substrate and 25(NiCr)-75Cr₃C₂ coatings. The droplet was made to rest for about 60 s to record the contact angle. Holmarc's CA analysis software is used for the analysis of the captured image. The CA was measured using Young's equation.2.8. The Contact Angle Hysteresis (CAH) is measured taking the difference between the preceding and advancing angles.

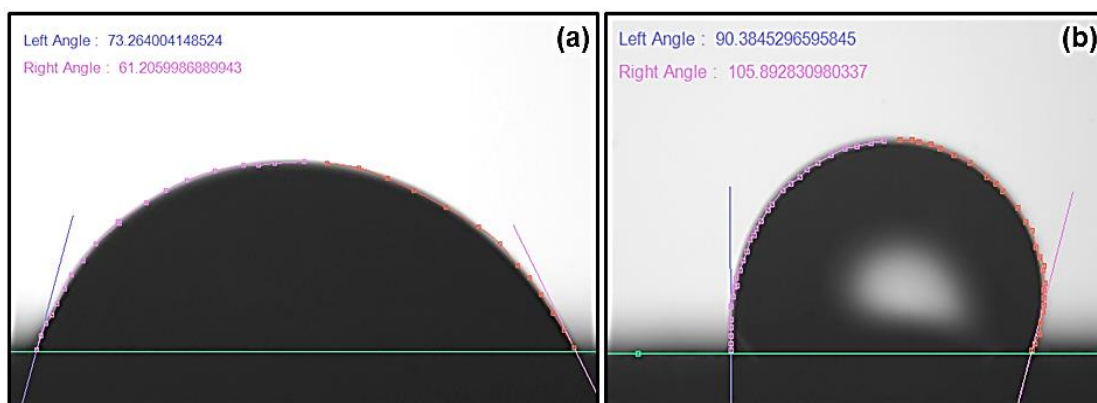


Fig. 4.7 Contact angle image of 3.5wt.%NaCl solution on a) substrate and b) the HVOF thermal sprayed 25(NiCr)-75Cr₃C₂ coating captured using the sessile drop method.

Fig. 4.7 (a) and (b) depicts the image showing CA of the 3.5wt.%NaCl solution droplet on the substrate and the 25(NiCr)-75Cr₃C₂ coating respectively. The CA of the substrate is found to be 67° which is hydrophilic. Whereas the CA of the as-

sprayed 25(NiCr)-75Cr₃C₂ found to be 98.14° and the CAH is found to be 15.51°, which indicates that the coated surface is of hydrophobic. The hydrophobic nature is attributed to the complex microstructure of the thermal spraying. The restricted dispersion of the 3.5 wt.% NaCl salt solution drop into the surface leaves air traps below the droplet. These air compartments and their associated capillary forces will lead to the adhesive capability of the droplets on the coating's surface. Further, it can also be inferred from the above result that the droplet is expected to enter into the larger scale grooves but not into the smaller scale grooves which are between the splats. The water droplet gets trapped at the edges of each micro-size splats containing nanopores, minute voids thereby introducing a significant energy barrier for the advancing liquid droplet that leads to the increase in CA (Feng et al., 2008). However, this water droplet gets sealed in between the splats that would restrict the contact line to recede during evaporation, which might be the reason for the negligible receding angle during CA measurement. We believe that the microstructure of the coating is responsible for the high CAH, which results in strong adhesion of water droplets on the coated surface (Feng et al., 2008). It is important for a cermet coating to maintain these properties even in harsh environments like saltwater. Hence, we performed the robustness check of the fabricated cermet coating by exposing it to saltwater. Our coating demonstrates that the 25(NiCr)-75Cr₃C₂ is of complex microstructure having a hydrophobic surface with good mechanical properties.

4.4 Summary and Conclusions

The present study examined HVOF coating of 25(NiCr)-75Cr₃C₂ Cermet on the mild steel substrate. The structural and morphological characterization of the coatings revealed different phases such as Cr₂O₃, Cr₃C₂, Cr₇C₃, and Ni present in the coating. The corrosion current density of the coated sample was found to be 6.878μA/cm⁻², whereas the current density of the substrate was 21.091μA/cm⁻². The corrosion rate of the coating sample was found to be 5 times less than the substrate. The Nyquist Impedance spectra were used to derive an equivalent circuit to analyze the interaction between the coating and electrolyte. The Bode Impedance plots obtained by EIS for the coating showed a typical passive material capacitive behaviour, indicated by medium to low frequency with phase angle approaching -60°, suggesting that a stable

film is formed on the tested material in the electrolyte used. A high saltwater contact angle (CA = 98.14°) and a high contact angle hysteresis (CAH-15.51°). The microhardness and the fracture toughness have increased after coating indicating an improvement in the mechanical properties.

In conclusion, the HVOF sprayed 25(NiCr)-75Cr₃C₂ coating on the low carbon steel substrate can improve the corrosion resistance, thereby increasing the service life of components in seawater applications. In addition, the sticky hydrophobic nature of the coating is obtained. The high advancing contact angle can be attributed to the local trapping offered by the complex microstructures present in the coating, whereas, the low receding angle is due to the sealing of the water droplet within the micro-island between the splats. Thus hydrophobic coating helps in improving the corrosion resistance in addition to the NiCr matrix. Also, the mechanical properties of the coatings showed an improvement in comparison to the substrate.

CHAPTER 5

Plasma sprayed α -Al₂O₃-GO composite: Corrosion, mechanical and wetting properties.

Outcome of Chapter 5

1. “Effect of graphene oxide loading on plasma sprayed alumina graphene oxide composite coating for improved corrosion resistance” submitted to ‘**Surface Topography: Metrology and Properties**’-IOP
2. “Plasma-sprayed graphene oxide reinforced alumina composite coatings on low carbon steel with improved fracture toughness, brittleness index and microhardness” (**Materials today: proceedings- Elsevier**)

CHAPTER 5

Plasma sprayed α -Al₂O₃-GO composite: Corrosion, mechanical and wetting properties

Overview

In this chapter, the spray-dried graphene oxide nanoplatelets reinforced alumina (α -Al₂O₃) were deposited on the low carbon steel substrate by Atmospheric Plasma Spray (APS) technique. The wt.% of GO are 0.5, 1.0, 1.5, and 2.0 wt.%. The GO-alumina nanocomposite coatings were characterized using XRD, Raman Spectroscopy, FTIR, XPS, FESEM, and HR-TEM. The porosity of the coatings is explained with the help of BET surface analysis. The corrosion behavior of the samples is investigated by LPR and EIS techniques. Further, the stability of the alumina-GO composites is discussed with the immersion test results. The mechanical and wetting properties of the alumina-GO composites are also discussed.

5.1. Introduction

Carbon-based nanocomposite materials play a significant role in improving the corrosion resistance, because of its enhanced mechanical, microstructural and electronic properties (Keshri, Huang, et al. 2010, Montemor 2014, Bisht et al. 2017, El-Shafai et al. 2019, Tiwari et al. 2019). Also, some of the nanocomposites show hydrophobic properties with improved corrosion protection (Montemor 2014, Vazirinasab et al. 2018, Singh et al. 2013, Wang and Kaneko 2013). Corrosion is one of the major problems in marine industries, oil and gas industries, thermal power plants, etc., and thereby causes huge financial loss world-wide (Finšgar and Jackson 2014, Iannuzzi et al. 2017, Lee and Berman 2018, Tong et al. 2016, Yu et al. 2018, Qiu et al. 2018). Therefore, there is a need for the development of corrosion-resistant coatings with advanced materials, while retaining the original properties of the substrate material. In this regard, the use of nanocomposite coatings has emerged as sought after coating materials to overcome these problems. Amongst the oxide ceramics for anticorrosion, Al₂O₃, referred as alumina, is an extremely important ceramic material, having several industrial applications (Krishnan et

al. 2006, Zhao et al. 2018, Schacht et al. 2000, Ćurković et al. 2008, Tallman et al. 2008, Park et al. 2018, Mirhashemihaghighi et al. 2016, Niazi et al. 2015).

Many researchers have worked on the synthesis and application of carbon nanomaterial and aluminum oxide composite coatings (Tallman et al. 2008, Yu et al. 2015, Nosbi and Akil 2015). The wear properties of carbon nanotube reinforced aluminum oxide nanocomposite coating by plasma spray technique revealed improved wear resistance (Balani et al. 2008). The tribological behaviour of carbon nanotube reinforced plasma sprayed aluminum oxide coating and comprehensive process maps to synthesize high-density plasma sprayed aluminum oxide composite coatings with varying carbon nanotube content has been reported (Keshri, Singh, et al. 2010). The tribological properties of graphene oxide doped alumina composite coatings are studied by (Yin et al. 2018). The anti-corrosion performance of alumina graphene oxide epoxy coatings have been reported by (Yu et al. 2015). The wear resistance and fracture properties of un-oxidized graphene/alumina nanocomposites are reported by (Kim et al. 2014). The wear resistance from the High-velocity Oxyfuel thermal sprayed Alumina-graphene nanocomposites is reported by (Murray et al. 2018). Therefore, alumina-carbon nanomaterial composites are an excellent combination to improve the properties. To the best of our knowledge, very few literatures on anticorrosion properties have been reported. There are no reports available for coatings with reinforcement of alumina-GO composite with varying GO wt.% using plasma spray technique with detailed electrochemical anticorrosion and the wettability studies.

5.2 Brief Methodology

Herein, we report the enhanced corrosion resistance of various wt.% of graphene oxide (0, 0.5, 1.0, 1.5, and 2.0 wt.%) in the alumina composite coating on the low carbon steel substrate using APS technique. The coatings were characterized using various techniques to confirm the retention of GO in the composite and quality of the coating. The corrosion, mechanical, and wetting properties of the coating were studied. On addition of 1.5 wt.% GO into the alumina matrix the anticorrosion properties and hydrophobicity of the coatings improved remarkably making it ideal for industrial applications.

5.3. Results and discussion

5.3.1 Dispersion of GO Nanoplatelets in the spray-dried alumina powder

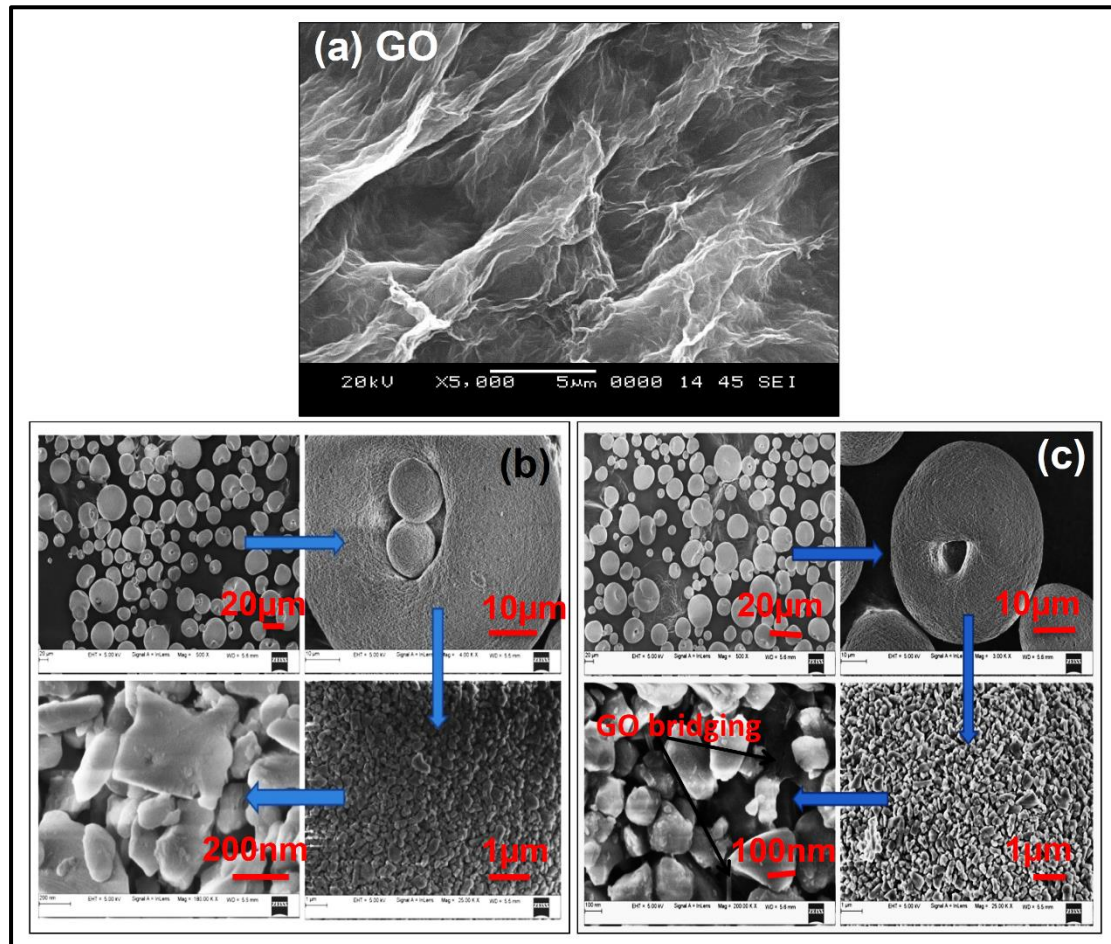


Fig. 5.1. SE images of powder distribution of a) GO nanoplatelets, b) spray dried alumina (SDA) and c) Spray-dried alumina with 0.5 wt. % GO Nanoplatelets (SDA-0.5GO).

The morphologies of the spray-dried powders are shown in **Fig. 5.1**. **Fig. 5.1 (a)** shows the FESEM image of as-prepared GO nanoplatelets, **Fig. 5.1 (b)** and **(c)** show the FESEM images of the SDA and SDA-0.5GO at lower and higher magnification respectively. The average agglomerate size of all the spherical powders is in 40–70 μm range. It is interesting to note that, the spherical and the doughnut-shaped agglomerates tend to reduce the inter-particle friction, thereby minimizing the blockage at the nozzle (Keshri et al 2011). This plays a considerable role in obtaining uniform and denser coatings. The dispersion of GO nanoplatelets in the $\alpha\text{-Al}_2\text{O}_3$ matrix can be witnessed from the FESEM

images of **Fig. 5.1** (c). The dispersion of GO nanoplatelets is identified from the bridging effect of GO nanoplatelets, which wrap the alumina particles with the Van der Waals force of attraction (Yu et al 2015).

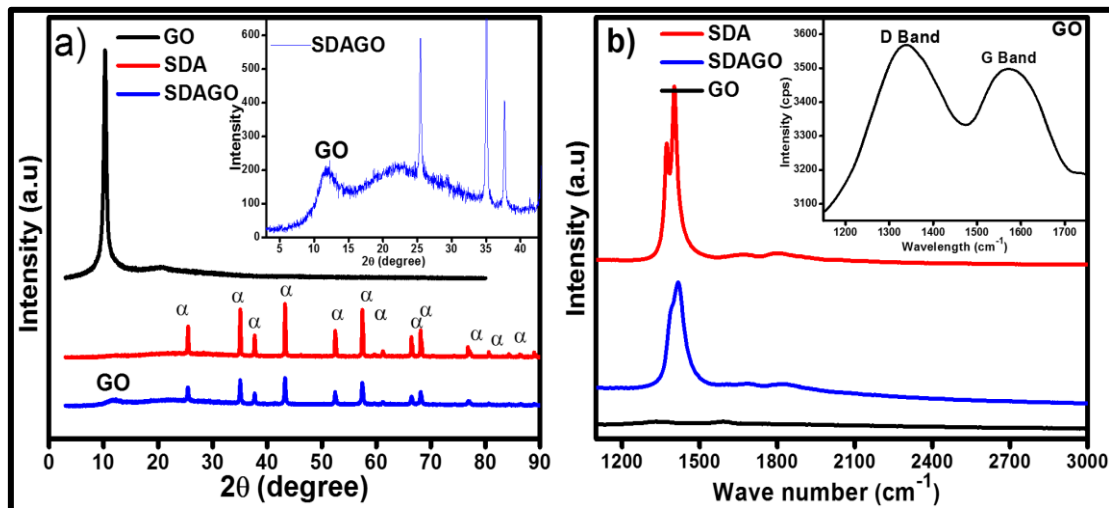


Fig. 5.2(a) X-Ray Diffractogram pattern and **(b)** Raman spectra of GO Nanoplatelets, SDA and SDA-0.5GO Nanocomposite powders. The inset in **(Fig. 5.2(a))** represents the enlarged XRD of SDAGO showing incorporation of GO to SDA and inset in **Fig. 5.2(b)** shows the enlarged image of the Raman spectra of GO nanoplatelets.

Fig. 5.2(a) shows the XRD patterns of GO nanoplatelets, SDA, and SDA-GO powders which revealing α - Al_2O_3 (JCPDS No 50-1496) and for GO, hexagonal carbon phase (JCPDS Card No.75- 1621). The inset of **Fig. 5.2(a)** confirms the reinforcement of GO platelets to the SDA while retaining the alpha structure of Alumina.

Fig. 5.2(b) shows the Raman spectroscopy for GO, SDA, and SDAGO. Two clear peaks at 1318cm^{-1} (D band) and 1584cm^{-1} (G band) are signatures of Graphene Oxide (Bagotia et al 2018, Tadyszak et al 2018) as shown in the inset of Fig. 2(b). The I_D/I_G ratio of GO spectra is 0.83, which gives evidence for the formation of GO (Rahman et al 2014). In the SDAGO composite, at 1484cm^{-1} the D band splitting is very small due to multiple layers of GO dispersion in the composite as reported by others (Kim et al 2014).

5.3.2 Structural and morphological analysis of the coatings

5.3.2.1 XRD Analysis

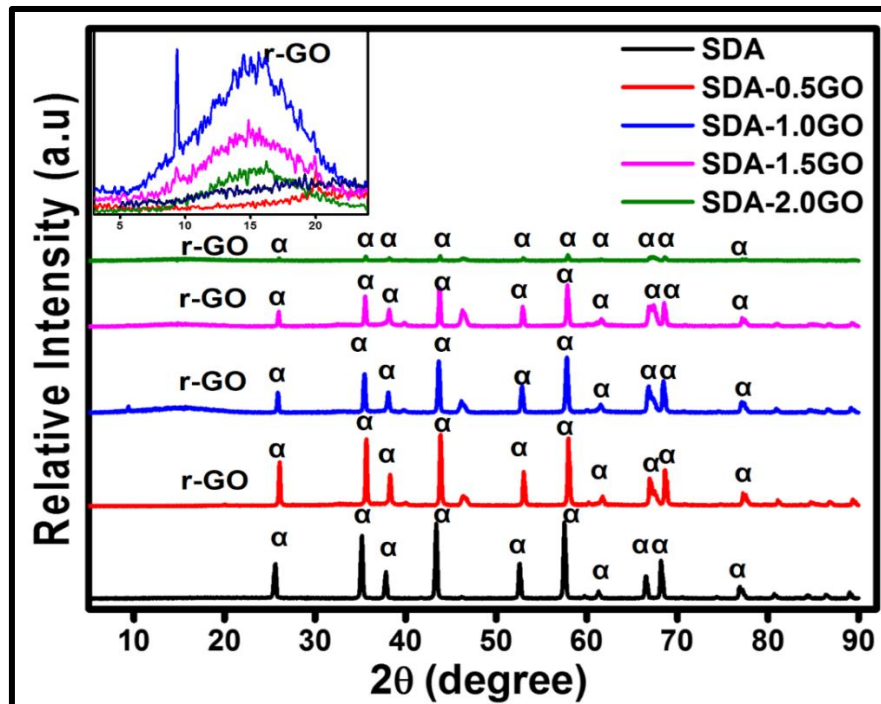


Fig. 5.3 X-Ray Diffractogram of SDA, SDA-0.5GO, SDA- 1.0GO, SDA- 1.5GO, and SDA- 2.0GO plasma-sprayed composites.

Fig. 5.3 depicts the XRD of atmospheric plasma sprayed coating of SDA, SDA-(0.5, 1, 1.5, and 2 wt. %) GO composites. The XRD phase analysis of plasma spray coatings showed the α -phase in alumina coated on the steel substrate. A broad peak at diffraction angle 17° corresponds to r-GO and a peak at 9.32° corresponds to GO. The diffraction angles at 25.36° , 35.52° , 43.82° , 52.94° , 58° , and 66.98° correspond to (012), (104), (110), (113), (024), (116) and (214) planes respectively for alpha phase according to JCPDS No. 50-1496. The diffraction angle at 39.84° corresponds to (311) reflections of the gamma phase (JCPDS No. 00-010-0425)(Samain et al 2014). A slight shift in the peak positions of SDA-GO composites is observed when compared to bare alumina coating. Therefore, XRD confirms the presence of the α - Al_2O_3 phase in the composite with GO. It may be noted that the peak intensity has decreased as the percentage of GO is increased and is least for the 2.0 wt% GO addition. The decrease in the intensities of plasma

sprayed SDA-GO are due to the presence of carbon as percentage of GO is increased (Tchomgui-Kamga et al 2010).

5.3.2.2 Raman Spectroscopy Analysis:

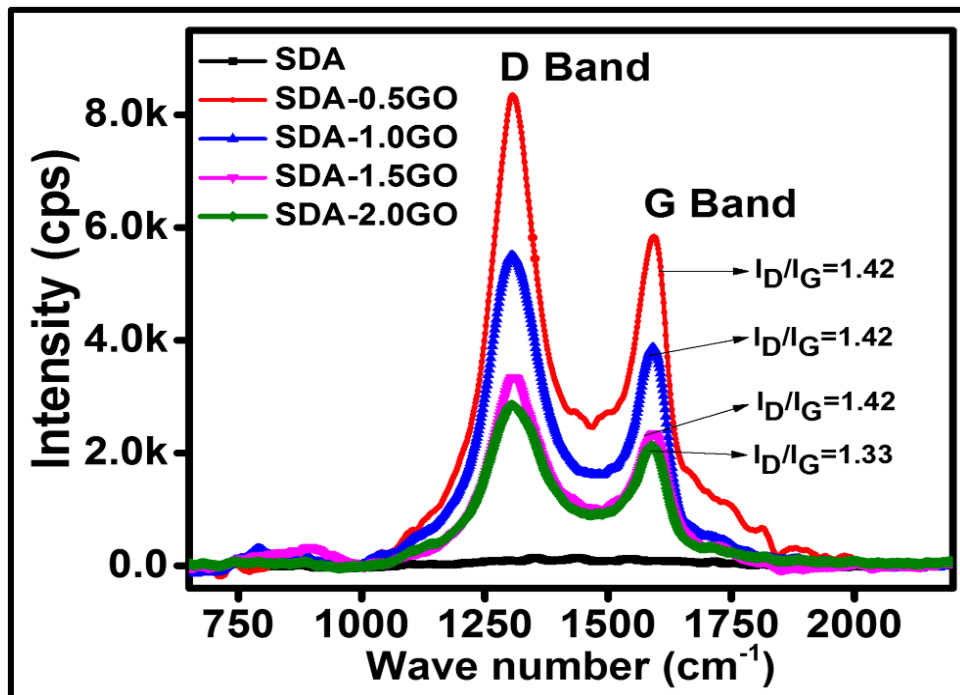


Fig. 5.4 Raman spectroscopy of SDA, SDA-0.5GO, SDA- 1.0GO, SDA- 1.5GO, and SDA- 2.0GO plasma-sprayed composites.

Furthermore, to confirm the existence of graphene oxide nanoplatelets in the coating, the Raman spectroscopy analysis was performed. **Fig. 5.4** shows the Raman spectra of SDA, SDA-0.5GO, SDA- 1.0GO, SDA- 1.5GO, and SDA- 2.0GO plasma-sprayed composites. The G and D peaks in the Raman spectra of SDA-GO composites are the direct demonstration of GO reinforcement in the composites (Xie et al 2015). In comparison to pure SDA coatings, the GO nanoplatelets reinforced SDA-GO composites show the two distinct characteristic peaks of graphene, which are observed at $\sim 1308 \text{ cm}^{-1}$ called D band and at $\sim 1590 \text{ cm}^{-1}$ called G band. This observation confirms the retention of GO nanoplatelets in the plasma sprayed coatings. The I_D/I_G ratio gives the defect density information of the coatings. The I_D/I_G ratio of SDA-0.5GO, SDA-1.0GO, SDA-1.5GO composites are 1.42 and that of SDA-2.0GO is 1.33. A similar observation is reported that the GO and rGO will have more defect density when compared to graphene (King et

al 2016a). The defect density is mainly due to the sp^2 bonds of the GO. The decrease in the I_D/I_G ratio of SDA- 2.0GO in comparison to lower percent composite coatings gives evidence for better performance (Cygan et al 2017, Yazdani et al 2015).

5.3.2.3 FTIR Analysis

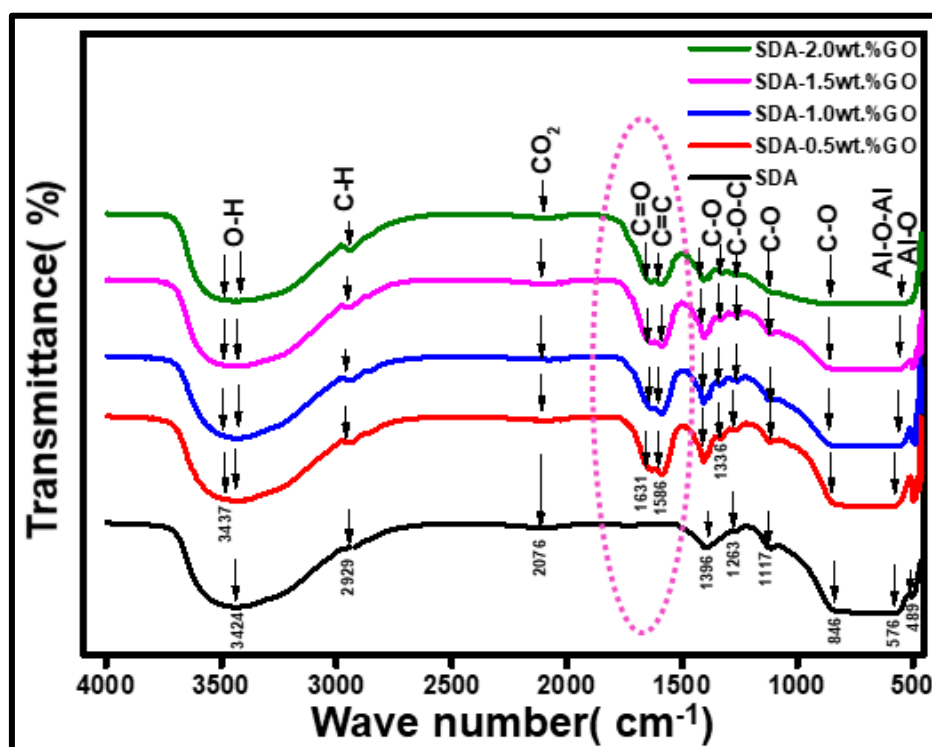


Fig. 5.5 FTIR spectra of as-synthesized SDA and SDA-(0.5, 1.0, 1.5 and 2.0) wt.% GO coatings.

Fig. 5.5 shows the typical FTIR spectra of as coated SDA and SDA-(0.5,1.0,1.5 and 2.0)wt.%GO. **Table 5.1** gives the different vibrational modes owing to different functional groups. Concerning the characteristics exhibited by parent graphite, the FTIR confirmed the successful incorporation of GO by the appearance of peaks at 1719, 1366, 1176, and 1050 cm^{-1} attributed to oxidation functional groups namely carbonyl, carboxyl, hydroxyl, and epoxy. On the other hand, the peak at 1631 cm^{-1} corresponds to graphitic domains indicating the presence of unoxidized graphite. The broad band above 3000 cm^{-1} in the GO spectrum is attributed to adsorbed water. In SDA and SDA-GO spectra the bands at 600-900 cm^{-1} correspond to Al-O-Al functional groups whereas bands at 1100 to 1200 cm^{-1} are attributed to C-O-C functional groups and bands at 1700-1800 cm^{-1} are of

C=O functional group. The peaks at 1631 cm^{-1} and 1586 cm^{-1} corresponding to C=O and C=C vibrations gives evidence for the incorporation of Graphene oxide in the SDA-(0.5, 1.0, 1.5 and 2.0)wt.% GO composites.

Table 5.1 Characteristic IR functional groups of GO, SDA, and SDAGO

Bands [cm^{-1}]	Vibrations
600-900	Al-O-Al vibrations
1100-1200	C-O-C vibrations
1700-1800	C=O vibrations
Above 3000	Adsorbed water (-OH) band

5.3.2.4 XPS analysis

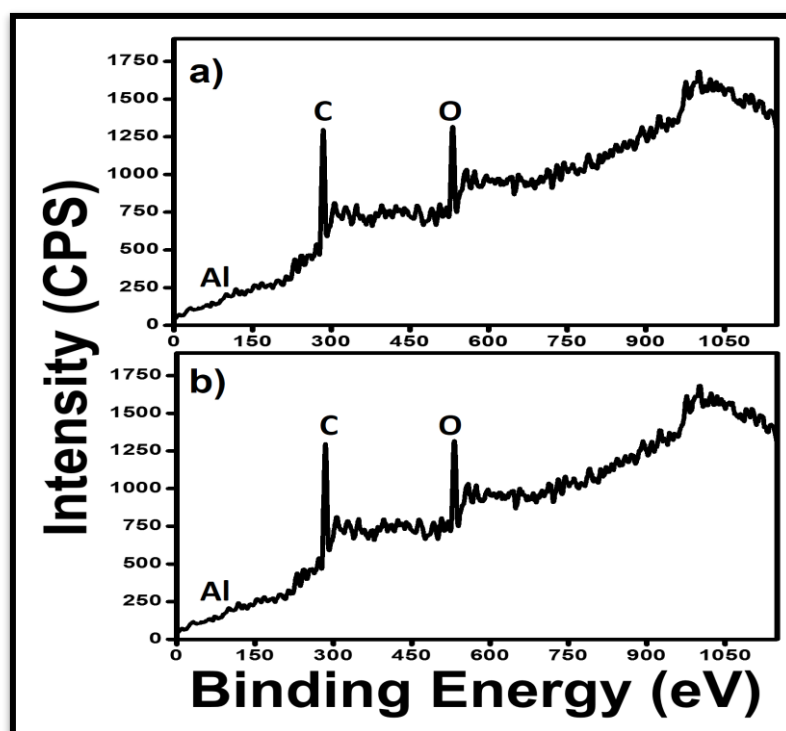


Fig. 5.6 XPS survey spectra of (a) SDAGO powder and (b) SDAGO plasma sprayed coatings.

XPS reveals the changes in the binding energies and the existence of multiple bands related to different elements associated with it. **Fig. 5.6**(a) and (b) represent the XPS survey spectra of SDAGO powder and SDAGO coatings respectively. Also, XPS analysis of SDA coating and SDAGO composites were also interpreted for the O1s, Al2p, and C1s as depicted in **Fig. 5.7** by spectral characterization. The bands are compared with the

reported values (Paparazzo 1986). The spectrum of each sample reveals the peaks for O1s, Al2p, and C1s, indicating the presence of O, Al, and C. Also, the major peaks indicate that the coatings have retained their chemical composition without any decomposition.

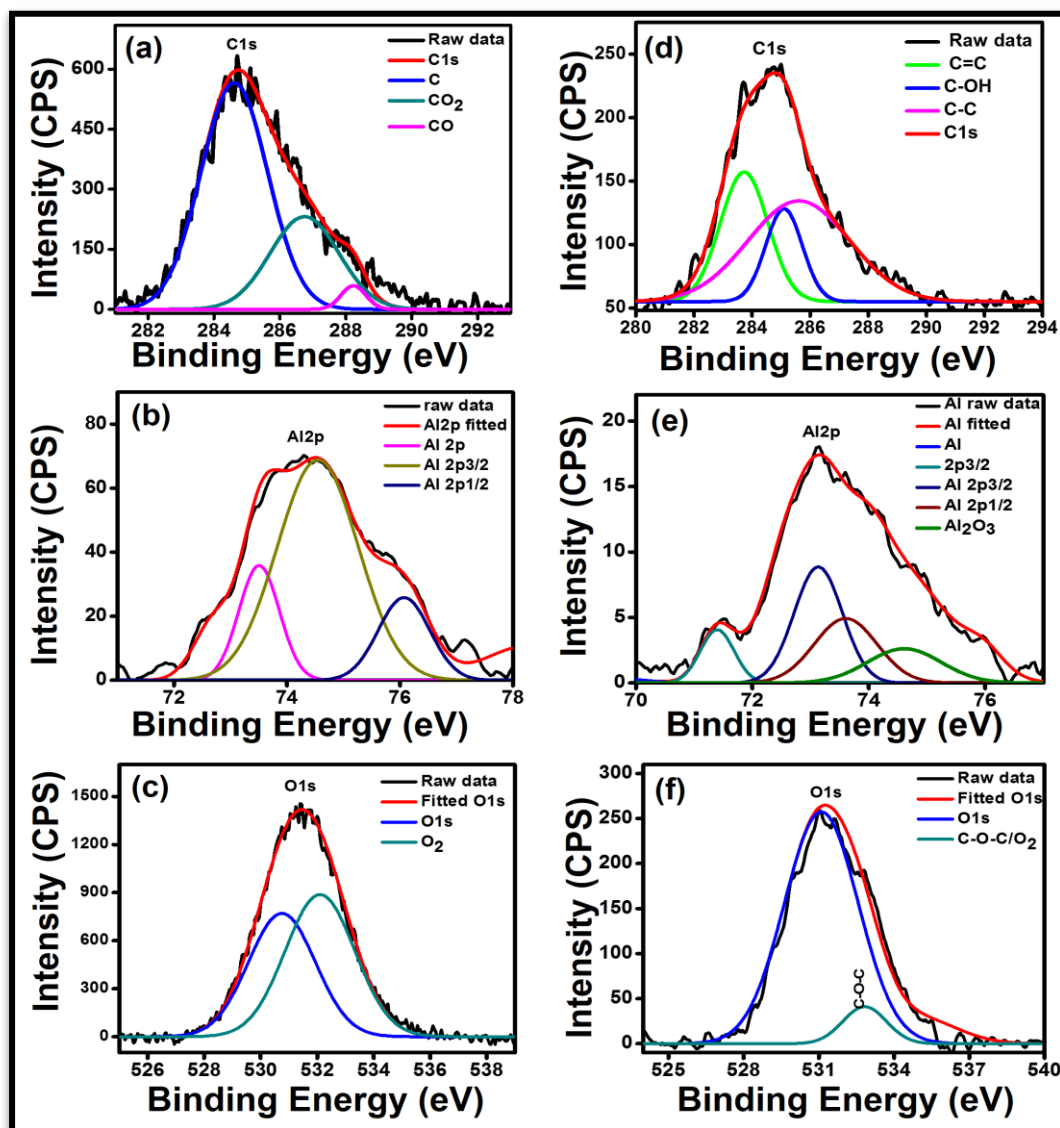


Fig.

5.7 XPS spectra of a) carbon (C1s), b) aluminum (Al2p), c) oxygen (O1s) of SDA coatings and d) C1s, e) Al2p and f) O1s are of SDA-0.5GO composite coatings.

5.3.2.5 FESEM Analysis

Fig. 5.8 (a), (b), (e), (f) and (g) show the surface morphologies of APS coating of SDA, SDA-(0.5, 1,1.5 and 2.0 wt.%GO) composites respectively. The morphological observation of SDA shows the larger pores and some microcracks, whereas the SDAGO shows the smaller pores along with the GO sheets. The large GO sheets are distinguished from the alumina splats using the EDS mapping taken on the respective regions. The EDS mapping taken on the alumina splat region and on the graphene oxide flakes region is shown in **Fig. 5.8** (c) and **Fig. 5.8** (d) respectively. The elemental mapping corresponding to carbon in **Fig. 5.8** (d) gives evidence for the presence of GO nanoplatelets with 40.78 wt. % of carbon content.

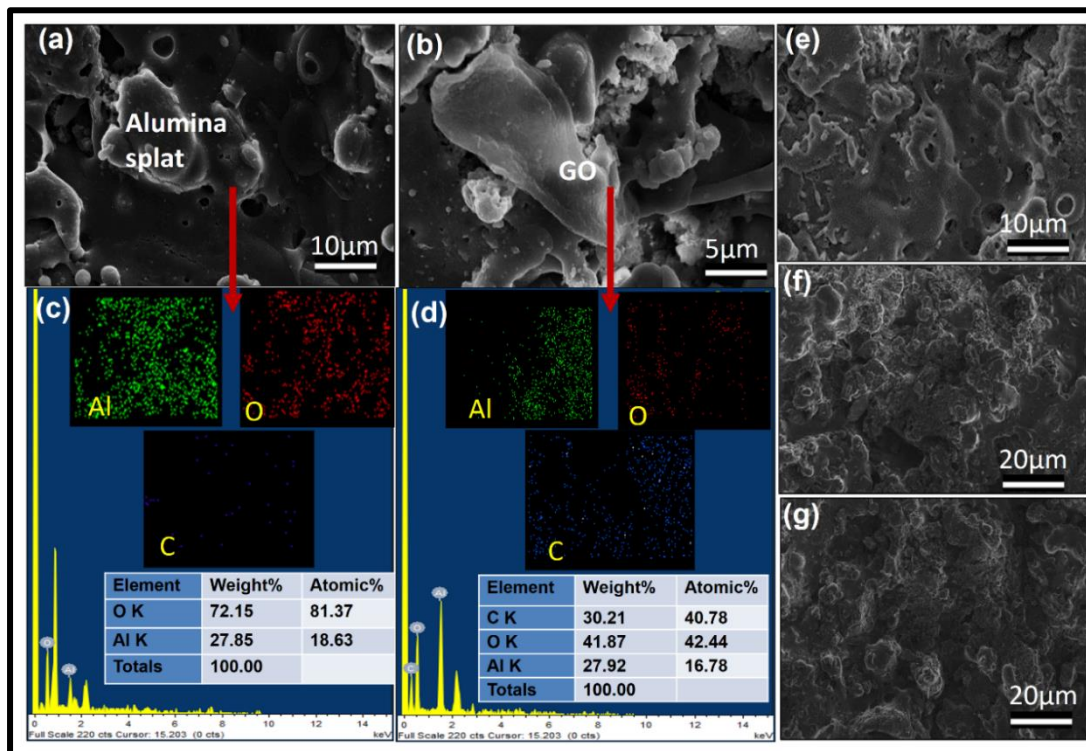
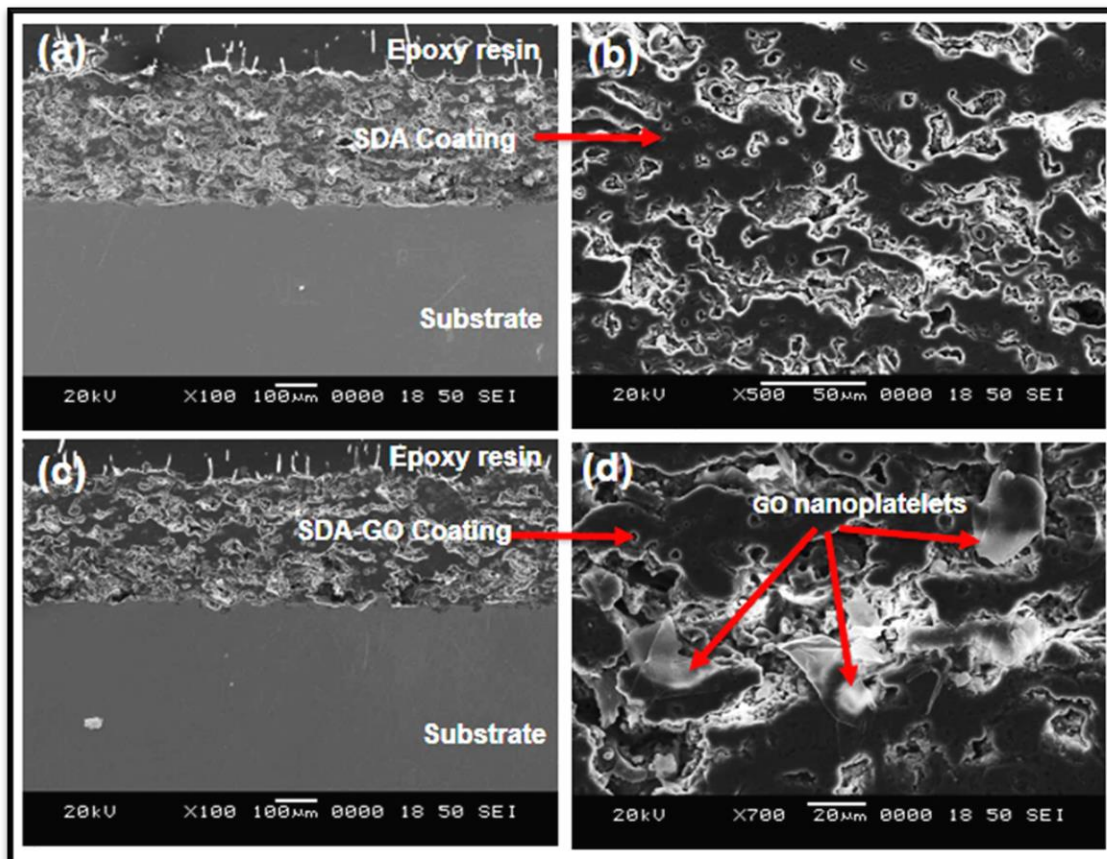


Fig. 5.8 SE surface morphology of a) SDA, b) SDA-0.5GO, e) SDA-1GO, f) SDA-1.5GO g) SDA-2GO coatings, and c) and d) EDS mapping on alumina splat region and also on GO flakes region respectively, revealing the high carbon content in the GO region compared to alumina splat.

Fig. 5.9 shows the cross-section of the coatings SDA and SDA-2.0GO. The interface of the cross-section of SDA and SDA-2.0GO shows the well-adhered coatings on the substrate with a thickness of around 300 μm . The FESEM cross-sectional images



showing the thickness of the SDA-0.5GO, SDA-1.0GO, and SDA-1.5GO are given in **Fig. 5.10**.

Fig. 5.9 SEM showing surface morphology at the cross-section of a) SDA, b) SDA coating at higher magnification, c) SDAGO Coating and d) SDAGO showing GO nanoplatelets at 2.0 wt.% GO in the coatings.

The microstructure reveals the regions of the re-solidification of the coating during the plasma spraying process. The more uniform coating with larger splats is witnessed at higher magnification. The GO nanoplatelets are seen in the SDAGO with higher 2wt.% of GO as shown in **Fig. 5.9** (d). The morphology of the GO flakes in the composites is as per the observation made by (Cygan et al 2017, Murray et al 2018, Xie et al 2015).

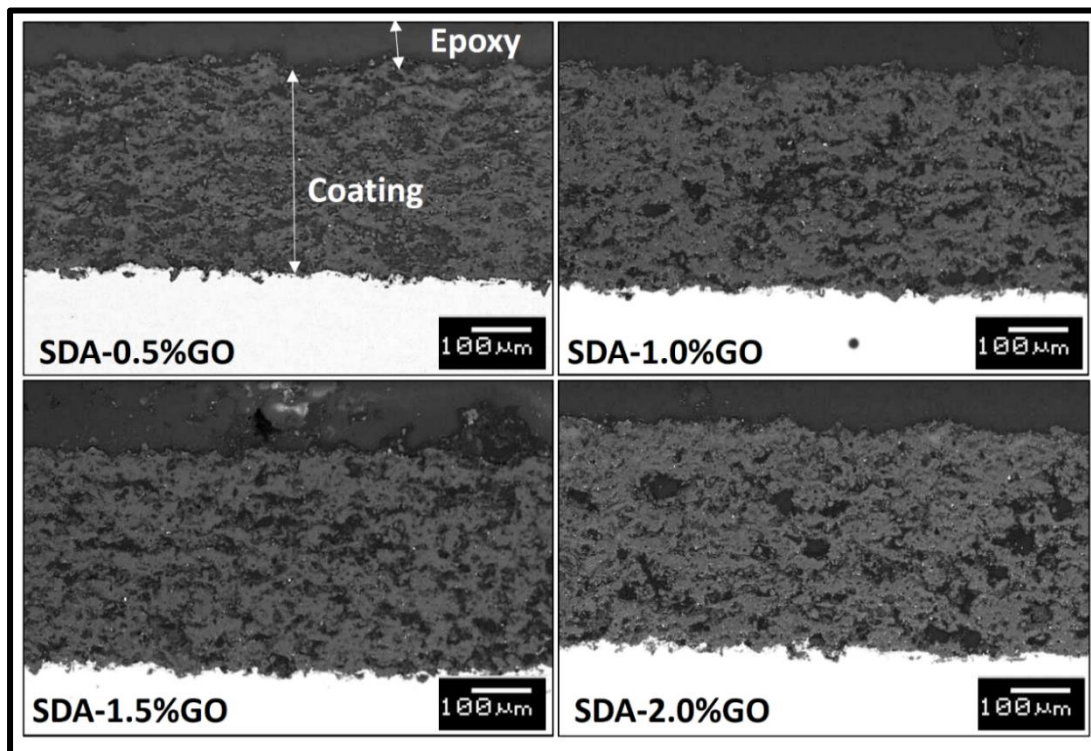


Fig. 5.10 The FESEM images showing thickness of the plasma sprayed coatings of SDA-0.5%GO, SDA-1.0%GO, SDA-1.5%GO and SDA-2.0%GO composites.

5.3.2.6 TEM analysis

Fig. 5.11 illustrates the HR-TEM image of GO nanoplatelets, Alumina and the GO fastened between Al_2O_3 splats with resultant SAED patterns. The HR-TEM image of GO and SDA are shown in **Fig. 5.11** (a) and (b) respectively while, the HR-TEM images of SDA-(0.5, 1.0, 1.5)GO in **Fig. 5.11** (c) to (e) indicate the presence $\alpha\text{-Al}_2\text{O}_3$ -GO nanocomposites. It is evident from these images that alpha alumina has spread on the reduced graphene oxide sheets. **Fig. 5.11** (f) shows the SDA-2.0GO nanocomposites with agglomeration. The interplanar spacing between planes in SDA-GO composites are shown in the insets of the images (Kellici et al 2017). The d spacing of alumina is found to be about 0.20 nm. One can further notice that interface between Al_2O_3 and GO nanoplatelets is free from any lattice distortion. The presence of spotless interface through GO nanoplatelets into $\alpha\text{-Al}_2\text{O}_3$ matrix may enhance the corrosion resistance ability of the coatings.

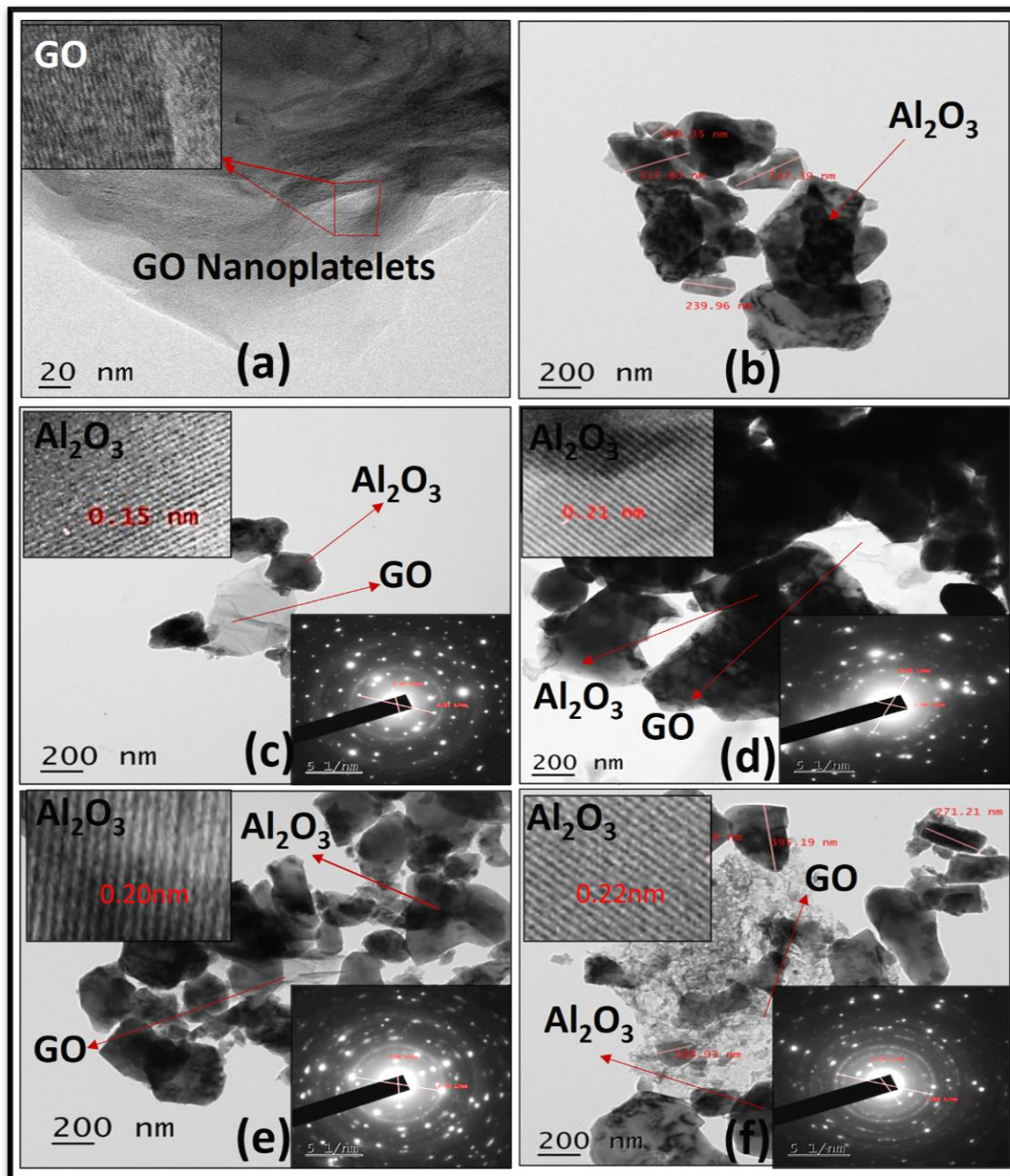


Fig. 5.11 HR-TEM images of a) GO nanomaterials b) SDA c) SDA- 0.5GO d) SDA- 1.0GO e) SDA- 1.5GO and f) SDA- 2.0GO with d spacing of Al_2O_3 and their corresponding SAED patterns.

5.3.3 Electrochemical Corrosion properties of the coatings

5.3.3.1 Linear polarization resistance (LPR) Measurements

LPR measurements were carried out around an equilibrium potential of 50 mV, at a scan rate of 0.166 mVs^{-1} . The electrochemical corrosion parameters have been obtained using the linear polarization curve viz., Tafel plot. The polarization resistances have been calculated using the current density and the Tafel slopes. The corrosion rates (CRs) have been determined by the Tafel extrapolation method. **Fig. 5.12** (a) shows the Tafel plots of the plasma sprayed coatings. The corrosion potential (E_{corr}), corrosion current density (I_{corr}) was obtained from the intersection point of anodic (β_a) and cathodic (β_c) branch of Tafel slopes. Polarization resistance (R_p) is calculated using Stern Geary equation 2.3 whereas, the corrosion rate (CR) is calculated according to G102 ASTM standard using equation 2.4 (Singh et al 2016).

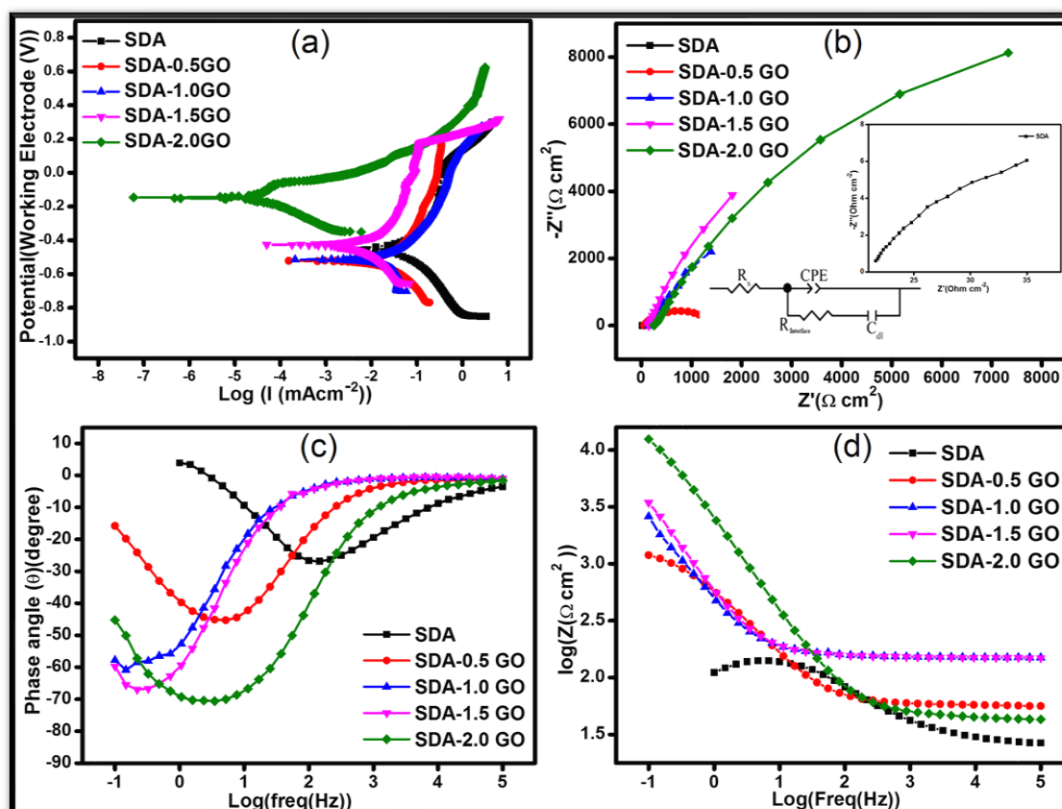


Fig.

5.12 a) Tafel plot b) Nyquist plot (inset shows Nyquist plot of SDA and equivalent circuit) c) Bode plot and d) Bode impedance plot of plasma sprayed coatings of SDA, SDA-0.5GO, SDA-1.0GO, SDA-1.5GO and SDA-2.0GO on the substrate.

The corrosion rates of all the composites are given in the **Table 5.2**. The reduction in corrosion current density is an indication of reduction in the corrosion rate. The R_p values for the GO reinforced alumina coatings has increased, while the CR has decreased as the wt.% of GO is increased. But, for 2.0 wt.% addition of GO to the alumina, the saturation of corrosion resistance is observed (**Table 5.2**). The corrosion rate (CR) of SDA-1.5GO and SDA-2.0GO are 0.375×10^{-6} and 0.257×10^{-6} mmpy respectively. Similarly, the corrosion current of 1.5 and 2 wt.% GO loading are 1.5×10^{-5} and 1.0×10^{-5} $\mu\text{A cm}^{-2}$ respectively. This indicates the six order improvement in the corrosion resistance that has been achieved with just 1.5 wt.% addition of GO to the Al_2O_3 (Ding et al 2018).

Table 5.2 Electrochemical parameters obtained by Tafel extrapolation

Sample	E_{corr} (mV)	I_{corr} ($\mu\text{A cm}^{-2}$)	β_a (mV)	β_c (mV)	CR (mmpy)
SDA	451.908	47.306	293.2	250.7	0.666
SDA-0.5GO	-461.141	8.463	321.1	295.2	0.212
SDA-1.0GO	-156.612	9.0×10^{-3}	62.1	81.8	0.234×10^{-3}
SDA-1.5GO	-146.644	1.5×10^{-5}	58.4	73.6	0.375×10^{-6}
SDA-2.0GO	-144.662	1.0×10^{-5}	59.9	81.0	0.257×10^{-6}

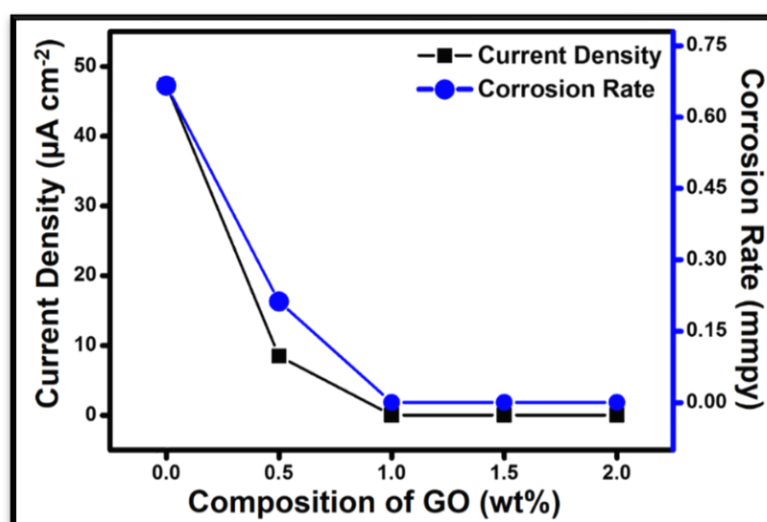


Fig. 5.13 Variation of Current density and corrosion rate as a function of composition.

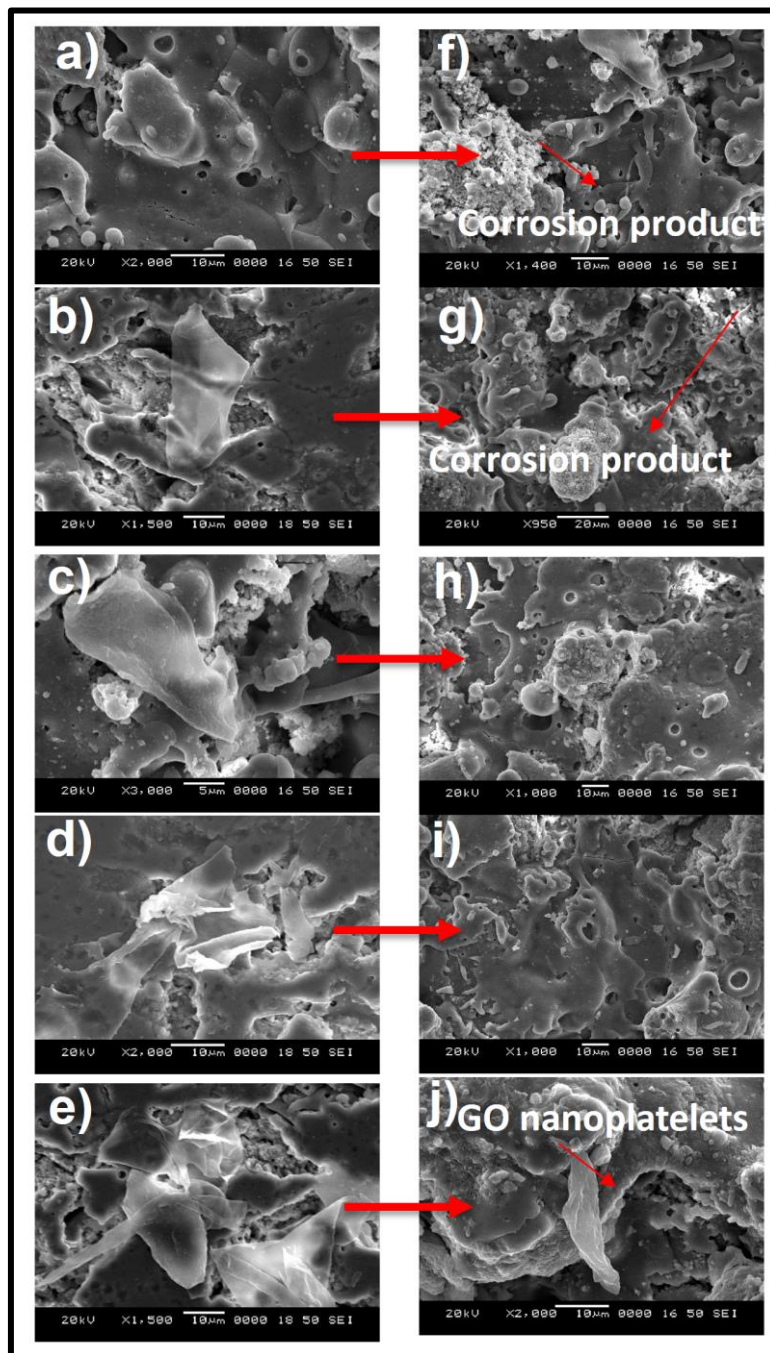


Fig. 5.14 (a), (b), (c), (d) and (e) SEM morphology of SDA and SDA(0.5, 1.0, 1.5 and 2.0)GO composites before corrosion and, (f), (g), (h), (i) and (j) after corrosion test respectively.

The surface morphology of SDA and SDA-(0.5, 1, 1.5, and 2.0 wt.%)GO coatings before and after corrosion are given in **Fig. 5.14**. The variation in the current density and the

corrosion rates are given in **Fig. 5.13**. The (1.5, and 2.0 wt.%) GO- alumina coatings are more stable when subjected to electrochemical corrosion tests.

5.3.3.2 Electrochemical impedance spectroscopy (EIS) Measurements

The electrochemical properties of plasma-sprayed SDA and SDA-(0.5, 1.0, 1.5 and 2.0 wt. %)GO nanocomposites coatings were determined using EIS measurements. **Fig. 5.12** (b) portrays the Nyquist plots of SDA, SDA-0.5GO, SDA-1GO, SDA-1.5GO, and SDA-2GO samples registered in 3.5 wt.% NaCl solution with an applied frequency range of 100 mHz to 200 KHz at an AC signal of 10 mV amplitude. The inset in **Fig. 5.12** (b) is the enlarged Nyquist plot of SDA coating. Nyquist plots of all samples show single incomplete semicircle arcs, and it is in the order SDA <SDA-0.5GO<SDA-1GO<SDA-1.5GO<SDA-2GO, which indicates higher corrosion resistance with the higher wt.% reinforcement of GO. Using the equivalent circuit model (inset in **Fig. 5.12** (b)) Nyquist plots were fitted as per equation 3.1 and the important circuit parameters are presented in **Table 5.3**.

Table 5.3 Equivalent circuit fitting elements.

Sample	$R_s(\Omega)$	$Q(\text{CPE}) (\mu\text{F})$	$R_{ct} (\Omega)$
SDA	-477.887	21.091	128.6
SDA-0.5GO	56.92	229.6	1530
SDA-1.0GO	152.70	812.1	19802
SDA-1.5GO	146.9	548.6	31757
SDA-2.0GO	45.30	103.4	25809

The solution resistance R_s is owing to the formation of metal ions at the interface is due to electrochemical reactions. The corrosion rate is controlled by the migration of ions and the electrochemical reactions taking place at the interface (Meng et al 2016). The R_{ct} indicates interfacial charge transfer (Hong et al 2002). Since R_{ct} is the measure of electron transfer across the surface, it is inversely proportional to the rate of the corrosion process, indicating that (0.5, 1.0, 1.5 and 2.0 wt.%) GO reinforced alumina coatings have less corrosion rate (Gong et al 2015, Tong et al 2016, Zhang et al 2018). However, 1.5 wt.% GO was found to show the highest R_{ct} (31,757 Ω) and 2.0wt% is found to be 25,809 Ω .

This further confirms improved corrosion resistance at higher percentage of GO addition to alumina.

The Bode plots for the impedance of the coatings are depicted in **Fig. 5.12** (c) and (d). In **Fig. 5.12** (c) the phase angle versus the frequency are presented and in **Fig. 5.12** (d) Bode impedance plot, resistance versus the frequency are presented. The phase angle plot for SDA and SDAGO composite coatings show the single time constant. The phase angle of SDA is of 27° . The phase angle increased with the percentage of the GO content and is 73° for 2.0 wt.% GO addition, which indicates good corrosion-resistant coating. Further, when compared to SDA coating, the phase angle for SDAGO coating has increased. The increase in the Bode phase angle suggests that there is a formation of a passive layer, which protects the further corrosion. The lack of a low-frequency time constant indicates the absence of corrosion processes at the surface of the composite coatings forming a passive layer because the GO acts as the anodic ion barrier. In addition, the impedance at the higher frequency is more and it has increased as the GO content is increased in the SDAGO composite coatings.

LPR and EIS results reveal that the corrosion inhibition of the SDAGO is better than that of pristine SDA. The inhibitory effects of r-GO can be attributed to thicker GO films in the coating formed due to the plasma spray process. Also, graphene oxide layers form bridging/stacking between the alumina splats, thereby blocking the interfaces, in addition, to cover the surface. This could effectively block the interfacial percolation of electrolyte from the surface into the bulk. Further, the high corrosion resistance is due to the chemical stability, chemical inertness, and impermeability to ion diffusion properties of sp^2 hybridized carbon nanostructure present in the SDAGO coatings.

5.3.4 Mechanical properties of the coatings

Fig. 5.15 (a) shows the Vickers hardness of plasma-sprayed alumina and its composites with GO reinforcement. The microhardness value of the SDA is about 4.148 GPa and decreased as the percentage of GO addition was increased in the composites in comparison to SDA. The highest values were measured for a small weight percentage of GO nanoplatelets (0.5 wt. %) with SDA. Further with the increase in the GO content in

the composite, the hardness decreases (**Table 5.4**). The hardness is least for the SDA-2.0GO composite. The change in the hardness indicates good dispersion of the reinforcing GO phase in the alumina matrix. The GO acts as the lubricant in the SDA matrix. The increase in the percentage of GO nanoplatelets in the composite, inhibits the ceramic grain growth, although the higher percentage of GO leads to the creation of agglomeration.

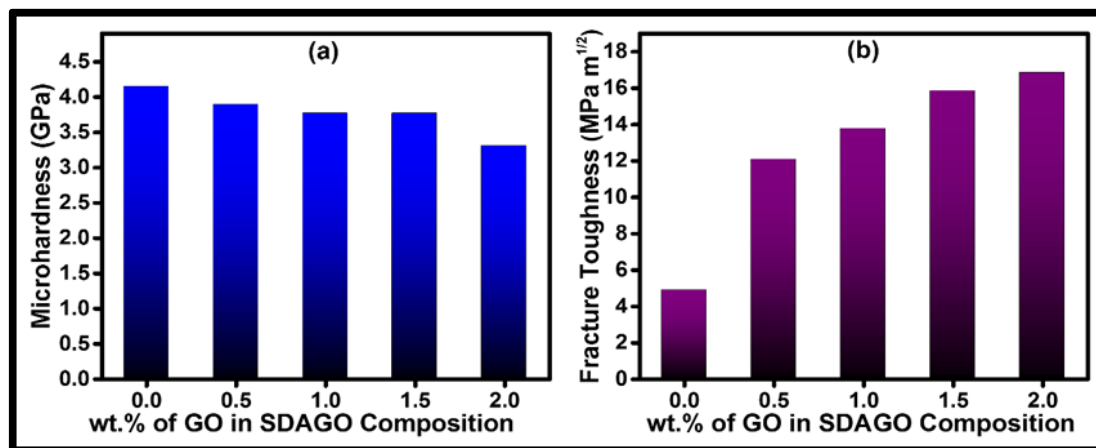


Fig. 5.15 a) Variation of microhardness and b) variation of fracture toughness of the plasma sprayed coatings SDAGO composites as a function of GO wt.% addition.

Table 5.4 Mechanical properties of SDA and SDAGO composite coatings.

Sample	Microhardness [GPa]	Brittleness index [Bi]	Fracture Toughness [MPa m ^{1/2}]
SDA	4.148	853	4.86
SDA-0.5GO	3.893	323	12.06
SDA-1.0GO	3.766	274	13.75
SDA-1.5GO	3.766	238	15.85
SDA-2.0GO	3.305	196	16.85

Fig. 5.15 (b) shows fracture toughness as a function of the weight percentage of GO in SDAGO composite. It is evident from **Table 5.4** that with the addition of 0.5wt.% GO the fracture toughness has increased to threefold from that of SDA. Thereafter the increment in fracture toughness is slower as the wt.% of GO increased and four times increment can be observed for the SDA-2.0GO composite. Also, the brittleness index of the SDA-2.0GO has decreased four times in comparison to SDA.

Thus, a little sacrifice on the hardness, a drastic improvement in the fracture toughness and ductility are obtained. The homogeneously dispersed graphene oxide in the SDA has led to enhanced fracture toughness and decreased brittleness index due to the graphene interface sliding effect and crack bridging of graphene sheets with the alumina.

5.3.5 Wetting properties of the coatings

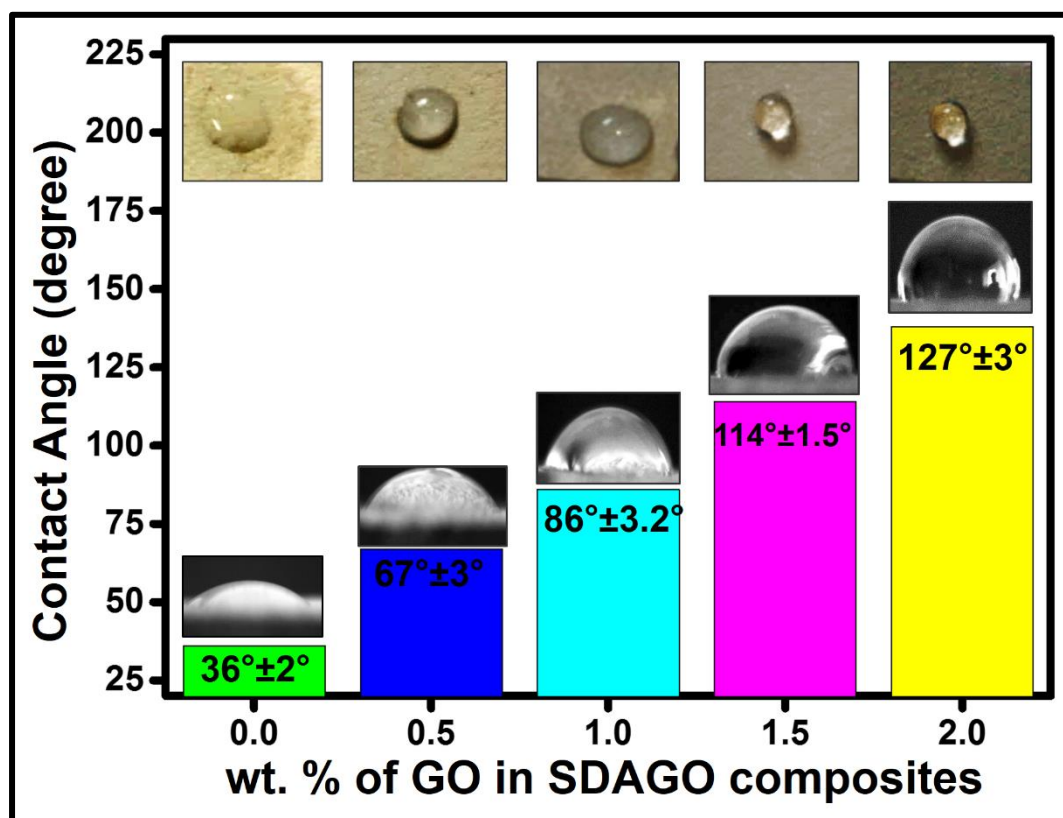


Fig. 5.16. Contact angle measurement variation as a function of wt.% GO nanoplatelets addition to Alumina. The inset shows the top view photograph of the corresponding coatings showing 3.5 wt.% NaCl solution droplets and contact angle measured images.

Contact angle (CA) measurement is an effective tool to study the wetting properties of the corrosion-resistant coatings (Románszki et al 2013). To find out the contact angle of the coatings, 3.5wt.% NaCl is used as the liquid. About 10 μ l of the liquid is dropped on the surface of the coatings and also the substrate. The focused image of the liquid drop is captured and the CA is measured with the help of the contact angle meter. **Fig. 5.16** shows the static contact angles for the plasma spray coating of SDA and SDA (0.5, 1.0, 1.5, and 2.0) GO and also the increasing trend of the contact angle with a percentage of GO nanoplatelets. The CA is tuned from 36.2° to 127° with GO loading. The CA of the

substrate is 70° (already given in chapter 3). As evident from **Fig. 5.16**, the SDA coating has the least CA of 36.2° , indicating the hydrophilic nature of the coatings. With the addition of GO nanoplatelets to the alumina, the hydrophilic nature has disappeared and the coated surface turns out to be hydrophobic. The CA values of 1.5 and 2 wt.% GO loading are close to each other. Larger the CA, lesser is the surface energy, which is due to the weaker adhesion of the 3.5 wt.% NaCl droplet to the coating surface. The wrinkled or folds of graphene oxide flakes (as seen in FESEM and TEM images) entrap the air bubbles, which drastically reduces the contact area of the 3.5 wt. % NaCl solution droplet with nano-protrusions in addition to nanopores (King et al 2016b).

It can be noted that thin layers of graphene oxide reveal hydrophilicity whereas, thicker coating of graphene oxide consisting of double-layer or more reveals hydrophobicity as reported by the literature (Munz et al 2015) and as evident from FESEM images of the SDAGO coatings. Also, the plasma spray results in an in-situ reduction of graphene oxide to r-GO. Since, the plasma spray process is a high-temperature process where, melting and re-solidification of alumina- graphene oxide composite takes place. Therefore, it is evident that due to plasma spray, not only the graphene oxide is reduced to r-GO but also, forms thick layers, making the coating hydrophobic. Hence, the plasma sprayed coating resulted in a hydrophobic surface with contact angles greater than 90° (Kantesh et al 2009, Prajitno et al 2016, Zhang et al 2017).

5.3.6 Porosity of the coatings

Further, from the BET results, the pore diameters are obtained for SDA and SDA-(0.5, 1.0, 1.5, and 2.0) wt.%GO are depicted in **Fig. 5.17**. The pore diameters of SDA and SDA-2wt.%GO coatings are 10.185 nm and 1.485 nm respectively showing a drastic decrease in the pore size. The specific surface area obtained by BET surface analysis of SDA is $29.609 \text{ m}^2\text{g}^{-1}$ and that of SDA-2wt.%GO is $48.607 \text{ m}^2\text{g}^{-1}$. This suggests that the pore size has decreased upon the incorporation of GO nanoplatelets, which implies that the porosity has decreased. The nanopores of SDAGO thus acts as the hydrophobic surface (Yang et al 2008). This hydrophobic surface acts as a protective layer by preventing the corrosion process. Because, the air trapped in the micro and nano-pores in the graphene oxide surface acts as the water repellent, thereby slowing down the further oxidation and breakdown of the passive film (Aryal et al 2015, Li et al 2014, Mohamed et

al 2015, Yu & Tian 2014). Thus, the SDAGO composite coatings act as excellent anticorrosion coatings with low wettability, by turning into a hydrophobic surface.

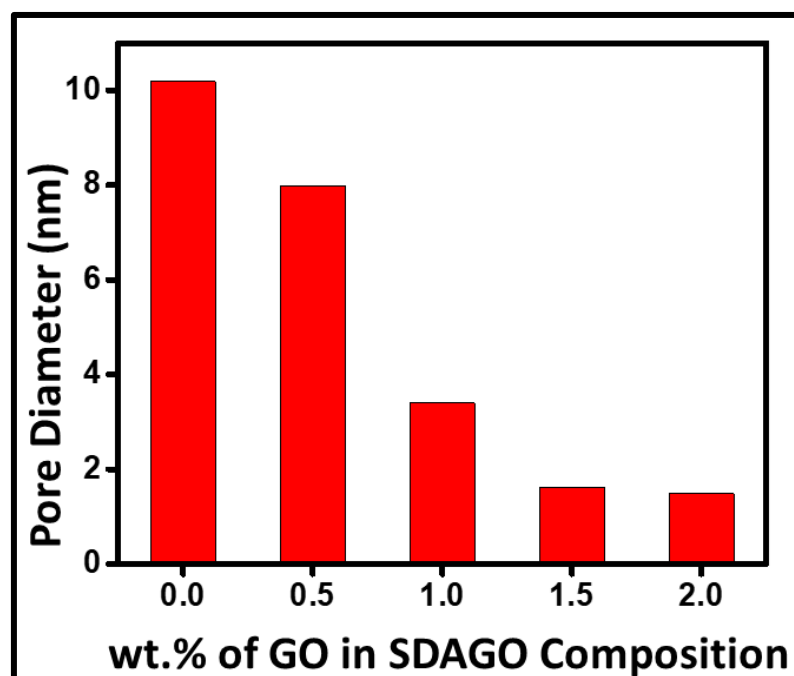


Fig. 5.17 pore diameter (pore size) as a function of GO wt.% in SDA-GO composite

5.4 Summary and Conclusions

Graphene oxide nanoplatelets (0.5, 1.0, 1.5, and 2 wt.%) reinforced in alumina (α - Al_2O_3) nanocomposite coating is employed for corrosion protection of low carbon steel, using atmospheric plasma spray technique. The XRD, FTIR, Raman spectroscopy, FESEM, and TEM characterization techniques revealed the retention of GO in the SDA-GO composite even after the plasma spray coating. The surface corrosion resistance improved nearly six orders of magnitude when coated with 1.5 and 2.0 wt.% GO reinforced alumina nanocomposite, in comparison with bare Al_2O_3 coating. The mechanical properties of atmospheric plasma-sprayed SDA and SDA-xGO coatings on low carbon steel was evaluated using the Vickers indentation technique, and the effects of GO addition in microhardness brittleness index and fracture toughness were investigated. It was found that the Vicker's microhardness of as-sprayed SDA is 4.148 GPa and it decreased with the increase in the addition of GO and for SDA-2.0GO, it is 3.305 GPa. The fracture toughness of SDA is 4.86 $\text{MPa m}^{1/2}$ whereas for SDA-2.0GO is 16.85 $\text{MPa m}^{1/2}$. The

fracture toughness has increased whereas the brittleness index has decreased as the weight percentage of GO addition is increased in the SDA-GO composite.

The increase in corrosion resistance is due to the hydrophobic nature of in situ reduced graphene using plasma spray. The plasma spray also results in the thick large-area graphene stacks, which bridge the surface of smaller alumina splats and reduces the number of interfaces. 1.5 and 2.0 wt.% GO reinforced alumina coatings reveal the hydrophobic nature, whereas, bare Alumina surface, 0.5, and 1 wt.% GO showed hydrophilic nature. Not much difference is found in the corrosion rate of 1.5 and 2.0 wt.% GO reinforced alumina nanocomposite coating. A similar trend is observed in the contact angles measurement. Therefore, 1.5 wt.% of GO reinforced alumina coating can be considered as an optimised condition to achieve the highest corrosion resistance. Also, the microhardness has decreased whereas the fracture toughness and the brittleness index has decreased. Thus, plasma-sprayed coatings are a promising way to produce GO-based Al_2O_3 coatings on an industrial scale with superior barrier properties for steel surface protection.

CHAPTER 6

Plasma sprayed ZrO₂-GNP composite coating: Corrosion, mechanical and wetting properties

Outcome of chapter 6

“Enhanced corrosion resistance of atmospheric plasma-sprayed zirconia-GNP composite by graphene oxide nanoplatelets encapsulation”, (**Applied Physics A-Springer**)

CHAPTER 6

Plasma sprayed ZrO₂-GNP composite coating: Corrosion, mechanical and wetting properties

Overview

The unique natural diffusion barrier property of graphene plays a crucial role in protecting the carbon steel substrates from corrosion, particularly using graphene oxide nanoplatelets (GNP)-Zirconia (ZrO₂) composites. In the present work, the atmospheric plasma spraying (APS) technique has been used to coat the spray-dried pristine ZrO₂ and ZrO₂-(0.5, 1.0, 1.5, and 2) wt. % GNP composite on the carbon steel substrate. The retention of GNPs in the coating was confirmed using XRD, Raman Spectroscopy, TEM, FESEM, and EDS techniques. The corrosion properties of the coatings in 3.5wt.% NaCl electrolyte was studied using linear polarisation resistance and electrochemical impedance spectroscopy technique. This reveals the enhanced charge transfer resistance, decreased corrosion current density and corrosion rate of ZrO₂-GNP composite. Further, the corrosion rate of ZrO₂-2 wt.% GNP coating is 130 times lesser than that of plasma-sprayed pristine ZrO₂. Compared to, 0.5, 1.0 and 1.5wt.% GNP added Zirconia coatings, ZrO₂-2 wt.% GNP displayed highest stability upto 14 days in 3.5% NaCl electrolyte. Further, the mechanical and wetting properties of the coatings are discussed.

6.1 Introduction

ZrO₂ is one of the vital ceramic materials known for its excellent mechanical strength, high thermal stability, high resistance to corrosion, and wear (Ahn et al., 1997; Aneziris et al., 2000; Bai et al., 2018; Pei et al., 1996). ZrO₂ also shows good thermal expansion properties and high hardness. Good thermal compatibility with metals among other properties makes ZrO₂ suitable for coatings that shield the underlying metal substrates from corrosion and oxidation. ZrO₂ is available mainly in three different allotropes namely, cubic, monoclinic, and tetragonal (Manivasakan et al., 2011). It is always used in the form of composite for better performance and stability. By the reinforcement of external cations such as Y³⁺, Mg²⁺, Ca²⁺, etc., the ZrO₂ can be stabilized at low

temperatures, resulting in a drastic improvement in its properties (Chung et al., 2016; Pergolesi et al., 2018; Riaz et al., 2012).

There are numerous studies on the reinforcement of materials such as Y_2O_3 , Al_2O_3 , NiCrAlY, Graphene oxide Nanoplatelets (GNPs), (Carbon Nanotubes) CNTs, etc., into the ZrO_2 as mentioned in the literature to improve its physical and chemical properties (Bai et al., 2018; De Aza et al., 2002; Di et al., 2016; Dobbins et al., 2003; Karaoglanli et al., 2011; Keyvani et al., 2010; Liu et al., 2013; Loghman-Estarki et al., 2016; Luo et al., 2016; Lupu et al., 2004; Pi et al., 2017). Nevertheless, GNP has numerous advantages over these materials to reinforce with the ceramics. Due to its excellent barrier properties, GNP also finds use as a protective coating. So far, very few attempts have been made to synthesize ZrO_2 -GNP nanocomposite (Di et al., 2016; Frost et al., 2012; Liu et al., 2013). On the other hand, the ZrO_2 -GNP composites are studied mainly in applications like photocatalysis, adsorption, specific capacitance, hot corrosion resistance, and mechanical properties (Di et al., 2016; Mudila et al., 2016; Pi et al., 2017). Due to promising properties of ZrO_2 -GNP nanocomposite, it can be used as a corrosion-resistant coating as well with good mechanical and wetting properties. Since there are no reports available on corrosion resistance properties of plasma-sprayed ZrO_2 -GNP composites, there is a scope to explore its potential in this field.

6.2 Brief Methodology

In this chapter, an effort has been made to obtain a ZrO_2 -GNP composite coating at different weight percent reinforcement of GNPs in ZrO_2 through APS, with the retention of GNPs in the matrix. The coatings have been characterized for structure, morphology, and corrosion resistance properties. Further, their corrosion behaviour was also studied at different immersion periods to ensure the stability of the coatings. Also, mechanical and wetting properties of the coatings are presented.

6.3 Results and discussions

6.3.1 Dispersion of GO Nanoplatelets (GNP) in the spray-dried Zirconia powder.

Fig. 6.1 shows the FESEM surface morphologies of the spray-dried powders employed for preparing APS coated samples used in corrosion studies. **Fig. 6.1(a)** is the lower magnification image of SDZ showing the doughnut-shaped and spherical shaped powder

particles and **Fig. 6.1(b)** shows the magnified image of the particles with irregular shapes. **Fig. 6.1(c)** is the spray-dried powders of SDZ-1wt.%GNP, which also shows the doughnut-shaped particles with an average size of about 50 μm . **Fig. 6.1** (c and d) clearly show the presence of GNPs in the SDZ-1wt.%GNP.

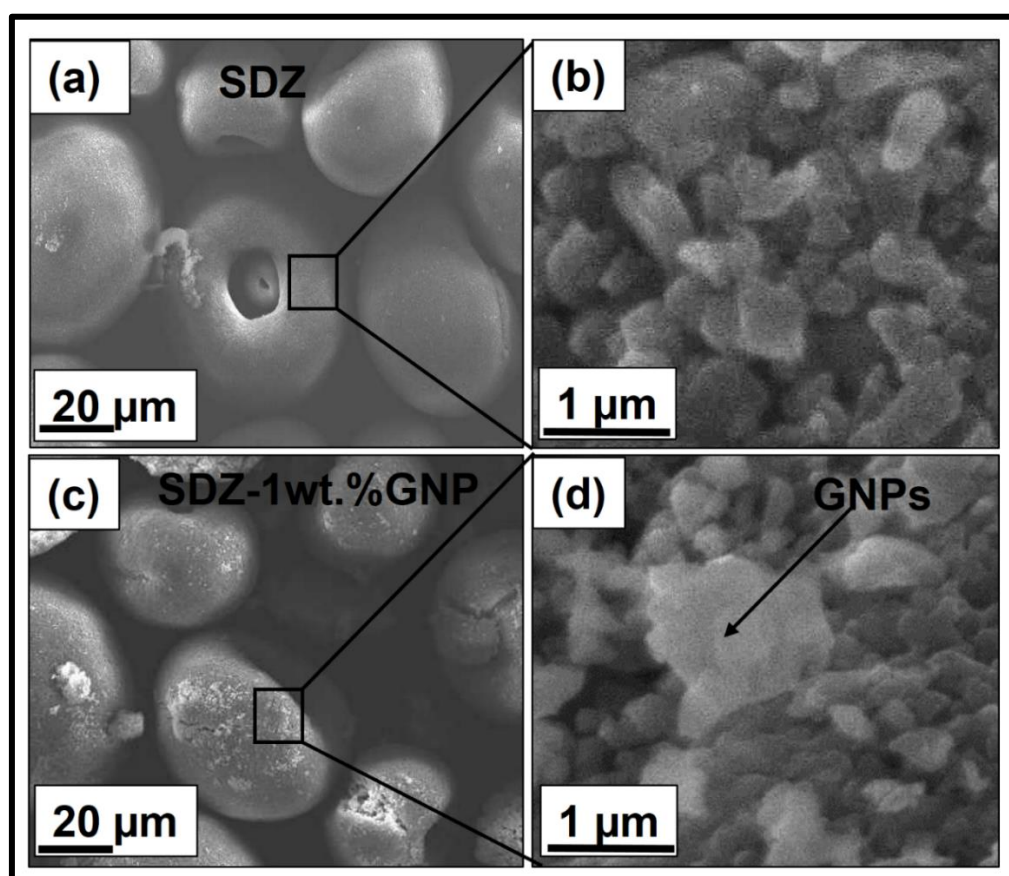


Fig. 6.1 (a) and (b) Surface morphology of the SDZ, (c) and (d) SDZ-1wt.%GNP powder at lower and higher magnification respectively.

The High-Resolution Transmission Electron Microscope (HR-TEM) (model: JEOL 2100 microscope, operating voltage of 200 kV), was used for the confirmation of GNP in the composites. **Fig. 6.2** shows the TEM images of the GNPs, spray-dried powders of SDZ and SDZ-GNP. **Fig. 6.2** (a) and (c) show the GNP and SDZ particles respectively. The GNPs encapsulated in the SDZ-1wt%GNP matrix is seen in **Fig. 6.2(c)**. Similarly, TEM image of SDZ-2wt.%GNPs in **Fig. 6.2(d)** also shows the encapsulation of GNPs which supports the FE-SEM results obtained.

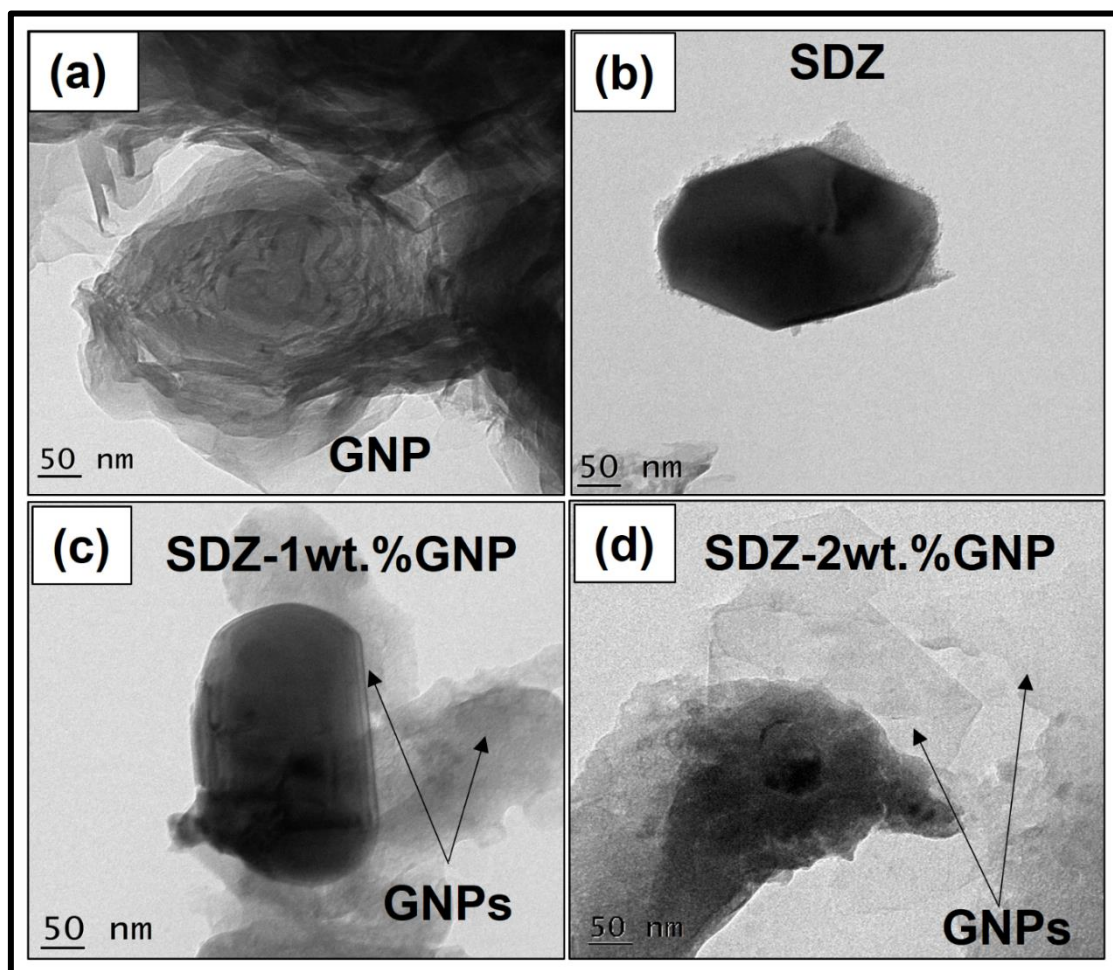


Fig. 6.2 TEM micrographs of (a) GNPs, (b) SDZ, (c) SDZ-1wt.%GNP and (d) SDZ-2wt.%GNP powders.

Structural characterization of the spray-dried powders and coatings was done using powder XRD. **Fig. 6.3** displays the XRD pattern of the SDZ and SDZ-GNP composites. The spray-dried powders show the monoclinic structure as compared with the JCPDS card number 37-1484. A peak at 12° in SDZ-GNP XRD patterns gives evidence for the presence of graphene oxide in the composites and its absence in SDZ.

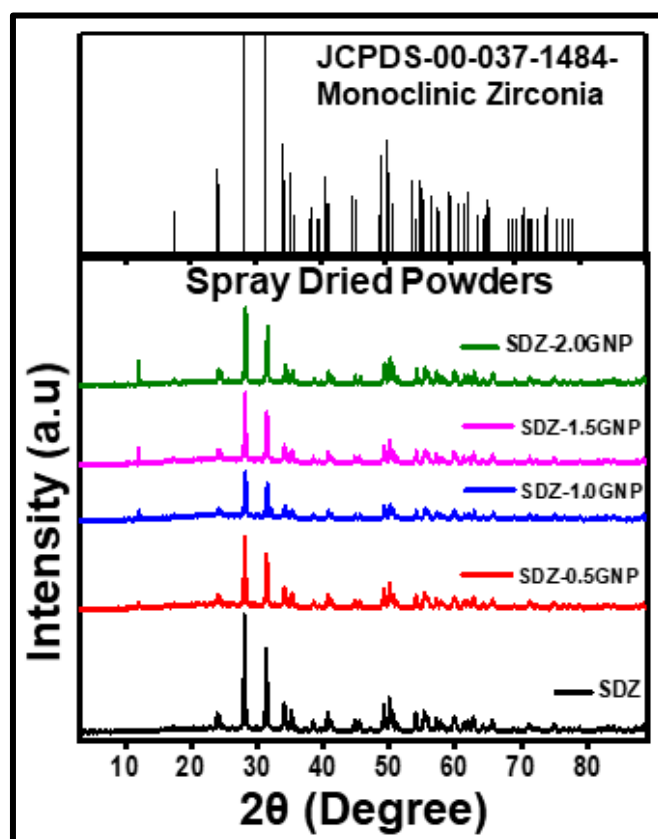


Fig. 6.3 X-Ray Diffractogram of (a) SDZ and SDZ-(0.5, 1.0, 1.5 and 2.0 wt.%)GNP powders

6.3.2 Structural and morphological analysis of the coatings

6.3.2.1 XRD Analysis

Fig. 6.4 displays the XRD pattern of PSZ and PSZ-GNP composites. Two different phases namely monoclinic and tetragonal are observed in PSZ-GNP. For the better understanding of the monoclinic and tetragonal phases present in PSZ and PSZ-GNPs, the crystal structures are drawn with the help of VESTA software and are presented in **Fig. 6.5**. The reflection planes m-(11-1), m-(111), m-(21-1), m-(122), and m-(221) (here m stands for monoclinic) are ascribed to monoclinic ZrO_2 as specified by the JCPDS card number 37-1484 (Gauna et al., 2015). The reflections t-(111), t-(101), and t-(122) (here t stands for tetragonal) are ascribed to the tetragonal phase as specified in the JCPDS card number 50-1089. A characteristic peak at 30° gives evidence for the presence of tetragonal phase (Gauna et al., 2015). It is observed in **Fig. 6.4(a)** that PSZ and PSZ-0.5wt.%GNP show no prominent peak at 17° , however, the peak

becomes prominent at higher wt.%GNP (1,1.5 and 2.0wt.%), indicating the mixed phase of the composites. Also with the increase in GNP wt.% a prominent peak at 12° is observed, which confirms the presence of GNP in the coating as seen in **Fig. 6.4(b)**.

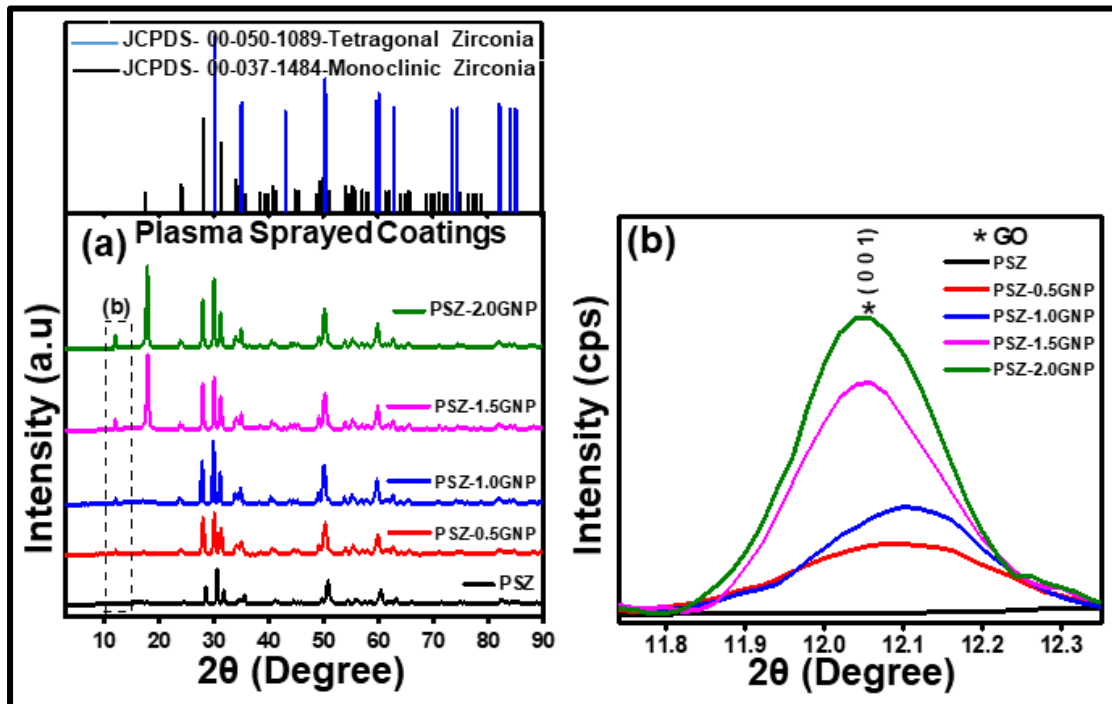


Fig. 6.4 X-Ray Diffractogram of (a) PSZ and PSZ-(0.5, 1.0, 1.5 and 2.0 wt.%)GNP, (b) Highlighted peak at 12° to show retention of GO in the plasma-sprayed coatings.

The monoclinic and tetragonal phases of the zirconia are drawn with the help of VESTA software. The space group P 21/c for monoclinic and P 4/m2 for tetragonal ZrO_2 is used to draw the crystal structures, which is shown in **Fig. 6.5**. The highly desirable tetragonal ZrO_2 is achieved with the reinforcement of GNP to the ZrO_2 crystalline structure. In the course of the reinforcement process, some of the Zr^{4+} ions are substituted in the crystal lattice by GNP. GNP maintains the tetragonal phase of the ZrO_2 at room temperature. This makes PSZ-GNP more stable and suitable to obtain desirable barrier properties.

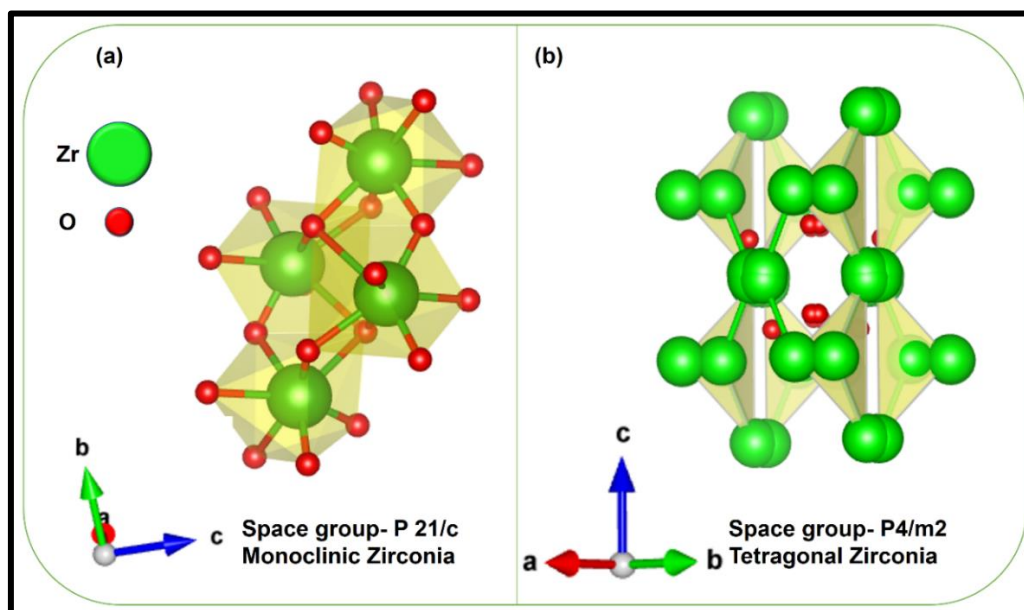


Fig. 6.5 Monoclinic and tetragonal structure ZrO_2 .

6.3.2.2 Raman Analysis

Further, Raman spectroscopy was used to find the retention of GNP in the plasma-sprayed PSZ-GNP composite. **Fig. 6.6** displays the Raman spectra of PSZ and PSZ-(0.5, 1.0, 1.5, and 2.0)wt.%GNP composites. The primary peaks of graphene oxide in G and D modes are observed at 1580 cm^{-1} and 1340 cm^{-1} respectively in the PSZ-GNP. The D-mode is mainly due to lattice defects in sp^2 carbon materials. The G-mode is due to the E_{2g} mode, which arises from C—C bond in sp^2 carbon materials. D'-peak at 1620 cm^{-1} in the case of PSZ-GNPs in **Fig. 6.6**, also overlaps the peak of PSZ, which is due to the randomly distributed surface charges and impurities (Xie et al., 2015). The intensity ratio of D and G peak (I_D/I_G) is often used for enumerating the degree of disorder present in carbon materials (Banhart et al., 2011; Jorio et al., 2010). It is found that the ratio of I_D/I_G to be 1.03 for PSZ-GNP. This increased I_D/I_G ratio of PSZ-GNP composite perhaps stems from the strong coupling between PSZ and GNP matrix (Moon et al., 2010). The increase in the defect density is very obvious in plasma-sprayed coatings due to the high-temperature processing condition (Archanjo et al., 2012).

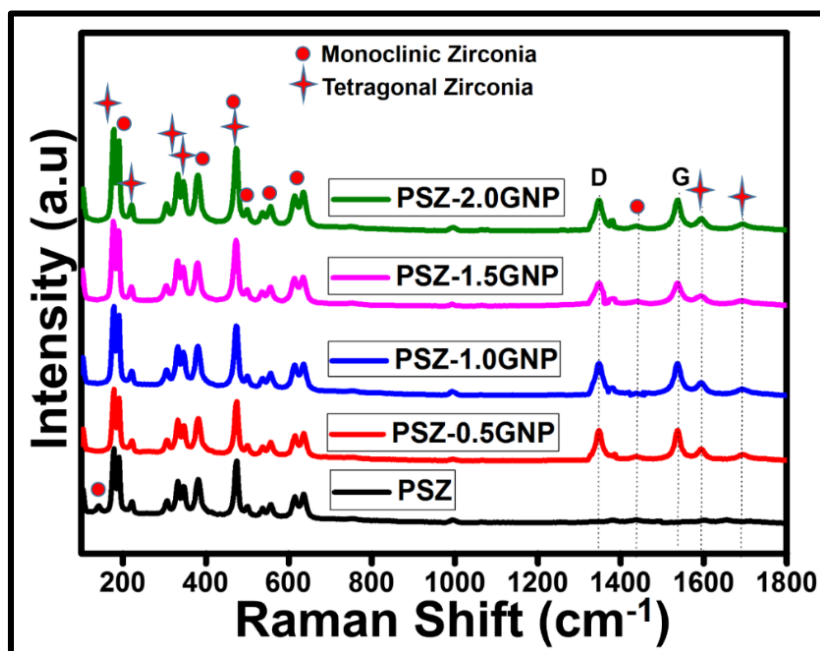


Fig. 6.6 Raman spectra of PSZ and PSZ-(0.5, 1.0, 1.5 and 2.0)wt.%GNP plasma sprayed coatings.

6.3.2.3 FESEM and EDAX Analysis

The FESEM surface morphology and EDS of PSZ, PSZ-1.0wt.%GNP, and PSZ-2.0wt.%GNP are shown in **Fig. 6.7**. The thickness of the coatings is around 500 μm and the cross-section image of PSZ and PSZ-1.0wt.%GNP coatings are given in **Fig. 6.8**. The surface morphology of PSZ splats at lower and higher magnification are shown in **Fig. 6.7** (a) and (b) respectively. The surface morphology of the PSZ-1.0wt.%GNP splats are shown in **Fig. 6.7** (d). The zirconia splats encapsulated by the GNPs can be witnessed from the surface morphology of PSZ-1.0wt.%GNP in **Fig. 6.7**(e). This encapsulation is more prominent in the plasma sprayed (PSZ-2.0wt.%GNP) sample which is shown in **Fig. 6.7**(g) and the overlapping of GNPs between the splats are much clearer in **Fig. 6.7**(h). FESEM images of PSZ and PSZ-GNP do not show any major or micro-cracks. However, we can observe that some amount of inclusions and micropores in the coatings surface, which are very apparent in APS coatings.

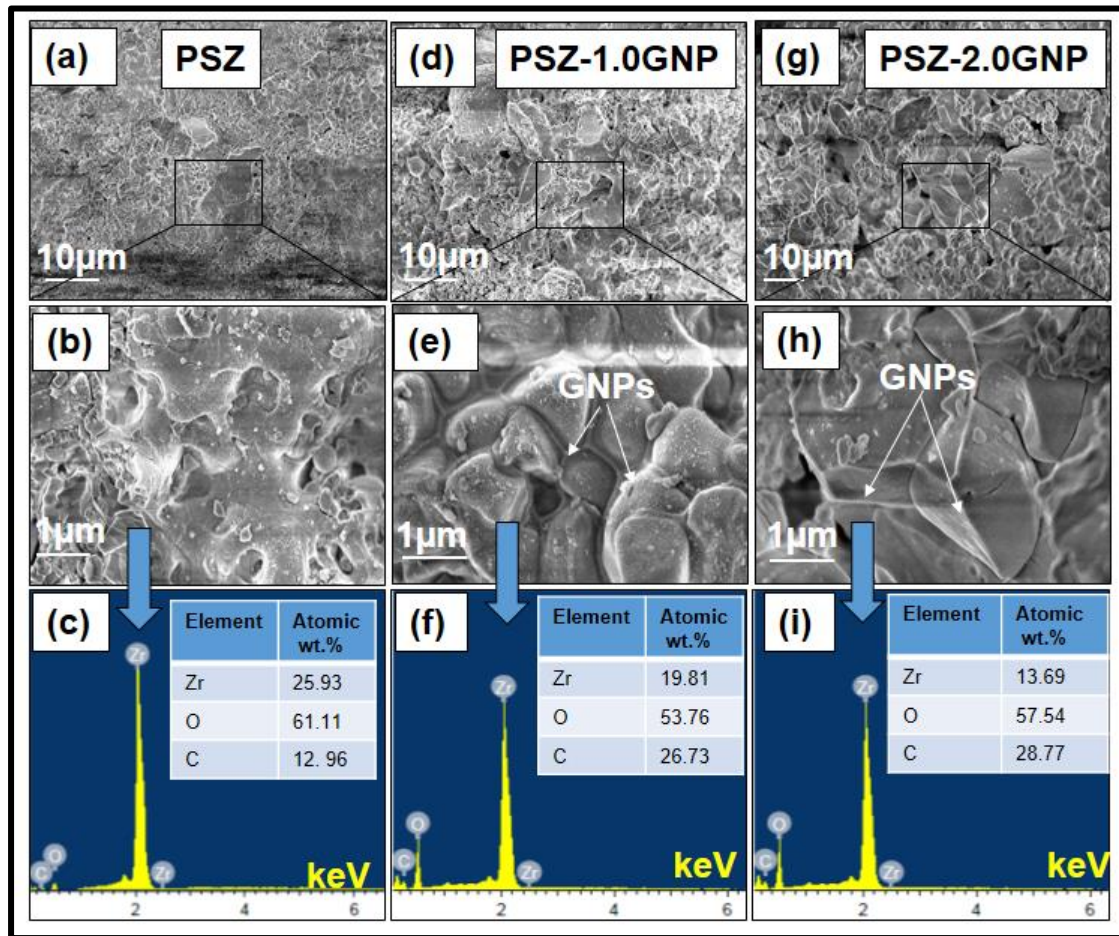


Fig. 6.7 FE-SEM images of (a) PSZ, (b) Higher magnification of PSZ, and (c) EDAX spectra of PSZ, (d) PSZ-1.0GNP, (e) Higher magnification of PSZ-1.0GNP (f) EDAX spectra of PSZ-1.0GNP, (g) PSZ-2.0GNP, (h) Higher magnification of PSZ-2.0GNP and (i) EDAX spectra of PSZ-2.0GNP.

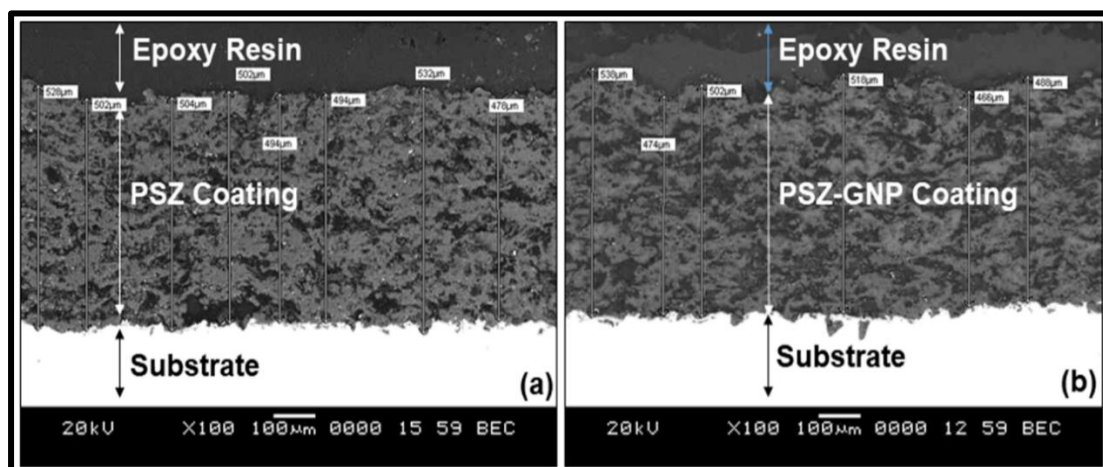


Fig. 6.8 FESEM cross sectional image of (a) PSZ and (b) PSZ-GNP coatings

6.3.3 Electrochemical Corrosion properties of the coatings

6.3.3.1 Linear polarization resistance (LPR) Measurements

Prior to the LPR test, an open circuit potential (OCP) for about 120 mins was run to establish chemical stability. LPR tests were conducted with a linear voltage sweep from -0.5 V to 0.75 V. The corrosion current density (I_{corr}) and corrosion potential (E_{corr}) are obtained by Tafel approximation of LPR curve. The Tafel curves for the PSZ and PSZ-GNP coatings in 3.5 wt% NaCl electrolyte are shown in **Fig. 6.9** and the corresponding electrochemical parameters are listed in **Table 6.1**. The Polarisation resistance (R_p) is calculated using the Stern Geary equation and is tabulated in **Table 6.1**.

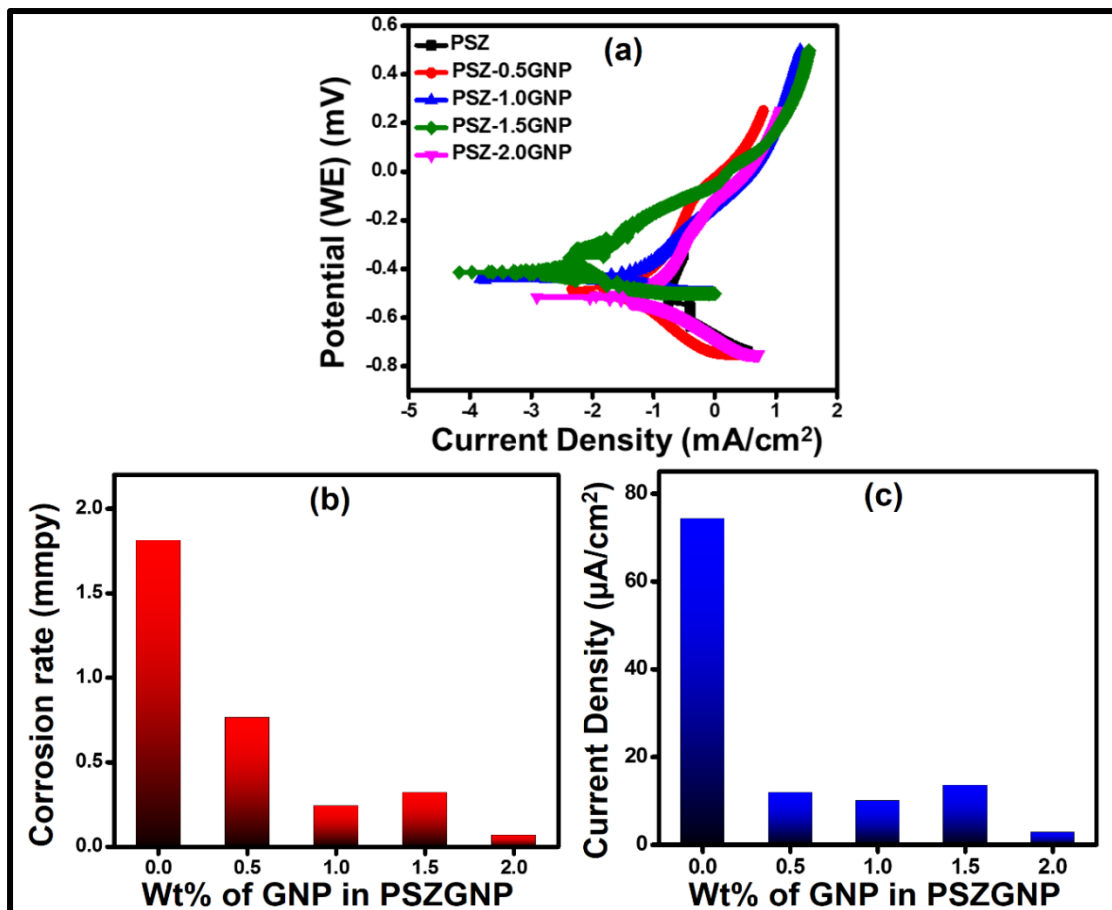


Fig. 6.9 (a) Tafel plot of SDZ and SDZ-(0.5, 1.0, 1.5, and 2.0)wt.%GNP plasma sprayed coatings, (b) Variation of corrosion rate, and (c) Variation of corrosion current density with the composition.

Table 6.1 Electrochemical parameters obtained from Tafel extrapolation of LPR tests.

Sample	E_{corr} (mV)	I_{corr} ($\mu\text{A cm}^{-2}$)	β_a (mV)	β_c (mV)	CR (mmpy)
PSZ	-352.516	74.345	237.27	14.4	1.812
PSZ-0.5GNP	-427.120	11.863	238.8	108.4	0.765
PSZ -1.0GNP	-424.725	10.116	129.1	86.5	0.241
PSZ -1.5GNP	-443.961	13.554	155.1	71.1	0.321
PSZ -2.0GNP	-424.247	2.837	153.6	58.5	0.067

The polarization curves for the PSZ-GNP plasma-sprayed coupons show a drastic reduction in anodic reaction rates, demonstrating that the GNP reinforcement in ZrO_2 protects the substrate which is coated. It also reveals the reduction in the I_{corr} value and the shift of E_{corr} towards a positive direction. This indicates that the PSZ-GNP acts mainly as an ionic barrier (Genorio et al., 2019). The decline in the kinetics of metallic ionization is the main reason for the decrease in the corrosion rate (Qiu et al., 2015). The Tafel curves for the PSZ-GNP coatings present a reduction in the cathodic reaction rate. In this case, the PSZ-GNP surface mainly acts as a corrosion inhibitor.

6.3.3.2 Electrochemical impedance spectroscopy (EIS) Measurements

EIS gives an insight into the barrier properties of anticorrosive coatings. The higher value of impedance at lower frequency is proportional to better anti-corrosion performance, whereas the lower value of impedance over a period of time is an indication of poor anti-corrosion coatings.

Fig. 6.10(a) is the Nyquist plot obtained for the PSZ and the PSZ-GNP composite coatings. In the Nyquist plot, each plasma-sprayed coated samples has a simple semi-circle that differs in radius, which implies the reduced charge-transfer resistance as the wt.% of GNP is increased. The radius of the semi-circles increased with an increase in the wt.% of GNP content, in comparison to PSZ, which indicates 2.wt% GNP reinforcement has got bigger semicircle implying the better anti-corrosion properties. Nyquist curves are fitted to a simple Randle's equivalent circuit as shown in **Fig. 10 (b)**, where, R_s is solution resistance, R_{ct} is charge transfer resistance, and CPE is a constant phase element. An excellent fitting was attained for the experimental data and iterated data using EC-lab software. The values of the circuit elements or fitting parameters are given in **Table 6.2**.

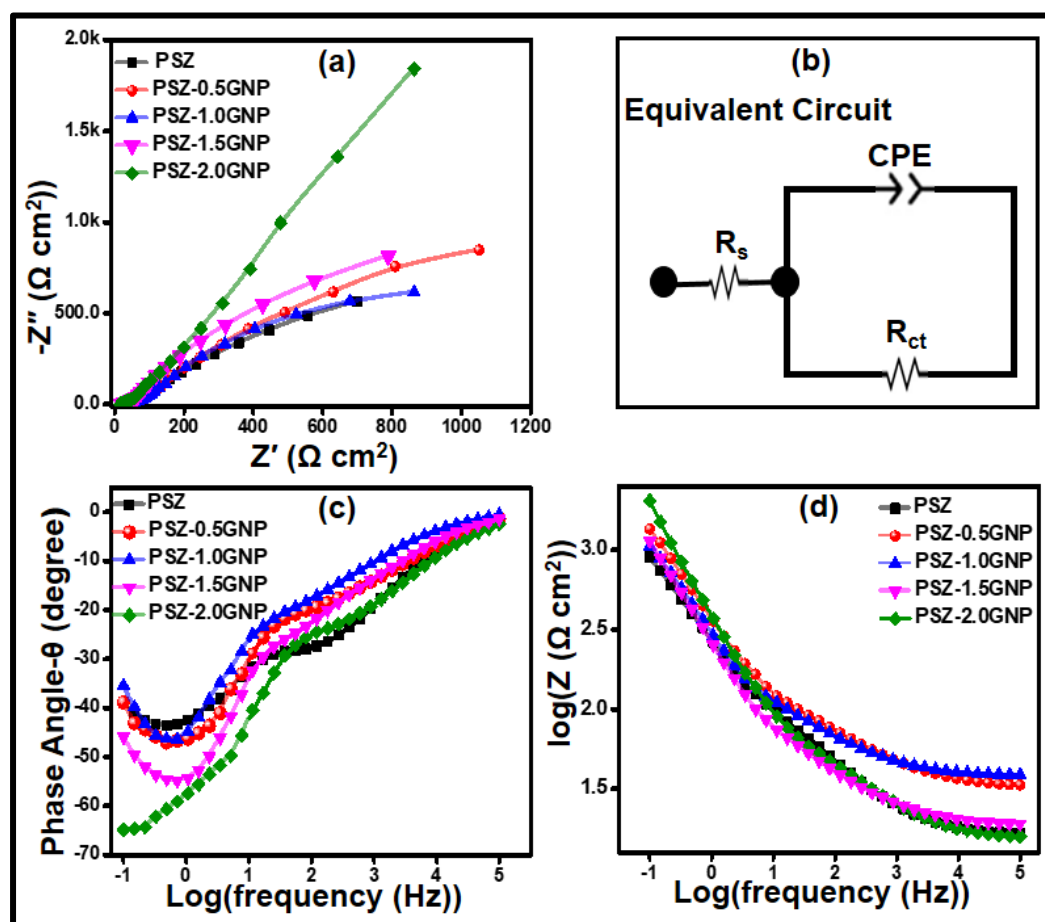


Fig. 6.10 EIS plot of PSZ and PSZ-(0.5, 1.0, 1.5 and 2.0)wt.%GNP plasma sprayed coatings. (a) The Nyquist plot, (b) equivalent circuit (c) Bode Plot, and (d) Impedance plot.

Table 6.2 Electrochemical circuit parameters obtained from EIS fitting.

Sample	$R_s(\Omega)$	α	$CPE \times 10^{-3} (F.s^{-1})$	$R_{ct} (\Omega)$
PSZ	15.6	0.466	1.589	0.191×10^{18}
PSZ-0.5GNP	39.9	0.516	1.375	0.156×10^{18}
PSZ -1.0GNP	35.58	0.508	1.069	0.349×10^{18}
PSZ -1.5GNP	17.54	0.597	0.887	0.848×10^{18}
PSZ -2.0GNP	21.24	0.564	1.352	1.666×10^{18}

Fig. 6.10 (c) and (d) represent the Bode phase angle and the Impedance plots of PSZ and the PSZ@GNP plasma-sprayed samples respectively. In the Bode plot (**Fig. 6.10** (c)),

two-time constants can be observed, which are two local minima having different phase shift for each coating. The phase shift for bare PSZ is minimum whereas for PSZ-2wt.%GNP phase shift is maximum. The phase angle of PSZ is around -45° , but as the percentage of GNP is increased in the zirconia, the phase angle shifted towards the more negative side. Also, the phase angle PSZ-2wt.%GNP approaching -70° is an indication of good corrosion resistance behaviour.

6.3.3.3 Stability by Immersion Test

Further, the effect of time on the corrosion of the coatings are studied. **Fig. 6.11** (a) to (e) shows the impedance spectra of the PSZ and PSZ-(0.5, 1.0, 1.5, and 2.0)wt.%GNP samples immersed for a different duration. Samples are immersed for one hour, one day, 2 days, 5 days, 7 days, and 14 days in the 3.5 wt.%NaCl solution, and their EIS are recorded. After exposure to a saline solution up to 14 days, the difference in the anti-corrosion property of the PSZ and PSZ-GNP samples are more prominent. **Fig. 6.11** (f) shows a better understanding of the EIS Spectra of PSZ and PSZ-(0.5, 1.0, 1.5 and 2.0)wt.%GNP after 14 days of exposure to the electrolyte. The electrochemical circuit parameters obtained after fitting the EIS of 14 days are given **Table 6.3**. The PSZ showed poor anti-corrosion performance after 14 days of immersion. Whereas, the PSZ-2.0wt.%GNP composites showed better stability even after the exposure to the electrolyte for 14 days which is evident from **Fig. 6.11** (f) with bigger semi-circle and is much better than the 0.5, 1.0 and 1.5wt.% GNPs added Zirconia coatings.

Table 6.3 Electrochemical circuit parameters obtained from EIS fitting after 14 days.

Sample	$R_s(\Omega)$	α	CPE $\times 10^{-3}$ (F.s ⁻¹)	R_{ct} (Ω)
PSZ	15.18	0.603	0.893	29
PSZ-0.5GNP	32.76	0.534	0.855	230
PSZ -1.0GNP	40.76	0.597	0.863	4486
PSZ -1.5GNP	16.27	0.580	0.959	3479
PSZ -2.0GNP	19.18	0.532	1.591	15332

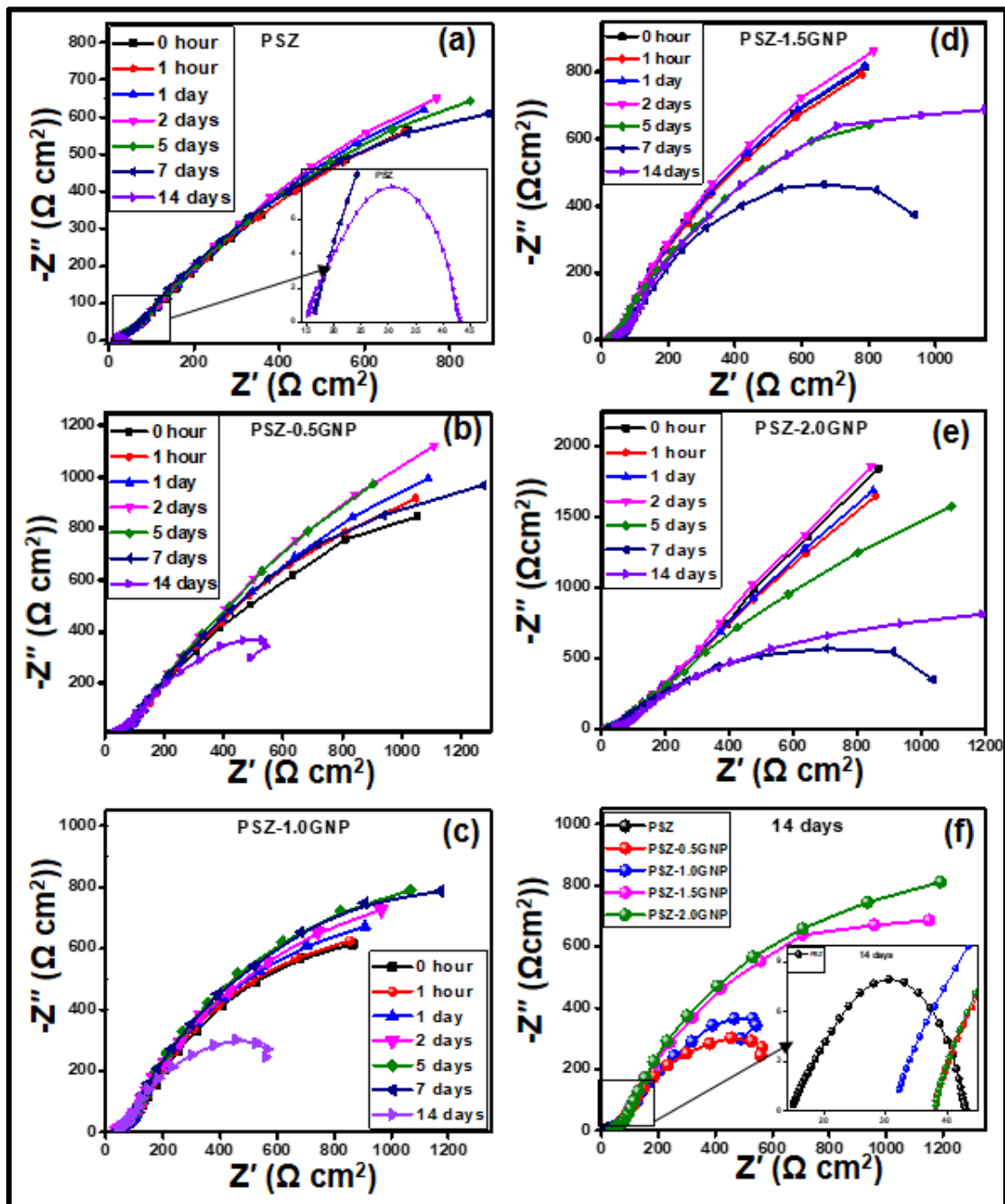


Fig. 6.11 The Nyquist plot of (a)PSZ, (b)PSZ-0.5GNP, (c) PSZ-1.0GNP (d) PSZ-1.5GNP (e) PSZ-2.0GNP immersed for various durations and (f) PSZ-(0.5, 1.0, 1.5 and 2.0)wt.%GNP plasma sprayed coatings immersed for 14 days (the inset in (f) indicates Nyquist plot of PSZ for 14 days).

The anti-corrosion property of the PSZ-GNP can be explained using the following reasons. First, GNP reinforced ZrO_2 coatings being impermeable to the electrolyte, makes the path of ions more tortuous thus, reduces the reaction rate. Because of the impermeability of graphene, the PSZ-GNP acts as an excellent barrier to water, oxygen, and chlorine which are corrosive elements. Second, when GNP is reinforced in the ZrO_2 coating, it can block/reduce the micropores of the PSZ-GNP by wrapping the ZrO_2 particles thereby decreasing the corrosive area. Third, GNP is known for its poor conductivity ($\sim 0.021 \text{ S cm}^{-1}$) which is a good property of any corrosion resistance material (Park and Ruoff, 2009). Due to the lower conductivity of GNPs in comparison to the low carbon steel substrate, it may be hard for the electrons to reach the cathodic site. Finally, the PSZ-GNP coating may be used as a corrosion inhibitor in a corrosive medium for longer periods, since GNP is an sp^2 hybridized carbon atom arrangement in the honeycomb lattice can perhaps give cathodic protection against the corrosion. Hence, we can conclude that the corrosion resistance property of the PSZ-2.wt%GNP the coating has significantly improved due to the reinforcement of GNPs in the zirconia. Also 2 wt.% GNP is an optimum loading because, at higher % o GNP, the coatings started peeling off from the substrate.

6.3.4 Mechanical properties of the coatings

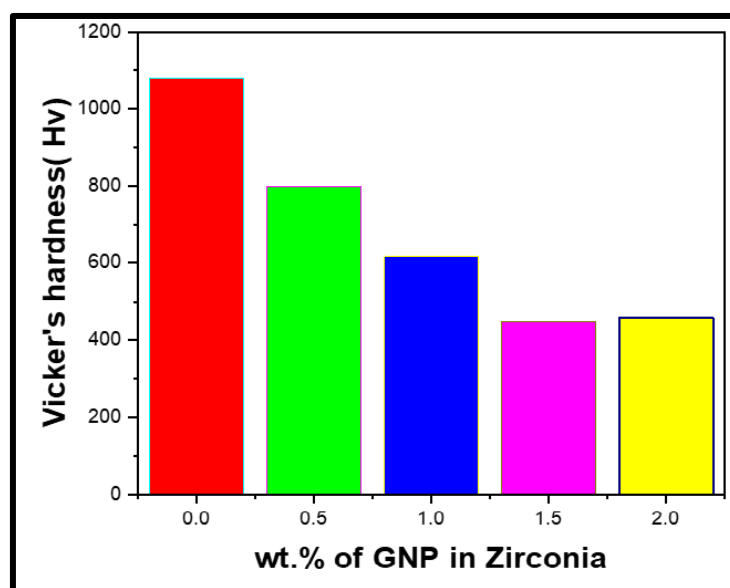


Fig. 6.12 Variation of microhardness of the PSZ and PSZ-(0.5, 1.0, 1.5, and 2.0) wt.% GNP plasma sprayed coatings.

Fig. 6.12 shows the Vickers hardness of PSZ and PSZ-(0.5, 1.0, 1.5, and 2.0) wt.%GNP plasma sprayed coatings. The hardness value of the PSZ is found to be 10.59 ± 0.23 GPa and decreased as the percentage of GNP addition is increased in the PSZ-GNP composites in comparison to PSZ (**Table 6.4**). The hardness is least for the PSZ-2.0GNP composite. The change in the hardness indicates good dispersion of the reinforcing GNP phase in the Zirconia matrix. The GO acts as the lubricant in the PSZ matrix. The increase in the percentage of GNP reinforcement inhibits ceramic grain growth. The homogeneously dispersed graphene oxide in the PSZ-(0.5, 1.0, 1.5 and 2.0) wt.%GNP plasma sprayed coatings has led to a decrease in the hardness due to graphene interface sliding effect and crack bridging of graphene sheets with the zirconia (Su et al., 2016).

Table 6.4. Mechanical properties of PSZ and PSZ-(0.5, 1.0, 1.5, and 2.0) wt.%GNP plasma sprayed coatings.

Sample	Microhardness [GPa]
PSZ	10.59 ± 0.23
PSZ-0.5GNP	7.85 ± 0.17
PSZ-1.0GNP	6.03 ± 0.099
PSZ-1.5GNP	4.39 ± 0.21
PSZ-2.0GNP	4.48 ± 0.25

6.3.5 Wetting properties of the coatings

Contact angle (CA) measurement was used to study the wetting properties of PSZ and PSZ-(0.5, 1.0, 1.5 and 2.0)wt.%GNP coatings. To find out the contact angle of the coatings, 3.5wt.% NaCl is used as the liquid. About 10 μ l of the liquid was dropped on the surface of the coatings. The focused image of the liquid drop was captured and the CA was measured with the help of the contact angle meter. **Fig. 6.13** shows the static contact angles for the plasma spray coating PSZ and PSZ-(0.5, 1.0, 1.5, and 2.0)wt.%GNP coatings. We can witness the increasing trend of the contact angle with an increase in the percentage of GO nanoplatelets in the composite. The CA is tuned from 30° to 114° with GO loading. As evident from **Fig. 6.13**, the PSZ coating has the least CA of 30° , indicating the hydrophilic nature of the PSZ coatings. With the addition of GO nanoplatelets to the zirconia, the hydrophilic nature has disappeared and the coated

surface turns out to be hydrophobic. The CA values of 1.5 and 2 wt.% GO addition are nearer to each other. Larger the CA, lesser is the surface energy, which is due to the weaker adhesion of the 3.5 wt.% NaCl droplet to the coating surface.

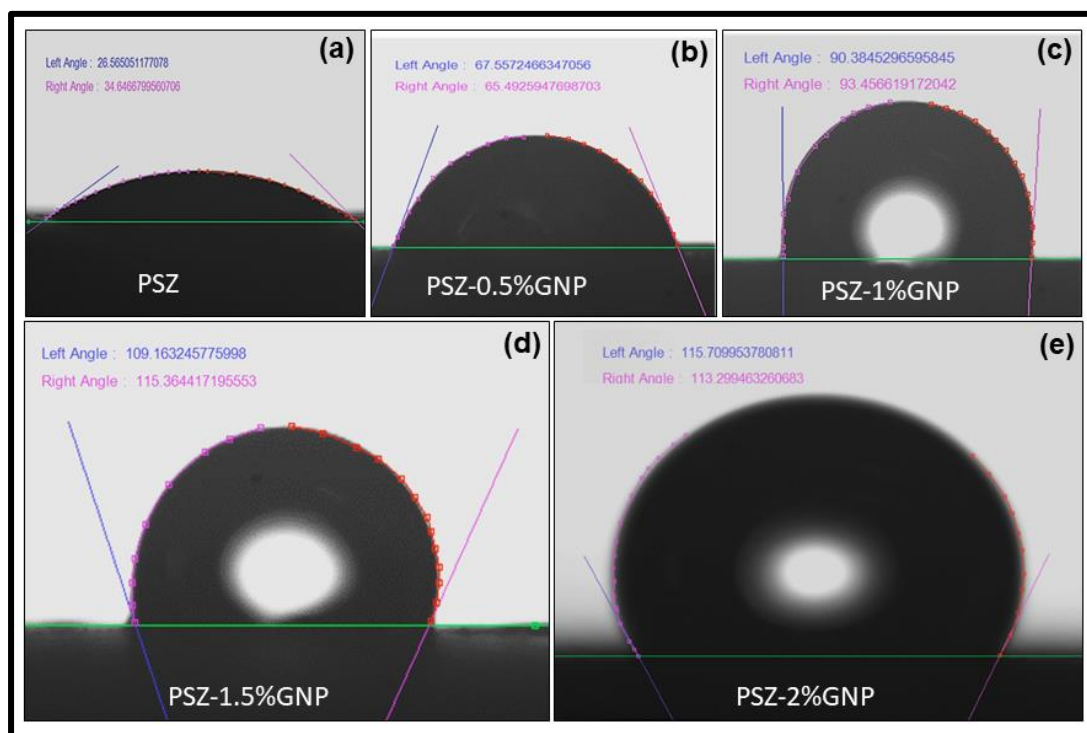


Fig. 6.13. Contact angle measurement of (a)PSZ, (b)PSZ-0.5GNP, (c) PSZ-1.0GNP (d) PSZ-1.5GNP (e) PSZ-2.0GNP.

It can be noted that thin layers of graphene oxide reveal hydrophilicity whereas, thicker coating of graphene oxide consisting of double-layer or more reveals hydrophobicity as reported (Munz et al., 2015). Since, the plasma spray process is a high-temperature process, where melting and re-solidification of PSZ and PSZ-(0.5, 1.0, 1.5, and 2.0)wt.%GNP composite takes place in the coating. Therefore, it is evident that due to plasma spray, not only the graphene oxide is reduced to r-GO but also, forms thick layers, making the coating hydrophobic. Hence, the plasma sprayed coating resulted in a hydrophobic surface with contact angles greater than 90° (Kantesh et al., 2009; Prajitno et al., 2016; Zhang et al., 2017).

6.3.6 Porosity of the coatings

Further, from the BET analysis of PSZ and PSZ-2wt.%GNP coatings, the pore diameters are 10.185 nm and 1.485 nm respectively. The specific surface area of PSZ is $29.609 \text{ m}^2\text{g}^{-1}$ and that of PSZ-2wt.%GNP is $48.607 \text{ m}^2\text{g}^{-1}$. This suggests that the pore size has decreased upon the incorporation of GO nanoplatelets, which implies that the porosity has decreased. The nanopores of PSZ-GNP thus acts as the hydrophobic surface (Yang et al., 2008). This hydrophobic surface acts as a protective layer by preventing the corrosion process. Because, the air trapped in the micro and nano-pores in the graphene oxide surface acts as the water repellent, thereby slowing down the further oxidation and breakdown of the passive film (Aryal et al., 2015; Li et al., 2014; Mohamed et al., 2015; Yu and Tian, 2014). Thus, PSZ-GNP composite coatings act as excellent anticorrosion coatings with low wettability, by turning into a hydrophobic surface.

6.4 Summary and Conclusions

In this work, the homogenous and uniform coatings of ZrO_2 -GNP composite by atmospheric plasma spray technique was deployed. The XRD results revealed that the plasma-sprayed coatings had the mixed-phase namely tetragonal and monoclinic phase of zirconia. A peak at 12° confirmed the retention of the GNPs in PSZ-(0.5, 1.0, 1.5 and 2.0)wt.%GNP composite. The EDS of coatings suggested that a higher percentage of carbon is present in the composites. The Raman spectrum with D and G band in the composites is in agreement with the XRD and EDS analysis. Further, in FE-SEM images, a highly ordered splat arrangement after reinforcement of GNPs was witnessed. Also, an encapsulation of the zirconia splats by the GNPs was clearly seen in FE-SEM images of the composite coatings. This paved the way for the superior corrosion resistance property of the composites being impermeable to 3.5 wt.%NaCl electrolyte. The corrosion inhibiting property of the PSZ-GNP was analyzed by Tafel and EIS plots. The corrosion rate of PSZ-2.0wt.%GNP was found to be 0.067 mmpy whereas the corrosion rate of PSZ was found to be 1.812 mmpy. The Nyquist plot, Bode, and Impedance plot complimented the corrosion result obtained by the Tafel plot. Also, on exposure to 3.5wt.%NaCl solution for 14 days, the PSZ-2.0wt.%GNP had the highest stability in comparison to PSZ and PSZ-(0.5, 1.0, 1.5)wt.% GNP composites.

The PSZ-2.0wt.%GNP has an excellent corrosion resistance property and stability to protect the carbon steel substrate from saline water, the corrosive media. The hydrophobic PSZ-2.0wt.%GNP coatings supported the corrosion results. The nanopores in the composite acted as a water repellent, thereby an anticorrosive hydrophobic coating is obtained. Also, the microhardness of the PSZ-GNP decreased with the addition GNP in the PSZ-GNP composite indicating that the GNP acts as the lubricant.

CHAPTER 7

Summary and Conclusions

CHAPTER 7

Summary and Conclusions

Overview

In this thesis, a small effort has been taken to improve the corrosion, mechanical, and wetting properties of low carbon steel which is largely used as a component in various industries especially in the marine industry. In the present work, the low carbon steel has been coated with a metal alloy Inconel-625, ceramic-metal composite 75NiCr-25Cr₂C₃, ceramic-nanomaterial composites like Alumina-Graphene oxide and Zirconia-Graphene oxide nanoplatelets using thermal spray coating techniques. The various characterization techniques have helped to evaluate the structural, compositional and morphological features of the substrate with and without coatings. The corrosion, mechanical and wetting properties of the coatings are also evaluated and compared with the low carbon steel substrate. A remarkable improvement in these properties is witnessed and they are summarized in this chapter.

7.1. The weld overlay coating of Inconel-625 on the substrate with SS-309Mo as a buffer layer.

The bi-layer weld overlay coating has been deposited on low carbon steel with SS30Mo as the intermediate layer and Inconel-625 as the top layer. This combination has been chosen with ANSYS FE analysis with minimal residual stress. A multilayer coating simulation of alternate skip welding of SS-309Mo weld overlay as a first layer by GTAW and Inconel-625 weld overlay as second final layer by SMAW process for the 6 mm thick substrate preheated to 100°C, was the best model among twelve combinations with 18 MPa surface residual stress. The intermediate layer SS-309Mo helps in preventing the dilution with the top layer.

The top layer ISSCS revealed higher corrosion resistance with a corrosion rate of 1.16×10^{-3} mmpy. Further, a decrease in I_{corr} and an increase in R_p confirms the good corrosion resistance of top layer weld overlay deposition. The CR, I_{corr} and R_p values of ISSCS are comparable with the bulk Inconel 625, which indicates that the weld overlay could achieve the intrinsic corrosion values as that of bulk Inconel-625 with just 2 mm layer

thickness deposition. The immersion studies showed that the ISSCS form a stable anticorrosive film on the substrate.

In addition, the microhardness of the ISSCS was found to be 2.52 ± 0.11 GPa and that of bare Inconel-625 was 2.30 ± 0.07 GPa which indicates a slight increase in its microhardness. Therefore, the Inconel 625 weld overlay with an intermediate layer of SS309Mo can reduce the cost, distortions, increase the corrosion resistance, hardness, and durability of the carbon steel components used in the seawater.

7.2 Nickel Chromium-Chromium Carbide cermet coating on the substrate by the HVOF process.

The spray-dried cermet 25(NiCr)-75Cr₃C₂ (Nickel Chromium-Chromium Carbide) has been coated on a low carbon steel substrate using the HVOF process. The structural and morphological characterization of the coatings by XRD and SEM respectively revealed different phases such as Cr₂O₃, Cr₃C₂, Cr₇C₃, and Ni present in the coating.

The corrosion current density of the coated sample was found to be $6.878 \mu\text{A}/\text{cm}^2$, whereas the current density in the uncoated substrate was $21.091 \mu\text{A}/\text{cm}^2$. The corrosion rate of the coating sample was found to be 5 times less than the substrate. The Nyquist Impedance spectra were used to derive an equivalent circuit to analyze the interaction between the coating and electrolyte. The Bode Impedance plots obtained by EIS for the coating showed a typical passive material capacitive behaviour, indicated by medium to low frequency with phase angle approaching -60° , suggesting that a stable film is formed on the tested material in the electrolyte used.

The microhardness and fracture toughness of the 25%NiCr-75%Cr₂C₃ coating are 1294 ± 37 H_v and 4 ± 0.9 MPa m^{1/2} respectively. The mechanical properties depend on the microstructure of the coating.

A high saltwater contact angle (CA = 98.14°) and a high contact angle hysteresis (CAH- 15°) representing a sticky hydrophobic nature similar to a Rose petal are obtained for our coating. The high advancing contact angle can be attributed to the local trapping offered by the complex microstructures present in the coating, whereas, the low receding angle is due to the sealing of the water droplet within the micro-island between the splats.

7.3 The alumina-graphene oxide coating on the substrate by APS process

Graphene oxide nanoplatelets (0.5, 1.0, 1.5 and 2 wt.%) reinforced in alumina(α - Al_2O_3) nanocomposite coating by atmospheric plasma spray technique is employed for the protection of low carbon steel. The retention of GO nanoplatelets in the composite coating are confirmed by various techniques such as XRD, Raman, FTIR, XPS, FESEM, and TEM. BET analysis revealed that the incorporation of GO has helped in decreasing the pore size and thereby decreasing the porosity of the coating.

The surface corrosion resistance improved nearly six orders of magnitude when coated with 1.5 and 2.0 wt.% GO reinforced alumina nanocomposite, in comparison with bare Al_2O_3 coating. The increase in corrosion resistance is due to the hydrophobic nature of in situ reduced graphene using plasma spray. The plasma spray also results in the thick large-area graphene stacks, which bridge the surface of smaller alumina splats and reduces the number of interfaces. Not much difference is found in the corrosion rate of 1.5 and 2.0 wt.% GO reinforced alumina nanocomposite coating.

In addition, the microhardness of the Alumina-GO composite has decreased whereas the fracture toughness has increased. Also, the contact angles measurement by sessile drop method revealed that 1.5 and 2.0 wt.% GO reinforced alumina coatings are of hydrophobic, whereas, bare Alumina surface, 0.5 and 1 wt.% GO are of hydrophilic. A similar trend has been observed for the corrosion rate as well. Therefore, 1.5 wt.% of GO reinforced alumina coating can be considered as an optimised condition to achieve the highest corrosion resistance since 1.5 and 2.0 wt.% GO reinforced alumina coatings showed similar results.

7.3 The zirconia-graphene oxide coating on the substrate by APS process

Homogenous and uniform coatings of ZrO_2 -GNP composite (PSZ and PSZ-(0.5, 1.0, 1.5, and 2.0)wt.%GNP) by atmospheric plasma spray technique was deployed. The XRD results revealed that the plasma-sprayed coatings had the mixed-phase namely tetragonal and monoclinic phase of zirconia. A peak at 12° confirmed the retention of the GNPs in PSZ-(0.5, 1.0, 1.5 and 2.0)wt.%GNP composite. The EDAX of coatings suggested that a higher percentage of carbon is present in the composites. The Raman spectrum with D and G band in the composites is in agreement with the XRD and EDS analysis. Also, an

encapsulation of the zirconia splats by the GNPs was seen in FESEM images of the composite coatings. This paved the way for the superior corrosion resistance property of the composites being impermeable to 3.5 wt.%NaCl electrolyte.

The corrosion inhibiting property of the PSZ-GNP were analysed by Tafel and EIS plots. The corrosion rate of PSZ-2.0wt.%GNP was found to be 0.067 mmpy whereas the corrosion rate of PSZ was found to be 1.812 mmpy. The Nyquist plot, Bode, and Impedance plot complimented the corrosion result obtained by the Tafel plot. Besides, on exposure to 3.5wt.%NaCl solution for 14 days, the PSZ-2.0wt.%GNP had the highest stability in comparison to PSZ and PSZ-(0.5, 1.0, 1.5)wt.% GNP composites. Thus, PSZ-2.0wt.%GNP has an excellent corrosion resistance property and stability to protect the carbon steel substrate from saline water, the corrosive media.

The microhardness value of the PSZ is found to be 10.59 ± 0.23 GPa and decreased as the percentage of GNP addition is increased in the PSZ-GNP composites in comparison to PSZ. The microhardness of PSZ-1.5GNP and PSZ-2.0GNP are 4.39 ± 0.21 GPa and 4.48 ± 0.25 GPa respectively which are nearly equal.

The contact angle values of 1.5 and 2 wt.% GO addition are nearer to each other. A similar trend has been observed for the corrosion rate and microhardness as well. With the addition of GO nanoplatelets to the zirconia, the hydrophilic nature has found to disappear and the coated surface turns out to be hydrophobic with a contact angle of 115° .

Summary of the results

The corrosion, mechanical and wetting properties of the low carbon steel substrate are improved by a thermal sprayed coating which is summarised in **Table 7.1**. The metal alloy Inconel-625 coating by weld overlay technique, the cermet 25NiCr-75Cr₃C₂ coating using HVOF and Al₂O₃-GO as well as ZrO₂ –GO composite coating by APS process showed a drastic improvement in the properties studied. Thus, choosing appropriate coating material and the coating technique is very much essential to get improved properties, reduction in cost and onsite application of the coatings in an industrial scale.

Table 7.1 Summary of the results

Sample type	Sample	Corrosion properties		Mechanical properties		Wetting Properties
		I_{corr} ($\mu\text{A cm}^{-2}$)	R_{ct} (Ω)	Micro-hardness GPa	Fracture toughness	Contact angle
Substrate	Low carbon steel	169.68 $\times 10^{-6}$	810	1.56 \pm 0.078	1.6 \pm 0.9	67°
Coating materials and method						
1. Metal alloy- WO Process	Inconel-625	1.16 $\times 10^{-6}$	281.25 $\times 10^3$	2.52 \pm 0.11	-	-
2. Metal-ceramic composite- HVOF Process	75NiCr- 25Cr ₂ C ₃	0.10	100 $\times 10^3$	12.69 \pm 0.362	4 \pm 1	98°
3. Ceramic- Nanomaterial composite-APS Process	Al ₂ O ₃	47.306	128.6	4.19	4.86	36°
	Al ₂ O ₃ -0.5GO	8.463	1530	3.89	12.06	67°
	Al ₂ O ₃ -1.0GO	9.0 $\times 10^{-3}$	19802	3.77	13.75	86°
	Al ₂ O ₃ -1.5GO	1.5 $\times 10^{-5}$	31757	3.77	15.85	114°
	Al ₂ O ₃ -2.0GO	1.0 $\times 10^{-5}$	25809	3.31	16.85	127°
	ZrO ₂	74.345	0.191 $\times 10^{18}$	10.59 \pm 0.23	-	30°
	ZrO ₂ -0.5GO	11.863	0.156 $\times 10^{18}$	7.85 \pm 0.17	-	66°
	ZrO ₂ -1.0GO	10.116	0.349 $\times 10^{18}$	6.03 \pm 0.099	-	91°
ZrO ₂ -1.5GO	13.554	0.848 $\times 10^{18}$	4.39 \pm 0.21	-	113°	
ZrO ₂ -2.0GO	2.837	1.666 $\times 10^{18}$	4.48 \pm 0.25	-	114°	

Different types of coatings are exhibited in this thesis work including different types of coating methods and materials. Based on the result obtained, the Inconel -625 shows highest corrosion resistance property, using weld overlay coating technique, it is very easy for onsite application like ship hulls, turbine blades in sea shore applications. Also, using advanced materials such as Alumina-1.5 wt% GO and Zirconia-1.5 wt%GO

coatings, the corrosion, mechanical properties are improved in comparison to alumina and zirconia coatings. These coatings can be done in large scale, because the synthesis method used for coating materials are already established method.

Scope for the future work

1. The residual stresses in the coatings can be studied theoretically using ANSYS simulation and experimentally using the XRD method or other methods. This can be a comparative study of residual stresses.
2. Apart from Alumina and Zirconia, other ceramics can be made composite with carbon nanomaterials and studied their properties in detail.
3. The wetting properties of the ceramic-nanomaterial composite studied by tuning with different compositions, additives, and polishing techniques to get superhydrophobic coatings.

References

Abioye TE, McCartney DG, Clare AT. (2015). Laser cladding of Inconel 625 wire for corrosion protection. *Journal of Materials Processing Technology* 217: 232-40

Ahn H-S, Kim J-Y and Lim D-S (1997) Tribological behaviour of plasma-sprayed zirconia coatings. *Wear* **203-204**:77-87.

Al-Fozan SA, Malik AU. (2008). Effect of seawater level on corrosion behavior of different alloys. *Desalination* 228: 61-67

Al Zoubi W and Ko YG (2018) Enhanced Corrosion Protection Performance by Organic-Inorganic Materials Containing Thiocarbonyl Compounds. *Scientific Reports* **8**:10925.

Amudha A, Shashikala HD, Asiq Rahman OS, Keshri AK and Nagaraja HS (2019) Effect of graphene oxide loading on plasma sprayed alumina-graphene oxide composites for improved anticorrosive and hydrophobic surface. *Surface Topography: Metrology and Properties* **7**:024003.

Amudha A, Nagaraja HS and Shashikala HD (2019) Finite element analysis of thermal residual stresses in SS-309Mo and Inconel-625 multilayer weld deposition on low carbon steel. *International Journal of Fatigue* **127**:338-344.

Amudha A, Nagaraja HS, Shashikala HD. 2020. Plasma-sprayed graphene oxide reinforced alumina composite coatings on low carbon steel with improved fracture toughness, brittleness index, and microhardness. *Materials Today: Proceedings*

Amudha A, Shashikala HD, Nagaraja HS. 2019. Corrosion protection of low-cost carbon steel with SS-309Mo and Inconel-625 bimetallic weld overlay. *Materials Research Express* **6**: 046523

Aneziris CG, Pfaff EM and Maier HR (2000) Corrosion mechanisms of low porosity ZrO₂ based materials during near net shape steel casting. *Journal of the European Ceramic Society* **20**:159-168.

Archanjo BS, Barboza APM, Neves BRA, Malard LM, Ferreira EHM, Brant JC, Alves ES, Plentz F, Carozo V, Fragneaud B, Maciel IO, Almeida CM, Jorio A and Achete CA (2012)

The use of a Ga⁺focused ion beam to modify graphene for device applications. *Nanotechnology* **23**:255305.

Armugam A, Shashikala HD and Hosakoppa N (2018) Corrosion Behaviour and Characterization of Thermal Sprayed Coating of Nickel Chromium Cermet on Low Carbon Steel. *Materials Today: Proceedings* **5**:16100-16105.

Aryal P, Sansom MSP and Tucker SJ (2015) Hydrophobic Gating in Ion Channels. *Journal of Molecular Biology* **427**:121-130.

Bai M, Maher H, Pala Z and Hussain T (2018) Microstructure and phase stability of suspension high velocity oxy-fuel sprayed yttria stabilised zirconia coatings from aqueous and ethanol based suspensions. *Journal of the European Ceramic Society* **38**:1878-1887.

Banhart F, Kotakoski J and Krasheninnikov AV (2011) Structural Defects in Graphene. *ACS Nano* **5**:26-41.

Atroshenko A, Vairis A, Bichkov V, Nikiforov R. (2014). ANSYS Simulation of Residual Strains in Butt-welded Joints. *Journal of Engineering Science and Technology Review* **7**: 9-11

Bagotia N, Choudhary V, Sharma DK. (2018). Superior electrical, mechanical and electromagnetic interference shielding properties of polycarbonate/ethylene-methyl acrylate-in situ reduced graphene oxide nanocomposites. *Journal of Materials Science* **53**: 16047-61

Balan AV, Shivasankaran N, Magibalan S. (2018). Optimization of cladding parameters for resisting corrosion on low carbon steels using simulated annealing algorithm. *Materials Research Express* **5**: 046527

Barai A, Uddin K, Widanage WD, McGordon A, Jennings P. (2018). A study of the influence of measurement timescale on internal resistance characterisation methodologies for lithium-ion cells. *Scientific Reports* **8**: 21

Bhandari J, Khan F, Abbassi R, Garaniya V, Ojeda R. (2015). Modelling of pitting corrosion in marine and offshore steel structures – A technical review. *Journal of Loss Prevention in the Process Industries* **37**: 39-62

Bobzin K, Kopp N, Warda T, Öte M. (2012). Determination of the Effective Properties of Thermal Spray Coatings Using 2D and 3D Models. *Journal of Thermal Spray Technology* 21: 1269-77

Česánek Z, Houdková Š, Lukáč F. (2018). High-temperature corrosion behavior of selected thermally sprayed coatings in corrosive aggressive environment. *Materials Research Express* 6: 016426

Chen L, Bai S-L, Ge Y-Y, Wang Q-Y. (2018). Erosion-corrosion behavior and electrochemical performance of Hastelloy C22 coatings under impingement. *Applied Surface Science* 456: 985-98

Chung P-T, Chiou S-H, Tseng C-Y and Chiang AS-T (2016) Preparation and Evaluation of a Zirconia/Oligosiloxane Nanocomposite for LED Encapsulation. *ACS Applied Materials & Interfaces* 8:9986-9993.

Corres H, Caldentey A, Petschke T. (1999). Pren Chapter 7-Serviceability limit states.

Cygan T, Wozniak J, Kostecki M, Petrus M, Jastrzębska A (2017). Mechanical properties of graphene oxide reinforced alumina matrix composites. *Ceramics International* 43: 6180-86

Dai Q, Ye X-X, Ai H, Chen S, Jiang L, et al. (2018). Corrosion of Incoloy 800H alloys with nickel cladding in FLiNaK salts at 850 °C. *Corrosion Science* 133: 349-57

De Aza AH, Chevalier J, Fantozzi G, Schehl M and Torrecillas R (2002). Crack growth resistance of alumina, zirconia and zirconia toughened alumina ceramics for joint prostheses. *Biomaterials* 23:937-945.

Di H, Yu Z, Ma Y, Zhang C, Li F, Lv L, Pan Y, Shi H and He Y (2016) Corrosion-resistant hybrid coatings based on graphene oxide–zirconia dioxide/epoxy system. *Journal of the Taiwan Institute of Chemical Engineers* 67:511-520.

Ding J-H, Zhao H-R, Zheng Y, Zhao X, Yu H-B. (2018). A long-term anticorrosive coating through graphene passivation. *Carbon* 138: 197-206

Dobbins TA, Knight R and Mayo MJ (2003). HVOF thermal spray deposited Y₂O₃-stabilized ZrO₂ coatings for thermal barrier applications. *Journal of Thermal Spray Technology* **12**:214-225.

Drelich J, Boinovich L, Chibowski E, Volpe C, Hołysz L (2019). Contact Angles: History of Over 200 Years of Open Questions. *Surface Innovations*: 1-25

Dwivedi D, Lepková K, Becker T. (2017). Carbon steel corrosion: a review of key surface properties and characterization methods. *RSC Advances* **7**: 4580-610

Frankel GS, Sridhar N. (2008). Understanding localized corrosion. *Materials Today* **11**: 38-44

Frost R, Jönsson GE, Chakarov D, Svedhem S and Kasemo B (2012) Graphene Oxide and Lipid Membranes: Interactions and Nanocomposite Structures. *Nano Letters* **12**:3356-3362.

Gauna M, Conconi S, Gómez S, Suarez G, Aglietti E and Rendtorff N (2015) Monoclinic-tetragonal zirconia quantification of commercial nanopowder mixtures by XRD and DTA. *Ceramics Silikaty* **59**:318-325.

Gateman SM, Stephens LI, Perry SC, Lacasse R, Schulz R and Mauzeroll J (2018) The role of titanium in the initiation of localized corrosion of stainless steel 444. *npj Materials Degradation* **2**:5.

Geim AK, Novoselov KS. (2007). The rise of graphene. *Nature Materials* **6**: 183

Genorio B, Harrison KL, Connell JG, Dražić G, Zavadil KR, Markovic NM and Strmcnik D (2019) Tuning the Selectivity and Activity of Electrochemical Interfaces with Defective Graphene Oxide and Reduced Graphene Oxide. *ACS Applied Materials & Interfaces* **11**:34517-34525.

Ghosh S, Ramgopal T. (2005). Effect of Chloride and Phosphoric Acid on the Corrosion of Alloy C-276, UNS N08028, and UNS N08367. *NACE-93110929* **61**: 11.

Gong Y, Li D, Fu Q, Pan C. (2015). Influence of graphene microstructures on electrochemical performance for supercapacitors. *Progress in Natural Science: Materials International* 25: 379-85

Goyal R, Sidhu BS, Chawla V. (2017). Characterization of plasma-sprayed carbon nanotube (CNT)-reinforced alumina coatings on ASME-SA213-T11 boiler tube steel. *The International Journal of Advanced Manufacturing Technology* 92: 3225-35

Feng L, Zhang Y, Xi J, Zhu Y, Wang N, Xia F and Jiang L (2008) Petal Effect: A Superhydrophobic State with High Adhesive Force. *Langmuir* 24:4114-4119.

Hashemzadeh M, Chen BQ, Guedes Soares C. (2015). Numerical and experimental study on butt weld with dissimilar thickness of thin stainless steel plate. *The International Journal of Advanced Manufacturing Technology* 78: 319-30

Hayden SC, Chisholm C, Grudt RO, Aguiar JA, Mook WM, et al. (2019). Localized corrosion of low-carbon steel at the nanoscale. *npj Materials Degradation* 3: 17

He X, Song RG, Kong DJ. (2018). Microstructure and corrosion behaviour of laser-cladding Al-Ni-TiC-CeO₂ composite coatings on S355 offshore steel. *Journal of Alloys and Compounds*

Hong T, Sun YH and Jepson WP (2002) Study on corrosion inhibitor in large pipelines under multiphase flow using EIS. *Corrosion Science* 44:101-112.

Jinlong L, Tongxiang L, Chen W and Wenli G (2015) Investigation of passive films formed on the surface of alloy 690 in borate buffer solution. *Journal of Nuclear Materials* 465:418-423.

Jorio A, Martins Ferreira E, Moutinho M, Stavale F, Achete C and Capaz R (2010) Measuring disorder in graphene with the G and D bands. *physica status solidi (b)* 247:2980-2982.

Jüttner K (1990) Electrochemical impedance spectroscopy (EIS) of corrosion processes on inhomogeneous surfaces. *Electrochimica Acta* 35:1501-1508.

Kang K, Kawahito Y, Gao M, Zeng X. (2017). Effects of laser-arc distance on corrosion behavior of single-pass hybrid welded stainless clad steel plate. *Materials & Design* 123: 80-88

Kantesh B, Ruben Galiano B, Debrupa L, Arvind A. (2009). The hydrophobicity of a lotus leaf: a nanomechanical and computational approach. *Nanotechnology* 20: 305707

Kartsonakis IA, Dragatogiannis DA, Koumoulos EP, Karantonis A, Charitidis CA. (2016). Corrosion behaviour of dissimilar friction stir welded aluminium alloys reinforced with nanoadditives. *Materials & Design* 102: 56-67

K B, Sridharan K, K M A, Lim HN and Nagaraja HS (2016) Microwave assisted growth of stannous ferrite microcubes as electrodes for potentiometric nonenzymatic H₂O₂ sensor and supercapacitor applications. *Electrochimica Acta* 217:139-149.

Kellici S, Acord J, Power N, Morgan D, Coppo P, et al. (2017). *Rapid synthesis of graphene quantum dots using a continuous hydrothermal flow synthesis approach*. 14716 pp.

Keshri AK, Lahiri D, Agarwal A. (2011). Carbon nanotubes improve the adhesion strength of a ceramic splat to the steel substrate. *Carbon* 49: 4340-47.

Keshri AK, Huang J, Singh V, Choi W, Seal S, Agarwal A. (2010). Synthesis of aluminum oxide coating with carbon nanotube reinforcement produced by chemical vapor deposition for improved fracture and wear resistance. *Carbon* 48: 431-42.

Keyvani A, Saremi M and Heydarzadeh Sohi M (2010) Microstructural stability of zirconia–alumina composite coatings during hot corrosion test at 1050°C. *Journal of Alloys and Compounds* 506:103-108.

Kim G, Choi H, Han C, Uhm S, Lee C. (2005). Characterization of atmospheric plasma spray NiCr–Cr₂O₃–Ag–CaF₂/BaF₂ coatings. *Surface and Coatings Technology* 195: 107-15.

Kim HJ, Lee S-M, Oh Y-S, Yang Y-H, Lim YS, et al. (2014). Unoxidized Graphene/Alumina Nanocomposite: Fracture- and Wear-Resistance Effects of Graphene on Alumina Matrix. *Scientific Reports* 4: 5176.

Kim JS, Park YIL, Lee HW. (2015). Effects of heat input on the pitting resistance of Inconel 625 welds by overlay welding. *Metals and Materials International* 21: 350-55.

King AAK, Davies BR, Noorbehesht N, Newman P, Church TL, et al. (2016a). A New Raman Metric for the Characterisation of Graphene oxide and its Derivatives. *Scientific Reports* 6: 19491.

Kumar S, Mudgal D, Singh S and Prakash S (2013) Cyclic oxidation behavior of bare and Cr₃C₂-25 (NiCr) coated super alloy at elevated temperature. *Adv Mater Lett* 4:754-761.

Kumari S, Tiyyagura HR, Douglas TEL, Mohammed EAA, Adriaens A, Fuchs-Godec R, Mohan MK and Skirtach AG (2018) ANN prediction of corrosion behaviour of uncoated and biopolymers coated cp-Titanium substrates. *Materials & Design* 157:35-51.

Levy A, Miriyev A, Elliott A, Babu SS, Frage N. (2017). Additive manufacturing of complex-shaped graded TiC/steel composites. *Materials & Design* 118: 198-203.

Li J, Yang L, Ma H, Jiang K, Chang C, et al. 2016. Improved corrosion resistance of novel Fe-based amorphous alloys. *Materials & Design* 95: 225-30.

Li M, Luo S, Wu P and Shen J (2005) Photocathodic protection effect of TiO₂ films for carbon steel in 3% NaCl solutions. *Electrochimica Acta* 50:3401-3406.

Li S, Wei Q, Shi Y, Zhu Z, Zhang D. (2015). Microstructure Characteristics of Inconel 625 Superalloy Manufactured by Selective Laser Melting. *Journal of Materials Science & Technology* 31: 946-52.

Li Y, Yang Z, Qiu H, Dai Y, Zheng Q, Li J and Yang J (2014) Self-aligned graphene as anticorrosive barrier in waterborne polyurethane composite coatings. *Journal of Materials Chemistry A* 2:14139-14145.

Li Y. (2001). Corrosion behaviour of hot dip zinc and zinc-aluminium coatings on steel in seawater. *Bulletin of Materials Science* 24: 355-60.

Liu C, Sun Y, Wen M, He T, Yu J. (2020). Effect of Cr addition on microstructure and welding solidification cracking susceptibility of Co-Al-W based superalloys. *Journal of Manufacturing Processes* 56: 820-29.

Liu J, Meng X, Hu Y, Geng D, Banis MN, Cai M, Li R and Sun X (2013) Controlled synthesis of Zirconium Oxide on graphene nanosheets by atomic layer deposition and its growth mechanism. *Carbon* **52**:74-82.

Liu Z, Gao X, Li J, Bai X. (2016). Corrosion behavior of low alloy pipeline steel in saline solution saturated with supercritical carbon dioxide. *Journal of Wuhan University of Technology-Mater. Sci. Ed.* 31: 654-61.

Loghman-Estarki MR, Shoja Razavi R, Edris H, Bakhshi SR, Nejati M and Jamali H (2016) Comparison of hot corrosion behavior of nanostructured ScYSZ and YSZ thermal barrier coatings. *Ceramics International* **42**:7432-7439.

Luo J, Luo X, Hu C, Crittenden JC and Qu J (2016) Zirconia Embedded in Carbon Nanowires via Electrospinning for Efficient Arsenic Removal from Water Combined with DFT Studies. *ACS Applied Materials & Interfaces* **8**:18912-18921.

Lupo F, Kamalakaran R, Scheu C, Grobert N and Rühle M (2004) Microstructural investigations on zirconium oxide-carbon nanotube composites synthesized by hydrothermal crystallization. *Carbon* **42**:1995-1999.

Makkonen L. (2016). Young's equation revisited. *Journal of Physics: Condensed Matter* 28: 135001.

Manivasakan P, Venkatachalam R, Ranjan Rauta P, Bandhu Sahu B and Panda B (2011) Synthesis of Monoclinic and Cubic ZrO₂ Nanoparticles from Zircon. *Journal of the American Ceramic Society* **94**:1410-1420.

Mansfeld F (1990) Electrochemical impedance spectroscopy (EIS) as a new tool for investigating methods of corrosion protection. *Electrochimica Acta* **35**:1533-1544.

Matthews S, Hyland M, James B. 2003. Microhardness variation in relation to carbide development in heat treated Cr₃C₂-NiCr thermal spray coatings. *Acta Materialia* 51: 4267-77.

Mayavan S, Siva T and Sathiyarayanan S (2013) Graphene ink as a corrosion inhibiting blanket for iron in an aggressive chloride environment. *RSC Advances* **3**:24868-24871.

Meng G, Li Y, Shao Y, Zhang T, Wang Y, Wang F, Cheng X, Dong C and Li X (2016) Effect of Microstructures on Corrosion Behavior of Nickel Coatings: (II) Competitive Effect of Grain Size and Twins Density on Corrosion Behavior. *Journal of Materials Science & Technology* **32**:465-469.

Mohamed AMA, Abdullah AM and Younan NA (2015) Corrosion behavior of superhydrophobic surfaces: A review. *Arabian Journal of Chemistry* **8**:749-765.

Mohammadi Zahrani E and Alfantazi AM (2012) Molten salt induced corrosion of Inconel 625 superalloy in $\text{PbSO}_4\text{-Pb}_3\text{O}_4\text{-PbCl}_2\text{-Fe}_2\text{O}_3\text{-ZnO}$ environment. *Corrosion Science* **65**:340-359.

Moon IK, Lee J, Ruoff RS and Lee H (2010) Reduced graphene oxide by chemical graphitization. *Nature Communications* **1**:73.

Moradi M, Ketabchi M. (2015). An Experimental Study of Microstructure and Mechanical Behavior of Alloy 625 Weld Overlay Deposited On ASTM A516 Grade 70. *Indian Journal of Science and Technology* **8**

Mudila H, Rana S and Zaidi MGH (2016) Electrochemical performance of zirconia/graphene oxide nanocomposites cathode designed for high power density supercapacitor. *Journal of Analytical Science and Technology* **7**:3.

Munz M, Giusca CE, Myers-Ward RL, Gaskill DK, Kazakova O. (2015). Thickness-Dependent Hydrophobicity of Epitaxial Graphene. *ACS Nano* **9**: 8401-11

Murray JW, Rance GA, Xu F, Hussain T. 2018. Alumina-graphene nanocomposite coatings fabricated by suspension high velocity oxy-fuel thermal spraying for ultra-low-wear. *Journal of the European Ceramic Society* **38**: 1819-28

Nagy G, Kerner Z, Schiller R. 2007. Interpretation of EIS data on passive steel surfaces in aqueous sulfuric acid solution in terms of carrier migration and recombination. *Electrochimica Acta* **53**: 1737-42

Nguyen Van T, Nguyen Tuan A, Le Thu Q and Pham Thi H (2019) Influence of plasma spraying parameters on microstructure and corrosion resistance of $\text{Cr}_3\text{C}_2\text{-25NiCr}$ cermet carbide coating. *Anti-Corrosion Methods and Materials* **66**:336-342

Okano S, Kobayashi S, Kimura K, Ando A, Yamada E, et al. 2016. Experimental and numerical investigation on generation characteristics of welding deformation in compressor impeller. *Materials & Design* 101: 160-69

Paparazzo E. 1986. XPS analysis of iron aluminum oxide systems. *Applied Surface Science* 25: 1-12

Pareek A, Shanthi Sravan J, Venkata Mohan S. 2019. Graphene modified electrodes for bioelectricity generation in mediator-less microbial fuel cell. *Journal of Materials Science* 54: 11604-17

Pawel SJ. 1993. Corrosion of Nickel-Based Alloys in Acidified Lithium Chloride Solutions. *NACE-93110929* 49: 5

Park S and Ruoff RS (2009) Chemical methods for the production of graphenes. *Nature Nanotechnology* 4:217.

Pei P, Malghan SG, Dapkunas SJ and Zajchowski PH (1996) Characterization and processing of spray-dried zirconia powders for plasma spray application. *Journal of Thermal Spray Technology* 5:343-351.

Pergolesi D, Gilardi E, Fabbri E, Roddatis V, Harrington GF, Lippert T, Kilner JA and Traversa E (2018) Interface Effects on the Ionic Conductivity of Doped Ceria–Yttria-Stabilized Zirconia Heterostructures. *ACS Applied Materials & Interfaces* 10:14160-14169.

Pi J-K, Wu G-P, Yang H-C, Arges CG and Xu Z-K (2017) Separators with Biomineralized Zirconia Coatings for Enhanced Thermo- and Electro-Performance of Lithium-Ion Batteries. *ACS Applied Materials & Interfaces* 9:21971-21978.

Popoola LT, Grema AS, Latinwo GK, Gutti B, Balogun AS. 2013. Corrosion problems during oil and gas production and its mitigation. *International Journal of Industrial Chemistry* 4: 35

Prajitno DH, Maulana A and Syarif DG (2016) Effect of Surface Roughness on Contact Angle Measurement of Nanofluid on Surface of Stainless Steel 304 by Sessile Drop Method. *Journal of Physics: Conference Series* 739:012029.

Qiu Y, Thomas S, Gibson MA, Fraser HL and Birbilis N (2017) Corrosion of high entropy alloys. *npj Materials Degradation* 1:15.

Qiu Z, Wang R, Wu J, Zhang Y, Qu Y and Wu X (2015) Graphene oxide as a corrosion-inhibitive coating on magnesium alloys. *RSC Advances* 5:44149-44159.

Quintino L, Liskevich O, Vilarinho L, Scotti A. 2013. Heat input in full penetration welds in gas metal arc welding (GMAW). *The International Journal of Advanced Manufacturing Technology* 68: 2833-40

Rafiee J, Mi X, Gullapalli H, Thomas AV, Yavari F, et al. 2012. Wetting transparency of graphene. *Nature Materials* 11: 217

Rahman OSA, Chellasamy V, Ponpandian N, Amirthapandian S, Panigrahi BK, Thangadurai P. 2014. A facile green synthesis of reduced graphene oxide by using pollen grains of *Peltophorum pterocarpum* and study of its electrochemical behavior. *RSC Advances* 4: 56910-17

Ranjarnodeh E, Serajzadeh S, Kokabi AH, Fischer A. 2011. Effect of welding parameters on residual stresses in dissimilar joint of stainless steel to carbon steel. *Journal of Materials Science* 46: 3225-32

Ranjit S. 2015. Numerical Simulation of Similar and Dissimilar materials Welding Process; Quantification of Temperature, Stresses, Strain and Deformation. *International Journal of Engineering and Technology* 7: 335-49

Rashmi S, Elias L and Chitharanjan Hegde A (2017) Multilayered Zn-Ni alloy coatings for better corrosion protection of mild steel. *Engineering Science and Technology, an International Journal* 20:1227-1232.

Rezaei Ashtiani HR, Zarandooz R. 2016. Microstructural and mechanical properties of resistance spot weld of Inconel 625 super alloy. *The International Journal of Advanced Manufacturing Technology* 84: 607-19

Riaz S, Hamid S and Naseem S (2012) *Synthesis and characterization of FeO-ZrO₂ nanoparticles for bio-medical applications.*

Ribeiro DV, Souza CAC and Abrantes JCC (2015) Use of Electrochemical Impedance Spectroscopy (EIS) to monitoring the corrosion of reinforced concrete. *Revista IBRACON de Estruturas e Materiais* **8**:529-546.

Románszki L, Mohos M, Telegdi J, Nyikos L. 2013. *Contact Angle Measurement is an Efficient Tool for the Characterization of Corrosion Protection Nanolayers on Copper Alloys and Stainless Steel*.

Sadeghimeresht E, Reddy L, Hussain T, Huhtakangas M, Markocsan N and Joshi S (2018) Influence of KCl and HCl on high temperature corrosion of HVAF-sprayed NiCrAlY and NiCrMo coatings. *Materials & Design* **148**:17-29.

Samain L, Jaworski A, Edén M, Ladd DM, Seo D-K, et al. 2014. Structural analysis of highly porous γ -Al₂O₃. *Journal of Solid State Chemistry* **217**: 1-8

Selines RJ, Pelloux RM. 1972. Effect of cyclic stress wave form on corrosion fatigue crack propagation in al-zn-mg alloys. *Metallurgical Transactions* **3**: 2525-31

Shao C, Lu F, Wang X, Ding Y, Li Z. 2017. Microstructure characterization and HCF fracture mode transition for modified 9Cr-1Mo dissimilarly welded joint at different elevated temperatures. *Journal of Materials Science & Technology* **33**: 1610-20

Shrestha S, Hodgkiess T, Neville A. 2001. The effect of post-treatment of a high-velocity oxy-fuel Ni-Cr-Mo-Si-B coating Part I: Microstructure/corrosion behavior relationships. *Journal of Thermal Spray Technology* **10**: 470-79

Shukla VN, Jayaganthan R and Tewari VK (2015) Degradation Behavior of HVOF-Sprayed Cr₃C₂-25%NiCr Cermet Coatings Exposed to High Temperature Environment. *Materials Today: Proceedings* **2**:1805-1813.

Silva CC, Afonso CRM, Ramirez AJ, Motta MF, Miranda HC, Farias JP. 2016. Assessment of microstructure of alloy Inconel 686 dissimilar weld claddings. *Journal of Alloys and Compounds* **684**: 628-42

Singh P, Sharma A, Smirnov AV, Diallo MS, Ray PK, et al. 2018. Design of high-strength refractory complex solid-solution alloys. *npj Computational Materials* **4**: 16

Singh S, Sribalaji M, Wasekar NP, Joshi S, Sundararajan G, Singh R and Keshri AK (2016) Microstructural, phase evolution and corrosion properties of silicon carbide reinforced pulse electrodeposited nickel–tungsten composite coatings. *Applied Surface Science* **364**:264-272.

Song B, Bai M, Voisey KT, Hussain T. 2017. Role of Oxides and Porosity on High-Temperature Oxidation of Liquid-Fueled HVOF Thermal-Sprayed Ni50Cr Coatings. *Journal of Thermal Spray Technology* **26**: 554-68

Sowrirajan M, Mathews PK, Vijayan S, Amaladasan Y. 2018. Effect of weld dilution on post-weld thermal conductivity of austenitic stainless steel clad layers. *Materials Research Express* **5**: 096512

Sturgeon A (2003) The Corrosion Behavior of HVOF Sprayed Stainless Steel and Nickel Alloy Coatings in Artificial Seawater, in *CORROSION 2003*, NACE International, San Diego, California.

Su J, Chen Y and Huang Q (2016) Graphene nanosheet-induced toughening of yttria-stabilized zirconia. *Applied Physics A* **123**:10.

Tang X, Wang S, Xu D, Gong Y, Zhang J, Wang Y. 2013. Corrosion Behavior of Ni-Based Alloys in Supercritical Water Containing High Concentrations of Salt and Oxygen. *Industrial & Engineering Chemistry Research* **52**: 18241-50

Tailor S, Vashishtha N, Modi A and Modi SC (2019) Structural and mechanical properties of HVOF sprayed Cr₃C₂-25%NiCr coating and subsequent erosion wear resistance. *Materials Research Express* **6**:076435.

Tadyszak K, Majchrzycki Ł, Szyller Ł, Scheibe B. 2018. Preparation and characterization of partially reduced graphene oxide aerogels doped with transition metal ions. *Journal of Materials Science* **53**: 16086-98

Tchomgui-Kamga E, Alonzo V, Nanseu-Njiki CP, Audebrand N, Ngameni E, Darchen A. 2010. Preparation and characterization of charcoals that contain dispersed aluminum oxide as adsorbents for removal of fluoride from drinking water. *Carbon* **48**: 333-43

Toma FL, Stahr CC, Berger LM, Saaro S, Herrmann M, et al. 2010. Corrosion Resistance of APS- and HVOF-Sprayed Coatings in the Al₂O₃-TiO₂ System. *Journal of Thermal Spray Technology* 19: 137-47

Tong LB, Zhang JB, Xu C, Wang X, Song SY, et al. 2016. Enhanced corrosion and wear resistances by graphene oxide coating on the surface of Mg-Zn-Ca alloy. *Carbon* 109: 340-51.

Toribio J. 1998. Residual stress effects in stress-corrosion cracking. *Journal of Materials Engineering and Performance* 7: 173-82.

Venkateswara Rao A, Ranjith Kumar B. 2018. Structural, electrical and electrochemical studies on doubly doped LiMn_{2-x}(GdNi)_xO₄ cathode materials for Li-ion batteries. *Materials Letters* 227: 250-53

Wang W and Alfantazi A (2014) An electrochemical impedance spectroscopy and polarization study of the role of crystallographic orientation on electrochemical behavior of niobium. *Electrochimica Acta* **131**:79-88.

Xie Y, Li H, Ding C, Zheng X and Li K (2015) Effects of graphene plates' adoption on the microstructure, mechanical properties, and in vivo biocompatibility of calcium silicate coating. *International journal of nanomedicine* **10**:3855-3863.

Xing X, Di X and Wang B (2014) The effect of post-weld heat treatment temperature on the microstructure of Inconel 625 deposited metal. *Journal of Alloys and Compounds* **593**:110-116.

Xiong C, Jiang L, Zhang Y, Chu H, Jiang P. 2016. Characterization of sulfate diffusion into cement paste by low frequency impedance spectroscopy. *Materials Letters* 174: 234-37

Xu F, Lv Y, Liu Y, Shu F, He P, Xu B. 2013. Microstructural Evolution and Mechanical Properties of Inconel 625 Alloy during Pulsed Plasma Arc Deposition Process. *Journal of Materials Science & Technology* 29: 480-88

Yan L, Xiao K, Yi P, Dong C, Wu J, Bai Z, Mao C, Jiang L and Li X (2017) The corrosion behavior of PCB-ImAg in industry polluted marine atmosphere environment. *Materials & Design* **115**:404-414.

Yang C-W, Liu C, Lin D-J, Yeh M-L and Lee T-M (2017) Hydrothermal treatment and butylphosphonic acid derived self-assembled monolayers for improving the surface chemistry and corrosion resistance of AZ61 magnesium alloy. *Scientific Reports* **7**:16910.

Yang D, Xu Y, Xu W, Wu D, Sun Y and Zhu H (2008) Tuning pore size and hydrophobicity of macroporous hybrid silica films with high optical transmittance by a non-template route. *Journal of Materials Chemistry* **18**:5557-5562.

Yazdani B, Xu F, Ahmad I, Hou X, Xia Y, Zhu Y. 2015. Tribological performance of Graphene/Carbon nanotube hybrid reinforced Al₂O₃ composites. *Scientific Reports* **5**: 11579.

Ye X, Lin Z, Zhang H, Zhu H, Liu Z, Zhong M. 2015. Protecting carbon steel from corrosion by laser in situ grown graphene films. *Carbon* **94**: 326-34

Yu D and Tian J (2014) Superhydrophobicity: Is it really better than hydrophobicity on anti-corrosion? *Colloids and Surfaces A: Physicochemical and Engineering Aspects* **445**:75-78.

Yu Z, Di H, Ma Y, Lv L, Pan Y, et al. 2015. Fabrication of graphene oxide–alumina hybrids to reinforce the anti-corrosion performance of composite epoxy coatings. *Applied Surface Science* **351**: 986-96

Yu K, Jiang Z, Li C, Chen S, Tao W, et al. 2017. Microstructure and Mechanical Properties of Fiber Laser Welded GH3535 Superalloy. *Journal of Materials Science & Technology* **33**: 1289-99

Zhang B, Wang J, Wu B, Guo XW, Wang YJ, Chen D, Zhang YC, Du K, Oguzie EE and Ma XL (2018) Unmasking chloride attack on the passive film of metals. *Nature Communications* **9**:2559.

Zhang H, Wang D, Xue P, Wu LH, Ni DR and Ma ZY (2016) Microstructural evolution and pitting corrosion behavior of friction stir welded joint of high nitrogen stainless steel. *Materials & Design* **110**:802-810.

Zhang P, Liu Z. 2016. Physical-mechanical and electrochemical corrosion behaviors of additively manufactured Cr-Ni-based stainless steel formed by laser cladding. *Materials & Design* **100**: 254-62

Zhang X-C, Xu BS, Wang HD, Wu YX. 2005. Modeling of the Residual Stresses in Plasma-Spraying Functionally Graded ZrO₂/NiCoCrAlY Coatings Using Finite Element Method. *Materials & Design* **27**: 308-15

Zhang X, Liu D, Ma Y, Nie J and Sui G (2017) Super-hydrophobic graphene coated polyurethane (GN@PU) sponge with great oil-water separation performance. *Applied Surface Science* **422**:116-124.

Zhang Y, Zhao Y, Tang A, Yang W, Li E. 2018. In-Situ Electrochemical Corrosion Behavior of Nickel-Base 718 Alloy Under Various CO₂ Partial Pressures at 150 and 205 °C in NaCl Solution. *Metals and Materials International* **24**: 752-60

Zhao G-F, Deng Z-Q and Zhang B (2019) Multibody failure criterion for the four-dimensional lattice spring model. *International Journal of Rock Mechanics and Mining Sciences* **123**:104126.

Zhu W-f, Xu C, Zeng L. 2010. Coupled finite element analysis of MIG welding assembly on auto-body high-strength steel panel and door hinge. *The International Journal of Advanced Manufacturing Technology* **51**: 551-59

Zimmerman J, Lindemann Z, Golański D, Chmielewski T, Włosiński W. 2013. Modeling residual stresses generated in Ti coatings thermally sprayed on Al₂O₃ substrates. *Bulletin of the Polish Academy of Sciences, Technical Sciences* **61**: 515-25

List of Publications

Peer-reviewed journal publications

1. **Amudha A**, H.D. Shashikala, O.S Asiq Rahman, Anup Kumar Keshri and H.S. Nagaraja “Effect of graphene oxide loading on plasma sprayed alumina graphene oxide composite coating for improved corrosion resistance” submitted to ‘**Surface Topography: Metrology and Properties**’-IOP
DOI: [10.1088/2051-672X/ab2707](https://doi.org/10.1088/2051-672X/ab2707)
2. **A Amudha**, H D Shashikala, H S Nagaraja, “Finite Element Analysis of Thermal Residual Stresses in SS-309Mo and Inconel-625 Multilayer Hybrid Coatings on Low Carbon Steel” **International Journal of Fatigue-Elsevier**
DOI: [10.1016/j.ijfatigue.2019.06.014](https://doi.org/10.1016/j.ijfatigue.2019.06.014)
3. **A Amudha**, H D Shashikala and H S Nagaraja, “Corrosion protection of low-cost carbon steel with SS-309Mo and Inconel-625 bimetallic weld overlay” January 2019, **Material Research Express-IOP**, Volume 6 Number 4
DOI: [10.1088/2053-1591/aafba6](https://doi.org/10.1088/2053-1591/aafba6)
4. **Amudha A**, H.S Nagaraja and H.D Shashikala “Enhanced corrosion resistance of atmospheric plasma-sprayed zirconia-GNP composite by graphene oxide nanoplatelets encapsulation”, (**Applied Physics A-Springer**)
DOI: [10.1007/s00339-020-03779-w](https://doi.org/10.1007/s00339-020-03779-w)
5. **Amudha A**, H.D Shashikala and H.S Nagaraja, “Corrosion Behaviour and Characterization of Thermal Sprayed Coating of Nickel Chromium Cermet on Low Carbon Steel” January 2018, **Materials today: proceedings- Elsevier** 5(8):16100-16105,
DOI: [10.1016/j.matpr.2018.05.093](https://doi.org/10.1016/j.matpr.2018.05.093)
6. **Amudha A**, H.D Shashikala and H.S Nagaraja, “Electrochemical corrosion behaviour of nickel chromium-chromium carbide coating by HVOF process” April 2018 **AIP Proceedings** 1943(1):020092
DOI: [10.1063/1.5029668](https://doi.org/10.1063/1.5029668)
7. **Amudha A**, H.D Shashikala and H.S Nagaraja “Plasma-sprayed graphene oxide reinforced alumina composite coatings on low carbon steel with improved fracture

toughness, brittleness index and microhardness” (**Materials today: proceedings-Elsevier**)

DOI: [10.1016/j.matpr.2020.05.464](https://doi.org/10.1016/j.matpr.2020.05.464)

8. **Amudha A**, H.D Shashikala and H.S Nagaraja “Electrochemical impedance behaviour of SS-309Mo and Inconel 625 weld overlay on carbon steel at different applied voltages” **AIP Conference Proceedings** 2247, 040012 (2020)

DOI: <https://doi.org/10.1063/5.0004092>

9. **Amudha A**, H.S Nagaraja and H.D Shashikala “Mechanical and wetting properties of 25%NiCr-75%Cr₂C₃ cermet coated on low carbon steel using HVOF thermal spray technique” (**Physica B: condensed matter – Elsevier**)- (accepted)

10. **Amudha A**, H.S Nagaraja and H.D Shashikala “A comparative electrochemical corrosion investigation of SS-309Mo and Inconel-625 weld-overlay on carbon steel in artificial and natural sea water” (**Protection of metals and physical chemistry of surfaces- Springer**)-(under review)

Publications from other work

11. **Amudha Armugam**, Ravi Raju and Varun A Baheti, “Interdiffusion study of Co-Sb system”, Recent advances in mass transport in engineering materials, **Diffusion Foundations- Scientific.net**, 27 (2020) 35-39

DOI: [10.4028/www.scientific.net/DF.27.35](https://doi.org/10.4028/www.scientific.net/DF.27.35)

12. K. Brijesh, Bindu K, **A. Amudha**, Nagaraja H S. "Dual electrochemical application of r-GO wrapped ZnWO₄/Sb nanocomposite". **Materials Research Express-IOP** (2019) 6, 115030

DOI: [10.1088/2053-1591/ab4644](https://doi.org/10.1088/2053-1591/ab4644)

International Conference Presentations

Oral presentations

1. **A Amudha**, H.S Nagaraja and H.D Shashikala “*Electrochemical corrosion behaviour of nickel chromium-chromium carbide coating by HVOF process*” International conference on Design, Materials and Manufacture2018 (ICDEM-2018), 29-31 January 2018. Conducted by NITK Surathkal.

2. **A Amudha**, H.S Nagaraja and H.D Shashikala “*Electrochemical impedance behaviour of SS-309Mo and Inconel 625 weld overlay on carbon steel at different applied voltages*” 2nd International Conference on Design, Materials and Manufacture (ICDEM-2019), 6-8th December-2019, Conducted by Department of MME NITK Surathkal.
3. **A Amudha**, H.S Nagaraja and H.D Shashikala “*Plasma-sprayed graphene oxide reinforced alumina composite coatings on low carbon steel with improved fracture toughness, brittleness index and microhardness*” 2nd International Conference on Recent Trends in Metallurgy, Materials Science and Manufacturing (IMME-19), 27– 28th December-2019 conducted by the Department of MME, NIT Trichy (**Best Paper Award**)
4. **A Amudha**, H.S Nagaraja and H.D Shashikala “*Mechanical and wetting properties of the NiCr-Cr₂C₃ cermet coated on low carbon steel using Thermal Spray Technique*” International conference on Current Trends in Functional Materials (CTFM-2020), 15-17th January, 2020 conducted by The Department of Physics, NITK Surathkal.

Poster Presentations

5. **A Amudha**, H.S Nagaraja and H.D Shashikala “*Thermal residual stress studies in multilayer weld coatings on low carbon steel to prevent environmental cracking*” 12th International conference on fatigue damage of structural materials (FATD-2018) USA, 16-21st September-2018 at Hyannis, USA. Conducted by ELSEVIER.
6. **A Amudha**, H.S Nagaraja and H.D Shashikala “*Synthesis and characterization of Hydrothermally synthesized alumina-graphene oxide composite*” International Conference on Nanotechnology: Ideas, Innovations and Initiatives-2017” (ICN:3I-2017), 06-08 December 2017. Conducted by IIT Roorkee. India
7. **A Amudha**, H.S Nagaraja and H.D Shashikala “*Corrosion Behaviour and Characterization of Thermal Sprayed Coating of Nickel Chromium Cermet on Low Carbon Steel*” International Conference on Advanced Materials ‘SCICON’16, 19-

21 December, 2016. Conducted by Amritha University, Coimbatore. Tamilnadu, India

List workshops attended

1. GIAN course on “Thermal sprayed coatings and Composites: Science, Engineering and Applications” conducted by MNNIT Allahabad from June 20 to July 1, 2016.
2. GIAN course on “Novel Functional Materials for energy conversion” conducted by NITK Surathkal from 4th to 7th October 2016.

Curriculum Vitae

Amudha A

Material Processing Laboratory, Department of Physics
National Institute of Technology Karnataka, Surathkal, Mangalore– 575 025
Contact No: 98442 06577, E-mail: amudha1512@gmail.com

Objective

To secure a responsible career opportunity where I can utilize my research and teaching skills, while making a significant contribution to the society in a professional environment.

Areas of interest

Material Science

- Electrochemical corrosion studies
- Mechanical properties of the materials
- Wetting properties of the coatings
- Metal alloys, Ceramics and Nanocomposite materials
- Thin film coatings and thermal spray coatings for various applications
- Diffusion in solids
- Intermetallics

Education

Course	Institution	Year of Completion
Ph.D	Department of Physics, National Institute of Technology Karnataka (NITK) Surathkal, India Guides: Prof. H. D Shashikala Dr. H.S Nagaraja	2020 (expected)
M.Sc	Department of Physics, National Institute of Technology Karnataka (NITK), Surathkal, India	2013
B.Sc.	The National Degree College, Bangalore, India	2011

Publications**Peer-reviewed journal publications:**

1. **Amudha A**, H.D. Shashikala, O.S Asiq Rahman, Anup Kumar Keshri and H.S. Nagaraja “Effect of graphene oxide loading on plasma sprayed alumina graphene oxide composite coating for improved corrosion resistance” submitted to ‘**Surface Topography: Metrology and Properties**’-IOP
DOI: [10.1088/2051-672X/ab270](https://doi.org/10.1088/2051-672X/ab270)
2. **A Amudha**, H D Shashikala, H S Nagaraja, “Finite Element Analysis of Thermal Residual Stresses in SS-309Mo and Inconel-625 Multilayer Hybrid Coatings on Low Carbon Steel” **International Journal of Fatigue-Elsevier**
DOI: [10.1016/j.ijfatigue.2019.06.014](https://doi.org/10.1016/j.ijfatigue.2019.06.014)
3. **A Amudha**, H D Shashikala and H S Nagaraja, “Corrosion protection of low-cost carbon steel with SS-309Mo and Inconel-625 bimetallic weld overlay” January 2019, **Material Research Express-IOP**, Volume 6 Number 4
DOI: [10.1088/2053-1591/aafba6](https://doi.org/10.1088/2053-1591/aafba6)
4. **Amudha Armugam**, Ravi Raju and Varun A Baheti, “Interdiffusion study of Co-Sb system”, Recent advances in mass transport in engineering materials, **Diffusion Foundations- Scientific.net**, 27 (2020) 35-39
DOI: [10.4028/www.scientific.net/DF.27.35](https://doi.org/10.4028/www.scientific.net/DF.27.35)
5. **Amudha A**, H.S Nagaraja and H.D Shashikala “Enhanced corrosion resistance of atmospheric plasma-sprayed zirconia-GNP composite by graphene oxide nanoplatelets encapsulation”, (**Applied Physics A-Springer**)
DOI: [10.1007/s00339-020-03779-w](https://doi.org/10.1007/s00339-020-03779-w)
6. K. Brijesh, Bindu K, **A. Amudha**, Nagaraja H S. "Dual electrochemical application of r-GO wrapped ZnWO₄/Sb nanocomposite". **Materials Research Express-IOP** (2019) 6, 115030
DOI: [10.1088/2053-1591/ab4644](https://doi.org/10.1088/2053-1591/ab4644)
7. **Amudha A**, H.D Shashikala and H.S Nagaraja, “Corrosion Behaviour and Characterization of Thermal Sprayed Coating of Nickel Chromium Cermet on Low Carbon Steel” January 2018, **Materials today: proceedings- Elsevier** 5(8):16100-16105,
DOI: [10.1016/j.matpr.2018.05.093](https://doi.org/10.1016/j.matpr.2018.05.093)
8. **Amudha A**, H.D Shashikala and H.S Nagaraja, “Electrochemical corrosion behaviour of nickel chromium-chromium carbide coating by HVOF process” April 2018 **AIP Proceedings** 1943(1):020092
DOI: [10.1063/1.5029668](https://doi.org/10.1063/1.5029668)
9. **Amudha A**, H.D Shashikala and H.S Nagaraja “Plasma-sprayed graphene oxide reinforced alumina composite coatings on low carbon steel with improved fracture toughness, brittleness index and microhardness” (**Materials today: proceedings-Elsevier**)
DOI: [10.1016/j.matpr.2020.05.46](https://doi.org/10.1016/j.matpr.2020.05.46)
10. **Amudha A**, H.D Shashikala and H.S Nagaraja “Electrochemical impedance behaviour of SS-309Mo and Inconel 625 weld overlay on carbon steel at different

applied voltages” **AIP Conference Proceedings** 2247, 040012 (2020) DOI: <https://doi.org/10.1063/5.0004092>

11. **Amudha A**, H.S Nagaraja and H.D Shashikala “Mechanical and wetting properties of 25%NiCr-75%Cr₂C₃ cermet coated on low carbon steel using HVOF thermal spray technique” (**Physica B: condensed matter – Elsevier**)- ([accepted](#))
12. **Amudha Arumugam**, Ravi Raju and Varun A Baheti "Diffusion Parameters and Growth Mechanism of Mg₂Ni phase: a promising hydrogen storage material grown by interdiffusion"-**JPED- Elsevier** ([under review](#))
13. **Amudha A**, H.S Nagaraja and H.D Shashikala “A comparative electrochemical corrosion investigation of SS-309Mo and Inconel-625 weld-overlay on carbon steel in artificial and natural sea water” (**Protection of metals and physical chemistry of surfaces- Springer**)-([under review](#))

Conference Presentations

Oral presentations

1. **Amudha A**, H.S Nagaraja and H.D Shashikala “International conference on Current Trends in Functional Materials (**CTFM-2020**) held from **15th-17th January 2020** conducted by The Department of Physics, NITK Surathkal.
2. **Amudha A**, H.S Nagaraja and H.D Shashikala “2nd International Conference on Recent Trends in Metallurgy, Materials Science and Manufacturing” (**IMME-19**) held from **27th-28th December-2019** conducted by the Department of Metallurgical and Materials Engineering, National Institute of Technology, Tiruchirappalli. (**Best paper award**).
3. **Amudha A**, H.S Nagaraja and H.D Shashikala “2nd International Conference on Design, Materials and Manufacture” (**ICDEM-2019**), **6th-8th December 2019**, Conducted by Department of Mechanical Engineering- NITK Surathkal.
4. **Amudha A**, H.S Nagaraja and H.D Shashikala “International conference on Design, Materials and Manufacture-2018” (**ICDEM-2018**), **29th-31st January 2018**. Conducted by NITK Surathkal.

Poster presentations

5. **Amudha Arumugam**, Ravi Raju and Varun A Baheti, “15th International conference on diffusion in solids and Liquids” (**DSL 2019 ATHENS**) held from **24th -28th June-2019** conducted by Diffusion Foundations at Athens, Greece.
6. **Amudha A**, H.S Nagaraja and H.D Shashikala “12th International conference on fatigue damage of structural materials” (**FATD-2018 USA**), held from **16th- 21st September-2018** at Hyannis, Cape Cod, USA. Conducted by ELSEVIER.
7. **Amudha A**, H.S Nagaraja and H.D Shashikala “International Conference on Nanotechnology: Ideas, Innovations and Initiatives-2017” (**ICN:3I-2017**), **06th-08th December 2017** conducted by IIT Roorkee, India.

8. K. Brijesh, Bindu K, **Amudha A**, Nagaraja H S “International Conference on Nanotechnology: Ideas, Innovations and Initiatives-2017” (ICN:3I-2017), **6th-8th December 2017** conducted by IIT Roorkee, India.
9. **Amudha A**, H.S Nagaraja and H.D Shashikala “International Conference on Advanced Materials SCICON’16, **19th-21st December, 2016** conducted by Amritha University, Coimbatore. Tamilnadu, India.
10. **Amudha A**, Chowdareddy N, H.D Shashikala “National Conference on Smart Materials and Technologies for Emerging Electronics” held at Mangalore Institute of Technology and Engineering, Moodabidiri on **March 8th-9th, 2013** Karnataka, India.

Achievements and awards

- NITK institutional fellowship for Ph.D. (2015-2020) awarded by MHRD, India.
- Received **best paper award** for oral presentation in “2nd International Conference on Recent Trends in Metallurgy, Materials Science and Manufacturing” (IMME-19) held from **27th – 28th December-2019** conducted by the Department of Metallurgical and Materials Engineering, National Institute of Technology, Tiruchirappalli. India
- Was class topper in PCM division of BSc (Under Graduate).
- Won prizes for securing highest marks in Chemistry for all the three years of BSc at “The National Degree College-Jayanagar, Bangalore”.
- Won second prize in Chemistry speaking competition conducted by “The National Degree College, Jayanagar, Bangalore”.
- Won first prize in English literature competition at Under Graduate level.

Teaching experience

Position: Guest Faculty for MSc Physics students

Subjects thought: Classical mechanics, Solid state physics and Astrophysics

Institute: Department of Physics, National Degree College (Autonomous) Jayanagar, Bangalore, Karnataka, India

Duration: August 2013-January 2015 (**1 year and 6 months**)

Research experience

1. Project Name: Synthesis and characterization of thermal sprayed coatings: corrosion, mechanical and wetting properties (July 2015 to July 2020)

Institute: Department of physics, National Institute of Technology Karnataka (NITK)-Surathkal

Designation: Research Scholar

Guides: Prof. H.D Shashikala and Dr. H.S Nagaraja

2. Project Name: Diffusion mechanism in Mg-Ni, Co-Sb and Pd-Zn binary alloys. (July 2013 to December 2014)

Institute: Department of Materials Engineering, Indian Institute of Science (IISc), Bangalore

Designation: Project Assistant

Guides: Prof. Alope Paul and Dr. R. Ravi

3. Project name: Oxidation, Corrosion Resistance and Micro-hardness of thermally treated Ti6Al4V Alloy. (MSc major project) (July 2012 to June 2013)

Institute: National Institute of Technology Karnataka (NITK)-Surathkal

Guide: Prof. H.D Shashikala

Hands on experience of experimental facilities

1. Rigaku miniflex-600 X-ray diffractometer
2. Holmarc's contact angle meter (Goniometer)
3. Microhardness tester
4. Abbe refractrometer
5. Physical vapour deposition (PVD) unit
6. Spin coating unit, Dip coating and thermal enamelling coating
7. Biologic SP-150 electrochemical workstation
8. Ocean optics UV-visible spectrometer and Diffuse reflectance spectrometer
9. Sigma photoluminescence spectrometer
10. High temperature and muffle furnaces.

Software skills

- Experience in analysing the data using Panalytical **Xpert highscore plus**, **Origin**, **Zsimpwin**, **EC-lab softwares**, **ImageView**, **ImageJ** and **Peakfit. v4.11** softwares.
- Finite Element Analysis (**FEA**) of residual stresses using **ANSYS** Simulation software.
- Generating crystal structure using **VESTA** and **Adobe crystal maker**.

Analysing skills

Characterization techniques like XRD, FTIR, SEM, TEM, EDS, XPS, CV, EIS, Potentiodynamic Polarization technique, Chronoamperometry, Chronopotentiometry, mechanical properties like Microhardness, Brittleness index and Fracture Toughness.

